TECHNISCHE UNIVERSITÄT MÜNCHEN
TUM School of Computation, Information and Technology

Gyrokinetic investigation on linear and non-linear energetic-particle driven instabilities in experimental relevant scenarios

Brando Rettino

Vollständiger Abdruck der von der TUM School of Computation, Information and Technology der Technischen Universität München zur Erlangung eines

Doktors der Naturwissenschaften
(Dr. rer. nat.)

genehmigten Dissertation.

Vorsitz:	Prof. Dr. Eric Sonnendrücker
Prüfer der Dissertation:	1. Hon.-Prof. Dr. Frank Jenko
	2. Prof. Dr. Laurent Villard

Die Dissertation wurde am 28.08.2023 bei der Technischen Universität München eingereicht und durch die TUM School of Computation, Information and Technology am 26.01.2024 angenommen.

TECHNISCHE UNIVERSITÄT MÜNCHEN

TUM School of Computation, Information and Technology

Max-Planck-Institut für Plasmaphysik

Gyrokinetic investigation on linear and non-linear energetic-particle driven instabilities in experimental relevant scenarios

Author:	Brando Rettino
Supervisor:	Prof. Dr. Frank Jenko
Advisors:	Dr. Alberto Bottino
Submission Date:	_____

Abstract

This thesis enquires into the mechanisms of energetic particle-driven instabilities in experimental plasma scenarios, focusing on the dynamics of energetic-particle driven Geodesic Acoustic Modes (EGAMs) and Alfvén Modes (AMs). The ability to predictively simulate the dynamics of energetic particles (EPs) in experimental scenarios is crucial for the operation of future fusion reactors. EP transport is expected to constitute a considerable fraction of the total heat transport in future fusion devices, therefore the EPs' dynamics become fundamental for burning plasma operations. This work is a milestone on the pathway to predictive, global, reactor-relevant plasma simulations. Experimental-like distribution functions were employed, including an analytical distribution function whose phase-space anisotropy has been parametrized and a numerical distribution function generated from the RABBIT code. The simulations were performed using the ORB5 code, a gyrokinetic particle-in-cell (PIC) global electromagnetic code. We incorporated experimental equilibrium and profiles from the NLED-AUG case, an experimental ASDEX-Upgrade case, with experimental relevant anisotropic distribution functions.

The thesis presents a comprehensive analysis of the linear stability of the EGAM influenced by experimental-like anisotropic EP distribution functions. The simulations reveal that EGAMs are primarily excited for high anisotropy levels and mid range pitches. Large scans over the anisotropy parameter-space using the ORB5 code are conducted to determine the linear stability threshold depending on anisotropy parameters, EP density fraction and temperature. Furthermore, many analytical models and numerical diagnostics were employed to study the linear stability characteristics of EGAMs.

Next, non-linear, electromagnetic, multi-mode simulations are performed. The simulations demonstrate the excitation of EGAMs through wave-wave coupling between $n = 1$ Alfvén Waves (AWs) and $n = 0$ Zonal Structures (ZS). This excitation dominates over the linear drive of EGAMs if the EPs cannot drive linearly the instability. This result is more consistent with experimental findings, furthermore it aligns well with theory and previous simulations, revealing growth rates depending on specific pitch angles. Additionally, simulations using numerically calculated neutral beam generated distribution functions (RABBIT code) show qualitative agreement with experimental measurements.

In conclusion, this thesis presents important advancements in the topic of non-linear EP dynamics proved by good qualitative agreement between simulations, theoretical predictions and experiments. This demonstrates the capability of the ORB5 code to

handle experimental-like anisotropic EP distribution functions. We are confident that with accurate reconstruction of profiles and distribution functions we can reproduce the non-linear EP dynamics with quantitative agreement with the experiment. Thus, the findings presented in the thesis provide a foundation for predictive tokamak simulations and contribute to the understanding of EP dynamics in fusion devices.

Zusammenfassung

Diese Arbeit untersucht von energetischen Teilchen getriebenen Instabilitäten in experimentellen Plasmaszenarien und konzentriert sich auf die Dynamik von sogenannten 'energetic-particle driven geodesic acoustic modes' (EGAMs) und Alfvén Moden (AMs). Die Fähigkeit, die Dynamik energetischer Teilchen (EPs) in experimentellen Szenarien vorherzusagen, ist für den Betrieb zukünftiger Fusionsreaktoren entscheidend. Der Transport der EPs wird voraussichtlich einen erheblichen Anteil am Gesamtwärmetransport in zukünftigen Fusionsanlagen ausmachen, weshalb die Dynamik der EPs für den Betrieb von eines brennenden Fusionsreaktors fundamental ist. Diese Arbeit stellt einen Meilenstein auf dem Weg zu prädiktiven globalen, reaktorrelevanten Plasmasimulationen dar. Experiment-ähnliche Verteilungsfunktionen wurden verwendet, darunter eine analytische Verteilungsfunktion, deren Phasenraumanisotropie parametrisiert wurde, und eine numerische Verteilungsfunktion, die aus dem RABBIT-Code generiert wurde. Die Simulationen wurden mit dem ORB5-Code durchgeführt, einem gyrokinetischen Particle-in-Cell (PIC) globalen elektromagnetischen Code. Wir haben damit zum ersten mal experimentelle magnetische Gleichgewichte und Profildaten aus dem NLED-AUG-Fall, einem experimentellen ASDEX-Upgrade Szenario, mit experimentell relevanten anisotropen Verteilungsfunktionen kombiniert.

Die Arbeit präsentiert eine umfassende Analyse der linearen Stabilität der EGAM, die von experiment-ähnlichen anisotropen EP-Verteilungsfunktionen bestimmt wird. Die Simulationen zeigen, dass EGAMs hauptsächlich bei hohen Anisotropien von einer bestimmten Klasse von Teilchen im Geschwindigkeitsraum (mittelgrosse pitch-Winkel) angeregt werden. Es wurden umfangreiche Scans über den Anisotropie-Parameterbereich mit dem ORB5-Code durchgeführt, um die lineare Stabilitätsschwelle abhängig von Anisotropie-Parametern, EP-Dichtefraktion und Temperatur zu bestimmen. Darüber hinaus wurden verschiedene analytische Modelle und numerische Diagnostiken eingesetzt, um die linearen Stabilitätseigenschaften der EGAMs zu untersuchen.

Anschließend werden nichtlineare, elektromagnetische, Multi-Moden Simulationen durchgeführt. Die Simulationen zeigen die Anregung von EGAMs durch die Wellen-Wellen-Kopplung zwischen Alfvén-Wellen (AWs) mit toroidaler Modenzahl $n = 1$ und zonalen Strukturen (ZS) mit $n = 0$. Diese Anregung dominiert über den linearen Antrieb von EGAMs, wenn die EPs die Instabilität nicht linear destabilisieren können. Dieses Ergebnis stimmt relativ gut mit experimentellen Befunden überein und passt zudem gut zur

Theorie und zu früheren Simulationen, bei denen die Wachstumsraten von spezifischen pitch-Winkeln abhängen. Zusätzlich zeigen Simulationen mit numerisch berechneten Verteilungsfunktionen, die durch den RABBIT-Code generiert wurden, eine qualitative Übereinstimmung mit experimentellen Messungen.

Kurz gefasst präsentiert diese Arbeit wichtige Fortschritte im Bereich der nichtlinearen EP-Dynamik, die durch eine gute qualitative Übereinstimmung zwischen Simulationen, theoretischen Vorhersagen und Experimenten belegt werden. Dies demonstriert die Fähigkeit des ORB5-Codes, experiment-ähnliche anisotrope EP-Verteilungsfunktionen zu verarbeiten. Wir sind zuversichtlich, dass wir mit genauerer Rekonstruktion von Profilen und Verteilungsfunktionen die nichtlineare EP-Dynamik quantitativ mit den Experimenten in Einklang bringen können. Die in der Arbeit vorgestellten Ergebnisse legen somit eine Grundlage für vorhersagbare Tokamak-Simulationen und tragen zum Verständnis der EP-Dynamik in Fusionsanlagen bei.

Contents

List of Figures

List of Abbreviations

ALE	**A**brupt **L**arge-amplitude **E**vents
AM	**A**lfvén **M**odes
ARC	**A**ffordable **R**obust **C**ompact fusion reactor
ASCOT	**A**ccelerated **S**imulation of **C**harged Particle **O**rbits in **T**ori
ASD	**A**nisotropic **S**lowing-**d**own
ASDEX	**A**xial **S**ymmetric **D**ivertor **Ex**periment
AUG	**A**SDEX **U**p**g**rade
AW	**A**lfvén **W**aves
CXRS	**C**harge **Ex**change **R**ecombination **S**pectroscopy
D	**D**euterium
EAE	**E**llipticity-induced **A**lfvén **E**igenmode
ECE	**E**lectron **C**yclotron **E**mission
ECRH	**E**lectron **C**yclotron **R**esonance **H**eating
EGAM	**E**nergetic particle driven **G**eodesic **A**coustic **M**ode
EP	**E**nergetic **P**articles
EPM	**E**nergetic **P**article driven **M**ode
FEM	**F**inite **E**lement **M**ethod
FLR	**F**inite **L**armor **R**adius
FOW	**F**inite **O**rbit **W**idth
FP	**F**okker-**P**lanck
FWHM	**F**ull **W**idth at **h**alf **M**aximum
GAM	**G**eodesic **A**coustic **M**ode
GENE	**G**yrokinetic **E**lectromagnetic **N**umerical **E**xperiment
GK	**G**yro**k**inetic
HFS	**H**igh **F**ield **S**ide
IC	**I**on **C**yclotron
ICRF	**IC** **R**ange of **F**requencies
ICRH	**I**on **C**yclotron **R**esonance **H**eating
ITER	**I**nternational **T**hermonuclear **E**xperimental **R**eactor
ITG	**I**on **T**emperature **G**radient Mode
JT	**J**apan **T**okamak
JT-60SA	**JT**-60 **S**uper-**A**dvanced
JT-60U	**JT**-60 **U**pgrade
LFS	**L**ow **F**ield **S**ide
LIGKA	**Li**near **G**yro**k**inetic shear **A**lfvén physics
MagLIF	**Mag**netized **L**iner **I**nertial **F**usion
MHD	**M**agneto**h**ydro**d**ynamics
MPG	**M**ax-**P**lanck **G**esellschaft

MPR	**M**ode **P**article **R**esonance
NAE	**N**on-circularity-induced **A**lfvén **E**igenmode
NBI	**N**eutral **B**eam **I**njection
NLED-AUG	**N**on-linear **E**nergetic particle **D**ynamics in **AUG**
PDF	**P**lasma **D**ispersion **F**unction
PIC	**P**article-**i**n-**c**ell
PSZS	**P**hase-**s**pace **Z**onal **S**tructure
RABBIT	**R**apid **A**nalytical **B**ased **B**eam **I**njection **T**ool
RHS	**R**ight **H**and **S**ide
SAW	**S**hear **AW**
SD	**S**lowing-**d**own
SPARC	**S**oonest/**S**mallest **P**ossible **ARC**
T	**T**riutium
TAE	**T**oroidal **A**lfvén **E**igenmode
TEM	**T**rapped **E**lectron **M**ode
TS	**T**hompson **S**cattering
WP	**W**ave-**p**article
XGC	**X**-Point included **G**yrokinetic **C**ode
ZF	**Z**onal **F**lows
ZFZF	**Z**ero **F**requency **Z**onal **F**lows
ZS	**Z**onal **S**tructures

1 Introduction

1.1 Nuclear Fusion

Soon after the discovery of nuclear power through fission, since the '50s, physicists tried to obtain energy from the opposite principle: nuclear fusion. Such source of energy is the one that powers the stars of the universe. Being able to control and exploit such powerful and unlimited [1] source of energy has been pursued for very long time with great endeavour. In fact, it is hoped to be a compact, renewable, abundant energy source not only in the next hundreds of years but as far in the future as we can possibly imagine. Even if this field of study may already seem important enough on its own for the reasons aforementioned, its importance becomes crucial if lowered in the nowadays energy ever-craving society [2].

Like fission, also fusion exploits the energy "hidden" in the nuclei of the atoms. Nuclei of different elements have different binding energy. Such nuclear energy can be released either with fission or fusion reactions, provided that the binding energy of the products is lower than that of the reactant. As it is clearly depicted in figure 1.1, we can harvest energy from splitting heavy nuclei in lighter products. Such process is obtained, for example, splitting an Uranium nucleus U^{235}, by means of a fast neutron, into lighter products (Kr^{92}, Sr^{141}). Unlike fission, in fusion two nuclei of light elements are bound together to obtain a heavier one and deliver energy.
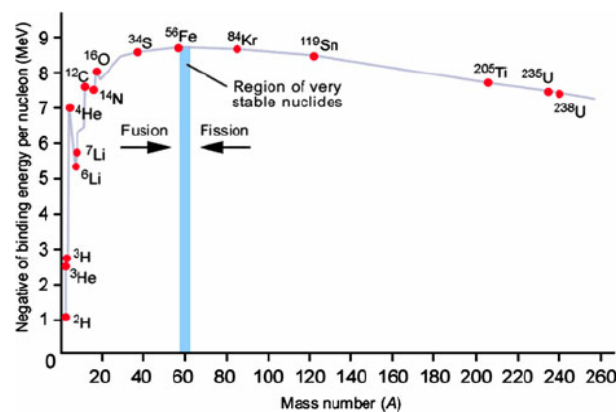
Figure 1.1: Negative binding energy with respect to mass number. Taken from [3]

There are several fusion reactions that can deliver energy. Nevertheless, the reaction which offers the largest cross section, in other words the most simple reaction to exploit, is the following one:

$$D+T \longrightarrow \alpha + n + 17.6\,MeV \ , \tag{1.1}$$
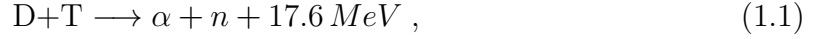
where D and T are deuterium and tritium, two isotopes of hydrogen with respectively one and two neutrons, α is an Helium-4 nucleus and n is a neutron. This reaction delivers $17.6\,MeV$ of kinetic energy distributed between the products according to their mass: 20% of it will go to the α-particle ($3.5\,MeV$) and 80% to the neutron ($14.1\,MeV$). The idea is exploiting this released energy as a heat source in a thermodynamic cycle. Electric power is harnessed by dynamos connected to turbines, as done traditionally in any thermo-electric power plant.

The first attempt to obtain sustained fusion reactions was through beam-target or beam-beam devices. Physicists thought it was enough to provide particles with enough energy to overcome the electrostatic potential barrier (in the order of keV) to let them react. The power balance would have anyhow given a great energy gain (MeV yielded against keV needed). Very soon it was clear that this process was useless because of the losses due to the much more frequent Coulomb collisions. At this point it was clear that the only sustained fusion process could be achieved only in very hot thermalized plasmas. Such plasma must be kept at sufficient high temperatures and densities for a long enough time span in order to let fusion reactions occur. The most important condition of a fusion reactor is the capability to produce more nuclear power P_{fus} than the potentially lost power P_{loss}. In the D-T case, fusion power can be evaluated as follows:

$$P_{fus} = \frac{1}{4} n_D \, n_T \, \langle \sigma v \rangle_{v,DT} \, E_{DT} \ , \tag{1.2}$$

where $n_{D,T}$ is the particle density of deuterium or tritium, $\langle \sigma v \rangle_v$ is the cross section for a given fusion reaction, which is a function of plasma temperature T, the operator $\langle ... \rangle_v$ is an average over a velocity maxwellian distribution function: $\langle ... \rangle_v = \int ... f_s d^3 v$, E_{DT} is the energy released by a D-T reaction. By definition, the power loss P_{loss} can be expressed as the ratio between the energy stored in the plasma and the energy confinement time τ_E, which, on the contrary, is the ratio between the energy stored in the plasma and the heat loss power:

$$P_{loss} = \frac{3nT}{\tau_E} \ , \tag{1.3}$$

where n is the D-T plasma density. In order to achieve the reactor condition the following equation must be satisfied:

$$P_{fus} > P_{loss} \implies n\tau_E > \frac{12\,T}{\langle \sigma v \rangle_{DT}\,E_{DT}} \; . \tag{1.4}$$

Lawson first defined this ignition criterion [4], which is commonly expressed as the well known "triple product" [5], obtained by multiplying 1.4 by the temperature T and considering its minimum (D-T reaction cross section is maximised for $T \geq 15\ keV$, and approximating $\langle \sigma v \rangle \propto T^2$ in the range $T \sim 15\ keV$):

$$nT\tau_E > 3.5 \cdot 10^{21}\ m^{-3} \cdot keV \cdot s \; . \tag{1.5}$$

In figure 1.2, the triple products for three different fusion reactions are shown. As said before it is easiest to realise a burning fusion plasma based on the D-T reaction.
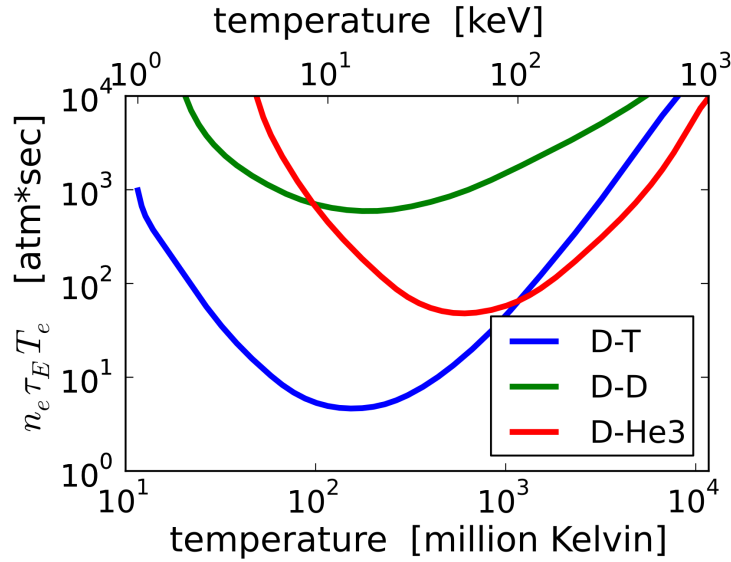
Figure 1.2: Triple products for different fusion reactions, taken from [6]

Therefore, to achieve such extreme conditions it is necessary to heat a D-T plasma at very high temperatures for as long time as possible. These temperatures are extremely harsh (15 $keV \simeq 174$ million K, the core of the Sun has $T_{sun} = 15$ million K), and thus there cannot be direct contact of this hot plasma with any material. Hence, electrostatic or magnetic confinement must be adopted to confine this very hot plasma. A number of devices, exploiting different principles, were developed and tested in the decades starting from the '50s. Still today many institutes, research centers and companies keep studying different concepts to achieve the best confinement. In the section 1.3, the main concepts are highlighted.

In the following section the principles of plasma physics are briefly presented. Plasma physics disciplines the behaviors of ionized gases, and many studies in fusion science derive from this very important branch of physics.

1.2 Plasma Physics

Plasma is often referred to as the fourth state of aggregation of condensed matter. The plasma state is characterized by the following main feature: the atoms are partially or fully ionised and thus positive and negative charged particles are the dominating constituents. In the core of (magnetic) fusion plasma devices, considered the great temperatures at play, we can consider all the particles to be fully or partially ionized. There are two main parameters characterizing a plasma. The first one is the so called Debye length, the distance within which the particles undergo the Coulomb forces of other charges:

$$\lambda_D = \sqrt{k_B \frac{T_e}{4\pi e^2 n_e}}, \tag{1.6}$$

where T_e is the electron temperature, e the electron charge, n_e the electron density and k_B the Boltzmann constant. Another important plasma parameter is the plasma frequency, which is the characteristic frequency arising in a plasma if a net charge separation is applied:

$$\omega_p = \sqrt{4\pi e^2 \frac{n_e}{m_e}}, \tag{1.7}$$

where m_e is the electron mass. Conventionally an ionized gas can be considered as a plasma if the following conditions are respected:

$$L \gg \lambda_D, \; \omega_p \gg \frac{v_{th}}{L}, \tag{1.8}$$

where L is the characteristic dimension of the plasma, and v_{th} the thermal velocity of the plasma particles.

Given the nature of its charged particles, a plasma is affected by magnetic fields $\mathbf{B}$. In particular the charged particles are affected by Lorentz forces:

$$\mathbf{F}_L = q(\mathbf{v} \times \mathbf{B} + \mathbf{E}), \tag{1.9}$$

where q is the charge of the particle, $\mathbf{v}$ its velocity, $\mathbf{B}$ is the magnetic field vector and $\mathbf{E}$ is the electric field vector. Therefore, particles will gyrate around magnetic field lines with the cyclotron frequency:

$$\omega_c = \frac{|q|B}{mc},$$ (1.10)

where q and m are the charge and the mass of the particle, c is the speed of light, while $B = |\mathbf{B}|$ is the value of the module of the magnetic field. The radius of such gyromotion is called Larmor radius:

$$\rho_L = \frac{v_\perp}{\omega_c} = \frac{v_\perp mc}{|q|B}.$$ (1.11)

For many thermal particles we have that $v_\perp \sim v_{th}$, therefore for such particles it is useful to define also a thermal larmor radius:

$$\rho_{L,th} = \frac{v_{th}}{\omega_c} = \frac{v_{th}mc}{|q|B}.$$ (1.12)

Given these basic characteristic parameters, in the next section we will offer two approaches to describe the collective behavior of a plasma. Since an exact microscopic description of all the particles in a reactor is unfeasible we need to introduce some approximations. We will accept that the particles can be described by some distribution in phase-space for the kinetic model or we will consider only space dependencies for a fluid model derived from the former.

1.2.1 Kinetic description

In the kinetic model we assume that the particles can be represented by an s-species distribution function $F_s(\mathbf{x}, \mathbf{v}, t)$ in six dimensions: three spatial ones $\mathbf{x}$, three in the velocity space $\mathbf{v}$, plus the dependency from time t. The evolution in time of such a distribution function is offered by the Boltzmann equation:

$$\frac{dF_s}{dt} = \frac{\partial F_s}{\partial t} + \mathbf{v} \cdot \frac{\partial F_s}{\partial \mathbf{x}} + \mathbf{a} \cdot \frac{\partial F_s}{\partial \mathbf{v}} = \left(\frac{\partial F_s}{\partial t} \right)_{coll},$$ (1.13)

where $\mathbf{v}$ and $\mathbf{a}$ are the velocity and the acceleration of the species and the right hand side term is the rate of change of F_s due to collisions. In some cases we can accept the collisional term to be 0. Considering that the forces exerted on a plasma come from electric fields $\mathbf{E}$ and magnetic fields $\mathbf{B}$ (through Lorentz force eq. 1.9), the acceleration of a plasma species will be

$$\mathbf{a} = \frac{q_s}{m_s}(\mathbf{E} + \frac{\mathbf{v} \times \mathbf{B}}{c}).$$ (1.14)

Plugging 1.14 into 1.13, and considering the collisional term to be 0, we obtain the

Vlasov equation [7]:

$$\frac{dF_s}{dt} = \frac{\partial F_s}{\partial t} + \mathbf{v} \cdot \frac{\partial F_s}{\partial \mathbf{x}} + \frac{q_s}{m_s}(\mathbf{E} + \frac{\mathbf{v} \times \mathbf{B}}{c}) \cdot \frac{\partial F_s}{\partial \mathbf{v}} = 0. \tag{1.15}$$

The charge density ρ_c and the current density $\mathbf{J}$ are given by the 0th and 1st order moments of the distribution function:

$$\rho_c(\mathbf{x}, t) = \sum_s q_s \int F_s(\mathbf{x}, \mathbf{v}, t)d\mathbf{v}, \quad \mathbf{J}(\mathbf{x}, t) = \sum_s q_s \int \mathbf{v}F_s(\mathbf{x}, \mathbf{v}, t)d\mathbf{v}. \tag{1.16}$$

We can then close the system, coupling eq. 1.15 and 1.16 with the Maxwell equations to solve the electromagnetic fields.

$$\nabla \cdot \mathbf{E} = 4\pi\rho_c \tag{1.17}$$

$$\nabla \cdot \mathbf{B} = 0 \tag{1.18}$$

$$\nabla \times \mathbf{E} = -\frac{1}{c}\frac{\partial \mathbf{B}}{\partial t} \tag{1.19}$$

$$\nabla \times \mathbf{B} = \frac{4\pi}{c}\mathbf{J} + \frac{1}{c}\frac{\partial \mathbf{E}}{\partial t}, \tag{1.20}$$

The above set of equations (1.15 to 1.20) constitute the Vlasov-Maxwell system of equation. This kinetic description of the plasma is very detailed and computationally heavy because not only it offers a microscopic description in time and in space of the plasma but also in the velocity space. Therefore it's a 6-dimensional (plus time) problem which incorporates all the times scales typical of plasmas, also those with high frequencies in the order of the cyclotron frequency ($\omega \sim \omega_{ci}$). The complexity and the presence of so many timescales require a lot of computational power to solve the fully kinetic description of a plasma.

It's possible to simplify this problem in different ways. A very well known one is obtaining fluid equations from the Vlasov-Maxwell set by considering moments of the distribution function. We will get a set of equations depending only on $(\mathbf{x}, t)$ which neglects the velocity space or kinetic effects. Nevertheless, such approach is extremely useful and powerful to find equilibrium and stability conditions for plasma configurations [8–10]. Such description goes under the name of MagnetoHydroDynamics (MHD) and will be briefly presented in the next section.

Another approach to simplify the Vlasov-Maxwell set of equation can be found doing some considerations on the plasmas we are interested in. The fast gyromotion of the

particles around the magnetic field (eq. 1.10) is included in the kinetic treatment shown above. In magnetized plasmas we can find many instabilities on very small timescales, at frequencies comparable to the cyclotron frequency $\omega \sim \omega_{ci}$. However, in fusion plasmas most of the phenomena of interest happen in a timescale much larger than the gyration period $\partial_t \ll \omega_{ci}$. Typically, also $\rho_L \ll L_B$ with $L_B = B/\nabla B$ is assumed as a spatial ordering, i.e. strongly magnetised plasmas. Hence, we can use a new framework where fast timescales are averaged and the fast gyromotion around the **B** field lines is neglected in order to reduce the number of dimensions and the complexity of computations and to neglect the small timescale phenomena. Such approach is called Gyrokinetic Theory and will be explained more in detail in section 2.1.

1.2.2 Fluid description: Magnetohydrodynamics

Magnetohydrodynamic or MHD theory is a powerful tool to describe the dynamics of electrically conducting fluids with or without external magnetic fields. MHD theory was first proposed by Alfvén [11, 12]. Such theory can be derived considering k^{th} order moments of eq. 1.15 [13]:

$$\int \underbrace{\mathbf{v} \cdot \mathbf{v} \cdot ... \cdot \mathbf{v}}_{k^{th} order} \left(\frac{\partial F_s}{\partial t} + \mathbf{v} \cdot \frac{\partial F_s}{\partial \mathbf{x}} + \frac{q_s}{m_s}(\mathbf{E} + \mathbf{v} \times \mathbf{B}) \cdot \frac{\partial F_s}{\partial \mathbf{v}} \right) d\mathbf{v} = \int \mathbf{v} \cdot \mathbf{v} \cdot ... \cdot \mathbf{v} \left(\frac{\partial F_s}{\partial t} \right)_{coll} d\mathbf{v}.$$
(1.21)

For each species s, the 0th order momentum of the Vlasov equation will yield the *mass continuity* equation, the 1st order one the *momentum balance* equation and the 2nd order one the *energy balance* equation. Closing the system with Maxwell equations, we can derive a two-fluid MHD model [9, 14, 15]. Such set of equation can be further simplified into the one-fluid MHD model [8], generally known as MHD model:

$$\textit{Continuity equation: } \frac{\partial n}{\partial t} + \nabla \cdot (n\mathbf{u}) = 0 \qquad (1.22)$$

$$\textit{Momentum equation: } \rho\frac{\partial \mathbf{u}}{\partial t} + \rho(\mathbf{u} \cdot \nabla)\mathbf{u} = -\nabla p + \frac{\mathbf{J} \times \mathbf{B}}{c} \qquad (1.23)$$

$$\textit{Energy equation: } \frac{\partial p}{\partial t} + (\mathbf{u} \cdot \nabla)p + \gamma p\nabla \cdot \mathbf{u} = (\gamma - 1)\eta J^2, \qquad (1.24)$$

where ρ is the density of the plasma, $\mathbf{u}$ is the plasma velocity, p the pressure, γ the adiabatic constant (for a plasma $\gamma = 5/3$), J is the absolute value of the current density $J = |\mathbf{J}|$ and $\eta = m_e\nu_e/(e^2 n_e)$ is the electric resistivity of the plasma. Equations 1.22 through 1.24 coupled with Maxwell equations 1.17 through 1.20 together with the

generalized Ohm's law:

$$\mathbf{E} + \frac{\mathbf{u} \times \mathbf{B}}{c} = \eta \mathbf{J}, \tag{1.25}$$

constitute a closed system of equations that can describe the dynamics of a resistant plasma. In some cases it's possible to approximate the plasma resistivity to be $\eta = 0$, in this case we can talk about *ideal* MHD.

As said this theory even if relatively simple is very useful for many applications. Solutions of the stationary MHD equations are the starting point of any device design [8] and can be evaluated with MHD, finding solutions to the momentum equation 1.23. For example, in Tokamaks this corresponds in finding solutions to the Grad-Shafranov equation [8, 16, 17] which is the poloidal component of eq. 1.23. Another application of MHD is studying the stability of small perturbations [8–10]. In fact, a magnetic configuration is never universally stable. Plasma equilibria are always affected by a huge variety of instabilities, this very thesis also inquires into two peculiar kinds of instabilities. Through various models derived from MHD it is possible to study threshold values, growth rates, frequencies of such modes.

Because of their combination between fluid dynamics and electromagnetic fields, plasmas are affected by an extremely large number of waves. For example, as it will be shown in section 2.4, a magnetized plasma is a medium for magnetic and magneto-sonic waves, where the local displacement of the plasma is coupled with the perturbation of the equilibrium magnetic field. These are the so called Alfvén Waves (section 2.4) and the magneto-sonic waves. The complexity of the geometries used for plasma confinement makes the variety of waves even richer, since in the same machines we observe an incredibly various range of plasma states and conditions. Some of these waves can be driven unstable by plasma characteristics as temperature, density and current profiles, or by kinetic effects of certain plasma populations as in the case of the present thesis. In fusion research, the study of these instabilities has been proved to be crucial. In fact, some of these instability, if not correctly mitigated, can lead to the disruption of the equilibrium state and the termination of the plasma.

Furthermore, MHD theory is used also to describe a variety of astrophysical plasmas [18] or other laboratory plasmas as for plasma thrusters [19]. In the next section we give a brief description of plasma confinement. It will be soon clear the importance of MHD theory to design such configurations and to evaluate their performances.

1.3 Magnetic Plasma Confinement

In this section the basics of magnetic plasma confinement will be briefly presented. Equation 1.5 is the condition to be achieved in order to reach reactor conditions. Considering that this equation is maximized for $T \sim 15 \ keV$ and therefore it can be considered as a fixed value, we can adjust the density or the confinement time to increase the triple product. The so called magnetic confinement exploits magnetic bottles and fields **B**, often coupled with drift or induced currents **J**, to generate Lorentz forces on the particles, 1.9. If **E** $= 0$ Lorentz force affects only the perpendicular motion of the particles and forces them to orbit around the magnetic field lines confining them. Such machines operate at relatively low densities in the order of $n \sim 10^{20} \ m^{-3}$ and relatively long confinement times $\tau \sim 0.1 - 1 \ s$.

Magnetic confinement approaches are the most used for fusion studies worldwide [20]. As mentioned above, such configurations have to somehow solve the momentum equation 1.23. In particular, if we assume stationary equilibria ($\partial_t = 0$) and the plasma to stand still (**u** $= 0$), the equilibrium condition reduces to:

$$\nabla p = \frac{\mathbf{J} \times \mathbf{B}}{c}. \tag{1.26}$$

From 1.26 we can infer that ∇p is perpendicular to both **B** and **J**, therefore the **B** and **J** lines lie on surfaces along which the pressure is constant. If we consider the stationary version of Ampére equation 1.20 and use it to substitute **J** in 1.26, we get:

$$\nabla \left(p + \frac{B^2}{8\pi} \right) = \frac{B^2}{4\pi} \hat{\boldsymbol{k}} \ , \tag{1.27}$$

where $\hat{\boldsymbol{k}} = (\hat{\mathbf{b}} \cdot \nabla)\hat{\mathbf{b}}$ is the magnetic field curvature vector, $\hat{\mathbf{b}}$ is the normalized magnetic field vector. From eq. 1.27 we notice that in order to counterbalance the plasma pressure a magnetic pressure and a magnetic curvature have to be applied. Furthermore, we notice that in case of a cylindrical configuration $\hat{\boldsymbol{k}} = 0$ we get $p + B^2/8\pi = const.$, so throughout the radius of the cylinder the plasma pressure p has to be counterbalanced by the magnetic pressure $B^2/8\pi$. Finally, we can introduce the kinetic to magnetic pressure ratio parameter:

$$\beta = \frac{p}{\frac{B^2}{8\pi}}. \tag{1.28}$$

The β parameter, often averaged over the control volume $\langle \beta \rangle_V$, is a figure of merit of the confinement, where $\langle ... \rangle_V$ is a volume integral. The higher β the better we exploit the confinement properties of **B** lines.

Given these basic tools of plasma equilibrium, we can move to the description of machines that can realize this equilibrium.

Pinches

One of the most basic ideas to confine a plasma is driving an axial current through a plasma. For example this can be achieved by applying a voltage to electrodes facing the plasma. The magnetic field that arise from the current via Ampére equation 1.20 couples with the current itself and drives a forces that confine the plasma according to 1.26. Such configuration is called z-pinch and has been studied thoroughly in many varieties [21, 22]. Z-pinches are intrinsically unstable due to $m = (0,1)$ sausage or kink modes [8, 21].Even though pinches have been discarded long ago as valid fusion device, the screw-pinch shape is often referred to as a simplified geometry to explain parameters and properties of tokamak plasmas.

In the event that magnetic lines terminate at a wall (as in the case of pinches), the plasma will come into contact with the wall, resulting in the dissipation of its energy. This occurs because the Lorentz force can not align parallel to the magnetic field, thus failing to prevent the collision between the plasma and the wall. This results into very low confinement times τ_e for pinches. To avoid this issue, the solution lies in creating magnetic lines that form closed loops and do not intersect the material wall. This configuration leads to a toroidal topology of magnetic field lines, which will be analyzed more thoroughly in the next section.

Toroidal machines

The fundamental concept is that a toroidal geometry enables magnetic field lines to be geometrically closed on themselves, leading to longer confinement times. In principle, particles could orbit indefinitely along the **B** lines. However, a simple configuration consisting solely of a toroidal axisymmetric field cannot maintain plasma equilibrium with the magnetic field [23]. This is due to the opposite velocity drifts experienced by electrons and ions produced by the gradient of the strength of the magnetic field (figure 1.3). In fact, in a purely toroidal configuration the magnetic field will be stronger closer to the rotation axis of the torus and weaker in the farther part of the torus. As the particles girate around magnetic lines they will be affected by a varying magnetic field resulting in differential Larmor radii in different point of the orbit. In particular the velocity drift produced will be:

$$\mathbf{v}_{\nabla B} = \frac{\mu}{q_s} \frac{\mathbf{B} \times \nabla B}{B^2} \ , \tag{1.29}$$

where $\mu = \frac{m\,v_{\perp}^2}{2B}$ is the magnetic moment of the particle. This causes the positive and negative charged particles to separate vertically and accumulate at opposite vertical ends, as displayed in fig. 1.3. As a result of these charge separations, an electric field is generated, inducing an E × B drift, similar to that explained above, that affects both ions and electrons alike:

$$\mathbf{v}_{E\times B} = \frac{\mathbf{E} \times \mathbf{B}}{cB^2} \ , \tag{1.30}$$

in fact, in equation 1.30, the direction of $\mathbf{v}_{E\times B}$ doesn't depend on the charge sign as in eq. 1.29. This particle drift causes the entire plasma to move outward, away from the axis of symmetry, resulting in the loss of plasma confinement. To achieve equilibrium where plasma pressure is balanced by magnetic forces, it is also necessary to incorporate a poloidal magnetic field.
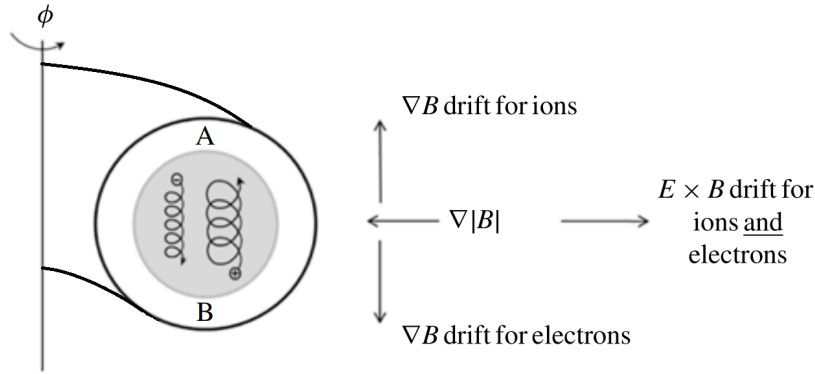
Figure 1.3: Purely toroidal axisymmetric field and consequent drifts. Adapted from [23]

The combined toroidal and poloidal magnetic fields result into a helical magnetic field, like in a "loop-screw-pinch", which generate opposing ∇B drifts for the same particle and prevents the loss of the plasma [5, 24]. Ultimately, in order to mitigate pressure and current-driven instabilities within the plasma and thereby enhance its confinement and stability, the implementation of a shear in the helical magnetic field becomes imperative [5]. A magnetic shear is produced by a radial variation of the inclination of the magnetic field lines. A more accurate definition of this will be given with the definition of safety factor profile in section 1.4.

There are two possible approaches to generate the poloidal component of the helical magnetic field within toroidal devices. The first method involves inducing a current in the plasma using Faraday's principle (as expressed in eq. 1.19). This is achieved by driving a current through a solenoid positioned at the center of the torus, effectively

utilizing the plasma as a one-loop secondary winding in a transformer. Consequently, the poloidal magnetic field is internally generated by the current flowing within the plasma itself. The machine adopting this principle is called Tokamak, a russian acronym which stands for "toroidal chamber with magnetic coils". This machine is axis-symmetric with respect to the toroidal axis. The details of this machine will be better described in section 1.4.

Alternatively, the poloidal component, as well as the rest of the helical **B** field, can be entirely generated externally by non-axisymmetric coils around the torus, eliminating the need for plasma current and enabling potentially steady-state plasma operations. This concept has been called *stellarator*. Although the stellarator is a potential candidate for future fusion reactors, its current performance, measured by the triple product (eq. 1.5), trails that of tokamaks [25, 26]. For a more complete description and understanding of the stellarator concept, the interested reader may refer to [27].

1.4 The Tokamak

The Tokamak was firstly introduced in Russia in 1958 [28]. In 1969, the russian tokamak T-3 was proved to have achieved an electron temperature up to $T_e = 1\,keV$ and confinement times up to tens of ms [29]. Such performances were a full order of magnitude higher than any other fusion device at the time. Tokamak technology spread quickly and, ever since, it is regarded as the most promising tool to achieve sustainable controlled fusion. In fact, the highest triple product has been achieved in tokamak machines [5, 30]. Being at the forefront of magnetic fusion research, today, two prominent tokamaks, ITER [31] and SPARC [32], are currently under construction. These ambitious projects aim to achieving D-T (deuterium-tritium) ignition, that is satisfying eq. 1.5, not yet achieved by any other magnetic fusion device, and conducting critical experiments with burning plasma. Both experiments are planned to start operation and produce relevant results within a decade.

Many other experimental tokamaks all over the world were or are being operated for scientific purposes. They play a crucial role in demonstrating feasibility of sustained fusion reaction, optimizing fusion reactor design, testing materials and components, and driving fusion technological development in general. The tokamak that will be referred to throughout this thesis is ASDEX-Upgrade [33], operated by Max Planck Society (MPG) in Garching, Germany. The ASDEX-Upgrade (AUG) tokamak leads in the development of plasma scenarios for future reactors due to its remarkable heating power-to-machine size ratio [34]. In some configuration, which is better described in sec. 3.2, this high power available to the plasma make the machine physics relevant for future burning plasma scenarios, in particular for Energetic Particles (EP) studies.

1.4.1 Tokamak components

As shown in 1.4, the main components of a tokamak are the central solenoid, for the generation of the plasma current, the toroidal field coils, for the generation of the toroidal magnetic field, and additional external poloidal coils, for the shaping of the plasma cross section and the control of the plasma. Additional components include:

- Heating systems:

  usually they include Electron Cyclotron Resonance Heating (ECRH), Neutral Beam Injection (NBI), and Ion Cyclotron Resonance Heating (ICRH). In AUG the NBI boxes have different orientations, allowing power release at various radial positions, including both on-axis and off-axis heating. This capability has been used in the thesis to explore the physics EP driven instabilities, see Chapter 4 and 5. The ECRH system utilizes metallic mirrors to change the heating positions by deflecting the beam angle. The ICRH antennas have fixed positions, with the location of heating power deposition varying based on the wave frequency and the magnetic field.

- Diagnostic systems:

  tokamaks employ several diagnostics to measure plasma parameters and performances. Thomson Scattering (VTA) [35] is the primary diagnostic for electron temperature measurement. Charge-Exchange Recombination Spectroscopy (CXRS) [36] is employed to measure ion temperature profiles through charge exchange reactions between injected neutral atoms and plasma ions. Electron cyclotron emission (ECE) is used to measure electron temperature from the cyclotron radiation produced by the gyration of electrons around magnetic field lines. Interferometry systems measure the plasma density computing the shift of phase in lasers due to the different plasma densities. Magnetic probes are essential diagnostics in a tokamak, providing information on the magnetic field and allowing the reconstruction of magnetic flux surfaces. Equilibrium codes use magnetic probe measurements to solve the Grad-Shafranov equation and derive plasma current, shape and stored energy.

- Control systems:

  tokamaks need sophisticated control systems which coordinate measurements and actuators to control plasma evolution and optimize its behavior. They include feedback controllers for parameter corrections and a pulse supervisor to handle exceptional situations. The control system and pulse supervisor dynamically adjust experimental conditions to achieve physical goals and reproduce expected parameter trajectories during a discharge.

- Vacuum, pumping and fueling systems:

  in tokamaks there's the need to pump out of the machine impurities or, in the future, fusion products and keep feeding in the plasma the reactants. To these purpose, vacuum and crio pumps are installed to achieve the extremely low vacuums needed for the correct functioning of these machines ($\sim 10^{-6}\ Pa$). Meanwhile, puffing and pallet injection systems are installed to fuel the plasma with reactant species (D, H or He in experimental devices and D-T mixtures in reactors).
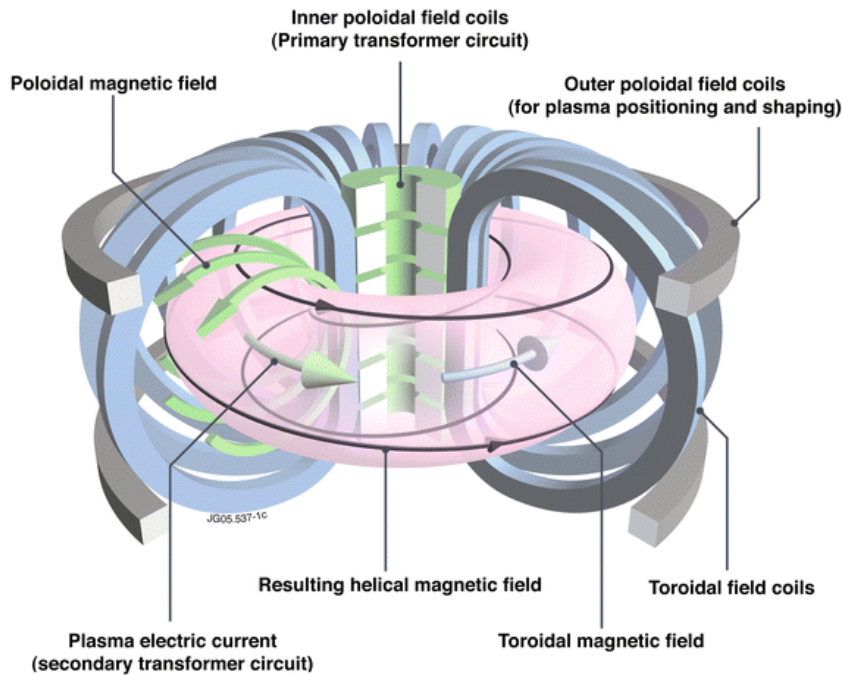
Figure 1.4: Tokamak scheme with coils, taken from [37]

major radius, R_0	1.65 m
minor radius, a	0.5 m
plasma current, I_p	$< 1.2\ MA$
toroidal magnetic field, B_t	$< 3.2\ T$
heating power, P_{in}	$< 30\ MW$
electron density, n_e	$<10^{20}\ m^{-3}$
ion temperature, T_i	$<8\ keV$

Table 1.1: Typical plasma parameters of AUG

1.4.2 Tokamak geometry

The size of a tokamak is characterized by a major radius, R_0, and a minor radius, a, which can be used to calculate the inverse aspect ratio, $\epsilon = a/R_0$. Given the toroidal geometry of the tokamak, two angular coordinates can be used to describe it, a toroidal angle ϕ and a poloidal one θ (fig. 1.5.a). The magnetic field is made up of two contributions along these directions: a dominant toroidal one, B_ϕ, produced by external coils, and a poloidal component, $B_\theta < B_\phi$, generated by an induced toroidal plasma current (fig. 1.5). The shape of the poloidal cross-section of the magnetic equilibrium can have a degree of elongation, $k \geq 1$ quantifying its numerical definition. The combination of these magnetic fields gives rise to nested surfaces, with field lines following a helical path along these surfaces. The helicity of the field lines is quantified by the safety factor profile q, which indicates the average of the change rate of the θ angle with respect to ϕ along a field line at different radial points:

$$q(r) = \frac{1}{2\pi} \int_0^{2\pi} \frac{\mathbf{B} \cdot \nabla \phi}{\mathbf{B} \cdot \nabla \theta'} d\theta', \tag{1.31}$$

in a simplified screw-pinch geometry, this can be approximated by: $q = rB_\phi/(R_0 B_\theta)$ [5, 8].

In a realistic non-circular geometry, the exact equilibrium is numerically calculated by solving the Grad-Shafranov equation. This equation finds an ideal equilibrium (neglecting resistivity) between the plasma pressure p and the magnetic field, with field lines lying on nested toroidal surfaces (magnetic surfaces), as previously shown in eq. 1.26. An alternative way to describe the geometry of a tokamak is through the poloidal magnetic flux function [8]:

$$\Psi = \frac{1}{2\pi} \int_{S_\Psi} \mathbf{B} \cdot d\mathbf{S} \tag{1.32}$$

figure 1.5.b clearly shows how this integral is obtained. Usually Ψ is used as a radial coordinate. This function remains constant on the magnetic surfaces at constant pressure. For completeness we can also define a toroidal flux function [8], as represented in fig. 1.5.a:

$$\Phi = \frac{1}{2\pi} \int_{S_\Phi} \mathbf{B} \cdot d\mathbf{S} \tag{1.33}$$
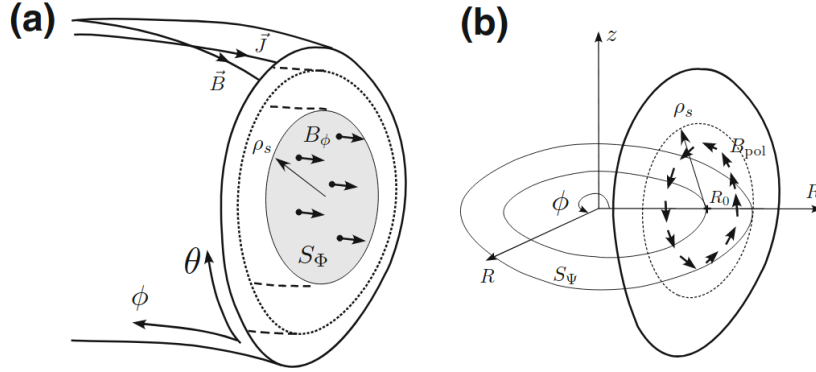
Figure 1.5: **a**) **J** and **B** lines surfaces of constant pressure. The toroidal magnetic flux Φ determined by the integral of the toroidal magnetic field B_ϕ on the S_ϕ area. **b**) The poloidal magnetic flux Ψ is defined by the integral of the poloidal magnetic field B_{pol} on the S_Ψ area. The magnetic axis is denoted as R_0. Taken from [24]

After discussing the significance of nuclear fusion research in tokamaks, we can now approach the specific research area addressed in this thesis, which is the study of energetic particle instabilities in tokamaks. Charged particles interact electromagnetically with each other and with the fields in a tokamak. These interactions can give rise to collective behavior among the particles, leading to both microscopic and macroscopic plasma instabilities. The focus of this thesis is on two kind of macroscopic instabilities that are commonly measured in reactor-relevant tokamak experiments, where large populations of EP are observed. EPs generated from NBI systems have characteristic velocities close both to the thermal speed and the Alfvén velocity. Therefore they can resonate and excite both an acoustic instability: the Geodesic Acoustic Mode (GAM), and a magnetic one: the Alfvén Wave (AW).

Furthermore, it is of capital importance to notice that the toroidal geometry, simply because the coils are disposed in a "denser" way near the axis of the machine, as clearly shown in figure 1.4, generates a $1/R$ dependence of the toroidal magnetic field B_ϕ. Therefore a particle, orbiting along a magnetic field line will experience a gradient in parallel magnetic field due to this toroidicity effect. Considering that for an unperturbed trajectory, a particle will conserve its energy ε:

$$\varepsilon = \frac{v_\parallel^2 + v_\perp^2}{2} = const \ , \tag{1.34}$$

and its so called magnetic moment μ:

$$\mu = \frac{mv_\perp^2}{2B} = const \ , \tag{1.35}$$

as the particle travels along the magnetic line going toward the inner part of the torus it will experience an increase in the module of B, according to the conservation of eq. 1.35, $v_\perp$ needs to increase too. Subsequently, according to expression 1.34, if $v_\perp$ increases then $v_\parallel$ must drop. In some cases particles don't have enough energy to overcome this magnetic well and get reflected backwards along the magnetic line. The particle which cannot travel to the high field side (HFS) of the tokamak are called *trapped*. On the contrary, if they have enough parallel velocity they will go all around the poloidal direction (even if slowing down in the HFS) and will be called *passing*. More details about these populations of particles can be found in [38].

An example of such orbits is shown in figure 1.6. It is interesting to observe that the trapped particles exhibit a particular orbit shape called *banana orbit*, red trajectory in fig. 1.6. This shape is due to the conservation of a third quantity called toroidal momentum [38]:

$$P_\phi = mRv_\phi - q_s\psi = const .\tag{1.36}$$

We see that if the toroidal velocity v_ϕ varies, as we have seen, along the trajectory then the radial coordinate of the particle ψ has to change in order to maintain eq. 1.36 true. The consequence is that we see a radial displacement in both the trapped and passing orbits as they go around the poloidal angle.
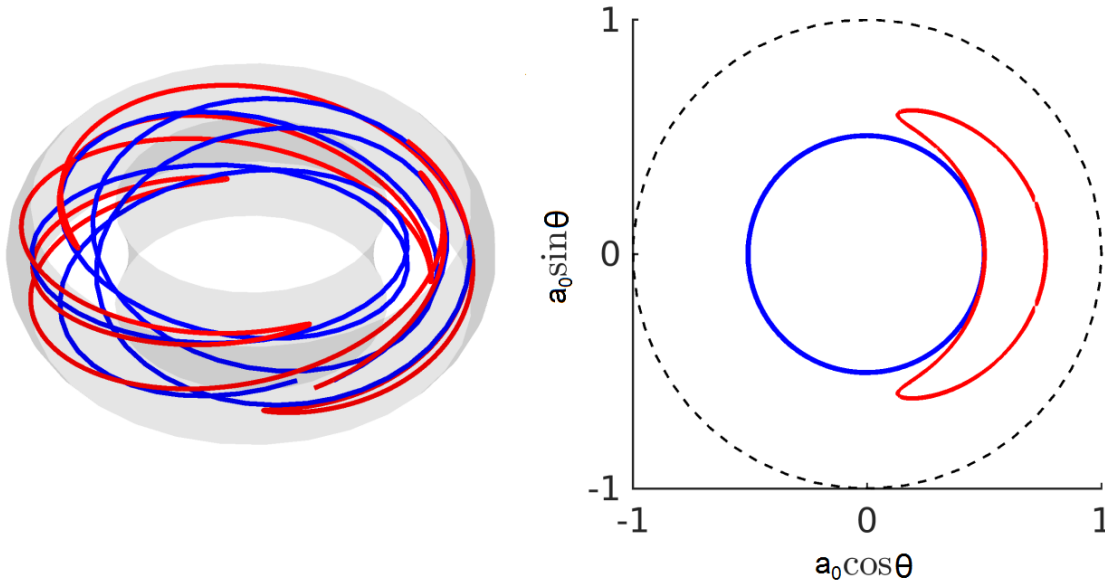
Figure 1.6: Passing (in blue) and trapped (in red) particles trajectories in toroidal configuration (left) and in a poloidal plane projection (right). Adapted from [39]

Finally, a last distinction in the particle populations is between the bulk plasma and energetic particles. Energetic Particles (EPs) are an ion species with suprathermal velocities $v_{th,EP} \ll v_{th,i}$, where $v_{th,EP}$ is the thermal velocity of EPs and $v_{th,i}$ is the thermal velocity of bulk ions. We will se more details about this plasma species in sections 1.5 and 2.2.

1.5 Energetic Particle Instabilities and Motivation

Study and confinement of energetic particles (EPs) is crucial for the development of future fusion reactors. In the burning plasma regime, fusion products are the primary source of plasma heating. Therefore, confining EPs for long enough times is fundamental for energy transfer to bulk species [40]. As described in the previous section, current machines use ICRH or neutral beam injectors NBI to generate EPs, which have different anisotropic non-Maxwellian phase-space distribution functions due to their low collisionality and exist far from thermal equilibrium [41, 42]. Such distributions are also very different from those originating from fusion products, anyhow they can still drive the above mentioned EP instabilities. Our long-term goal is to predict the self-organisation of a burning fusion plasma, considering cross-scale and mode coupling phenomena. Thus we can use present day experiments to validate the models to predict non-linear EP dynamics related to experimental-like EP distribution functions. In the present work we develop and test numerical tools to analyze physical phenomena characteristic of burning plasmas which can be reproduced on different scales in present day machines which are not yet reactors (refer to section 3.2 for details about this EP study relevant experimental set-up). As it will be clear from the present section, it is very important to validate numerical codes, including step by step more phenomena and experimental relevant features to advance in the capabilities to simulate such scenarios.

In this section we preliminary introduce the nature of the instabilities we are going to study in the present work (section 1.5.1), then we present the complexity of the problem and the effort done in the past to reconstruct the EP dynamics (sec. 1.5.2). Finally we explain the relevance of the work presented in this thesis in the framework of EP dynamics studies in section 1.5.3. After it we will outline the goals of the thesis and its results (section 1.6).

1.5.1 EP instabilities

EP-driven modes, which are formed by Alfvén Waves (AW) [43] and Energetic-particle driven Geodesic Acoustic Modes (EGAM) [44], can be excited by EPs and harm

confinement by redistributing them in velocity and real space [45, 46]. Linear excitation of EGAMs ($n = 0$ mode) exclusively requires velocity-space gradients of the distribution functions F_0, so that the mode can be driven by inverse Landau damping [47]. Hence, anisotropic EP F_0 are needed to linearly drive EGAMs unstable [48–50]. EGAMs can redistribute particles in phase space [46], representing a valid mechanism to exchange energy between EPs and bulk ions [48, 51, 52] and can be used to regulate turbulence [53]. A detailed explanation of the physics behind this kind of instability is offered in section 2.3 in Chapter 2. Whereas Alfvén Waves can be excited both by anisotropic and isotropic distribution functions. In fact, radial gradients in EP F_0 can also represent a driving force for $n > 0$ modes [47]. AWs can redistribute particles before their thermalization with the bulk plasma, leading to severe heat losses and eventually to damaging the machine. In particular, they are believed to be the cause for the so called abrupt large-amplitude events (ALE), observed in JT-60U [54–56]. The details of the physics of AWs is presented in section 2.4 in chapter 2. Furthermore, AWs and EGAMs are coupled non-linearly via EP non-linear response [57–59]. For details about this non-linear wave-wave coupling refer to section 2.5. The work hereby presented shows that such physical mechanism is fundamental to reconstruct experimental observations of AWs and EGAMs in ASDEX-Upgrade [50, 59].

1.5.2 State of the Art

Understanding the EP dynamics is a great challenge in the pathway to effective and efficient nuclear fusion reactors. The large EP Larmor radius and drift orbit width and the expected pressure contribution related to EPs in burning plasma scenarios ($\beta_{EP} \sim \beta_{th,i}$) make EPs a very important topic for reactor confinement. Because of these characteristics, EPs are crucial in the coupling between microscopic and macroscopic plasma phenomena [60, 61]. Furthermore, saturated EP-driven instabilities (such as AWs) will produce anomalous EP radial transport, potentially harming severely the confinement [45]. As we see, EPs have multiple channels to reach non-linear saturation, either through wave-particle or through wave-wave interactions. The goal is to determine what phenomena are dominant in which scenario.

In fact, in order to study all these phenomena we need models which necessarily retain the following features:

- Electromagnetic physics: in order to capture the magnetic nature of many phenomena (e.g. AWs).

- Non-linear physics: this is needed to study the coupling among different cross-scale instabilities (e.g. meso-scale AWs with meso-scale ZS or micro-scale drift wave turbulence) and the transport associated with the saturation of the modes.

- Global perspective: needed to correctly evaluate the impact of the realistic mode spatial structures on the non-linear wave-wave interactions or on the self-consistent radial transport associated with the wave-particle saturation channel.

- Kinetic treatment: needed to capture the kinetic nature of most of this EP-mediated phenomena and the crucial phase-space effects of distribution functions on the drive of modes. It is, therefore, compulsory the use of fully gyrokinetic (GK) or GK-MHD hybrid codes with realistic distribution functions.

Not only, in order to evaluate a correct hierarchy of these phenomena and produce consistent and valid reduced models, we need to consider all this physics at the same time on very different times scales, characteristic of the different phenomena we want to study (e.g. the high frequency dynamics of meso-scale instabilities as AWs and the low frequency of micro-scale turbulence).

So far the development of these models was focused on only one phenomena at a time, limiting the simulations only to certain time scales, or mode numbers or running single flux tube simulations. For example, so far, in this EP framework, previous studies focused only either on the linear drive of EGAMs by double bump-on-tail distribution functions [48, 49] or study on linear dynamics or non-linear saturation of AWs alone [62, 63].

In order to achieve the goals mentioned above we have to run these GK, global, electromagnetic, non-linear codes over very long periods. The code ORB5 has a prominent importance in the development of these tools. Only recently, work was started to enquire into the non-linear coupling mechanisms [50, 58, 59]. In reference [58] we have an example of this attempt. The work presented in this thesis is a more experimental relevant case of this multi-mode simulation effort, see details in chapter 5. With the results obtained in this thesis we paved the way to the possibility of advancing in the integration of multiple instabilities in the same simulation. As already said, the final goal is to reach the capability of global simulations of burning plasmas.

A very interesting method is currently being elaborated to overcome the challenges of current numerical frameworks when dealing with long-time- scales and non-local behaviors. This is a Phase-spaze zonal structure (PSZS) transport theory [64–67]. This theory generalizes the concept of plasma transport into the phase-space by offering the definition of the plasma non-linear equilibrium distribution function considering slowly evolving structures in phase-space. In the future, with this method, it will be possible to reconstruct evolving non-linear equilibria and implement them in GK codes (like ORB5), enabling them to run simulations over long time-scales with little noise. The idea is to integrate the GK codes, which yield a description of the non-linear global perturbations and their saturation mechanisms, into a reduced EP transport model

based on PSZS theory for the analysis of present experimental measurements and the fully predictive simulation of future burning plasmas.

Finally, it's very important to remind that for all these non-linear phenomena we can use the theory developed in literature for the interpretation of the numerical results. In some cases, we also can have dedicated experiments (as in this work) to which we can refer for the validation of our codes. It is only in this on-going comparison between theory, numerical simulations and experimental observations that we will be able to develop models capable of fully reconstruct the dynamics of EP in a burning plasma scenario. On a small scale, this is what has been done in this thesis as it is more clearly state in the next section.

1.5.3 Motivation

Because of the importance of EP dynamics for future reactors, it is crucial to develop and experimentally validate models that are able to reconstruct these phenomena [68]. Gyrokinetic tools (see Chapter 3) are particularly suitable to enquire into such studies [68, 69]. Also, in present day machines, and in particular in ASDEX-Upgrade, experiments can be set up to maximize the EP physical effects, as in the so called NLED-AUG case [70, 71]. It is possible to detect frequency and spatial information from experimental observations of EP driven modes [72], this allows to do comparisons between observations and simulations. The purpose of this thesis is to advance in the predictive capability of the gyrokinetic code ORB5 [69] to simulate this non-linear EP dynamics in experimental relevant scenarios [50, 58, 59, 68, 73]. In particular, we aim to do so by studying and trying to reproduce the experimental EP dynamics from the NLED-AUG case. Particularly in this case, as elaborated in in section 3.2 and Chapter 5, our objective is to determine the predominant phenomenon within the given experimental scenario. This implies determining whether it is the linear driving mechanism of GAMs or the non-linear interaction between AWs and ZS to regulate the EP dynamics observed in ASDEX-Upgrade (see section 3.2), utilizing a distribution function that closely represents the EP experimental like conditions. As previously highlighted in section 1.5.2, this attempt represents a novel challenge. Until now, the focus within the ORB5 code framework has predominantly been on studying single instabilities, often disregarding the use of experimentally relevant EP distribution functions. This endeavor marks a significant step toward understanding the intricate, non-linear, multi-mode, multi-scale and global nature of EP dynamics. To this goal the present work compares ORB5 simulations of NLED-AUG case in ASDEX-Upgrade [50, 58, 59] with the available analytical theory and experimental measurements.

1.6 Thesis scope and outline

This thesis enquires into the consequences of using different EP distribution functions in gyrokinetic simulations to analyze the linear and non-linear behaviour of two instabilities (EGAMs and AWs) and their coupling in ASDEX-Upgrade. This case involves investigating the linear driving of EGAMs and the complex, non-linear interaction between AWs and ZS. This research also aims to determine which of these phenomena is dominant in the given experimental context. In particular, we study the effect of adopting experimental-like, anisotropic EP distribution functions, both analytical and numerical ones, which is a novel approach.

The structure of the thesis is as follows: in Chapter 2 we provide the reader with the main theoretical background. First of all, gyrokinetic theory is introduced in section 2.1. In sec. 2.2 EP features and dynamics will be outlined. After that, the GAM dispersion relation and the linear drive mechanism are presented in sec. 2.3, as well as the AW dispersion relation and characteristics in sec. 2.4. Finally, non-linear interactions between AWs and EGAMs are discussed in sec. 2.5.

In Chapter 3, we present the numerical tools and framework used for the simulations. In sec. 3.1 the gyrokinetic model for ORB5 used for our calculations is briefly introduced, consequently, an overview of the features of the code is offered. In section 3.2 we describe the experiment in ASDEX-Upgrade from which we derived our numerical setup for our simulations. We then show the newly implemented anisotropic distribution functions in sec. 3.3.

Chapter 4 produces the results of linear excitation studies for EGAMs using the new F_0. The results for the analytical F_0 are presented in sec. 4.3, those for the numerical F_0 in sec. 4.4. A first comparison with experiments is offered in sec. 4.4.4.

In Chapter 5, we show the non-linear, electromagnetic simulation results, where AWs were included in the simulations and allowed to interact with EGAMs. Firstly, the results for the analytical distribution function were shown in sec. 5.2, and then for the numerical one in sec. 5.3. In sec. 5.4 a new, more accurate, comparison between non-linear simulations and experimental observation is performed.

Finally, in Chapter 6, a summary, conclusions and open issues of the thesis will be presented. A glimpse on future perspectives will be given.

2 Theoretical background

After having shown the importance of the field and having pointed out the relevance of the topic hereby treated, we provide the reader with the basic tools to understand the theoretical basis of the work carried out in this thesis. To this purpose we will introduce the gyrokinetic theory (section 2.1), backbone of the code we used for our simulations, ORB5, and main pillar for studies of the kinetic plasma dynamics. Afterward we will describe the general behavior of energetic particles (section 2.2). Subsequently, we introduce the two EP driven instabilities we will discuss in this thesis (sections 2.3, 2.4). Finally, we describe the non-linear interaction phenomena which regulate the coupling between Alfvén Waves and Zonal Structures (section 2.5).

2.1 Gyrokinetic theory

Gyrokinetic theory is a simplified kinetic description of a magnetized plasma, that allows for faster computations. In fact, the aim of the gyrokinetic transformation is to bring the 6-dimensional motion of a charged particle in a magnetized plasma to a 5-dimensional one, conserving the drifts and the effects of field perturbations up to a certain order. The description of the whole procedure and derivation of this theory goes beyond the scope of this thesis, the interested reader may refer to [74–76]. Usually the gyrokinetic framework can be obtained as a two steps derivation. First, starting from the single-particle Lagrangian, the so called guiding center transformation is performed [77]. That brings the actual particle position to the instantaneous guiding center, considering zero perturbations in the external fields and retaining only the spatial geometry and gradients of the magnetic field. This is obtained by subtracting the gyroradius from the particle position as shown in fig. 2.1.
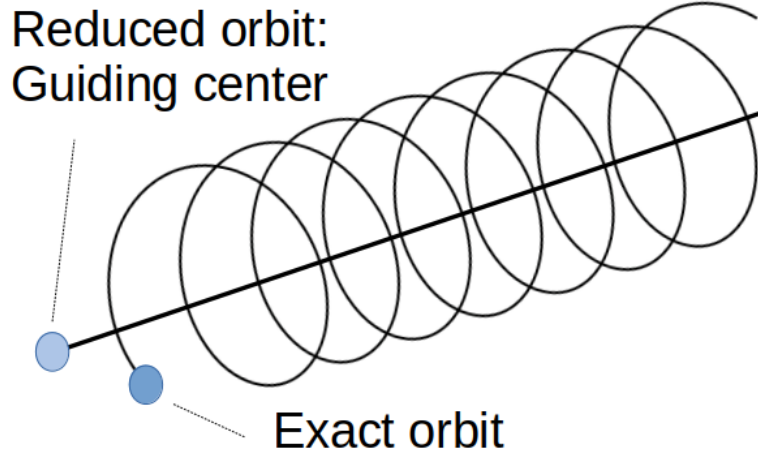
Figure 2.1: Visualization of the transformation from the exact orbit of the particle to the guiding center: the fast gyromotion around the magnetic field line is averaged

The position of the guiding center will follow primarily the parallel motion along the magnetic field lines, but, at higher orders, it will also follow directions perpendicular to the field lines due to the well known drift motions and the finite Larmor radius effects. Therefore, the new set of coordinates is wanted to be independent of the gyroangle variable:

$$\mathbf{Z} = \underbrace{(\mathbf{x}(\theta), v_{\parallel}(\theta), \mu(\theta), \theta)}_{\text{local coordinates}} \longrightarrow \mathbf{Z}_{gc} = \underbrace{(\mathbf{R}(\cancel{\theta_{gc}}), v_{\parallel,gc}(\cancel{\theta_{gc}}), \mu_{gc}(\cancel{\theta_{gc}}), \theta_{gc})}_{\text{guiding center coordinates}}, \qquad (2.1)$$

where the *gc* pedex indicates that the coordinates are the guiding center coordinates, $\mathbf{R}$ is the guiding-center position of the particle such that $\mathbf{x} = \mathbf{R} + \boldsymbol{\rho}(\theta)$, $v_{\parallel}$ is the parallel velocity of the particle, μ is the magnetic moment of the particle. Whereas $z^{\alpha} = z^{\alpha}(\theta)$, in the guiding center system we have $z^{\alpha}_{gc} \neq z^{\alpha}_{gc}(\theta_{gc})$. If we manage to find a transformation capable of realizing 2.1, the dynamics of the set of the first five coordinates will be solvable independently of the last one θ_{gc}, the gyroangle. This transformation is obtained by writing the Lagrangian of a charged particle, under the hypothesis of a magnetized plasma: $\epsilon_B = \rho_L/L_B \ll 1$, with ρ_L Larmor radius and $L_B = |\nabla B/B|_{max}^{-1}$. We will make use, at different orders of ϵ_B, of the Lie Transform methods: $\Gamma = e^{G_z}\gamma + dS$ [75], where γ is the 1-form Lagrangian, G_z the generating field and S an arbitrary scalar for the gauge invariance. By introducing and assigning the free variables we can decouple the dependency of the coordinates from θ and conserve energy

and momentum. By applying all these transformations we yield the guiding-center Lagrangian [77] (the *gc* pedex is dropped for simplicity):

$$\mathcal{L}_{gc}(\mathbf{R}, v_\parallel, \mu, \theta) = (\frac{q_s}{c}\mathbf{A} + mv_\parallel\mathbf{b}) \cdot \dot{\mathbf{R}} + \frac{m_s c}{q_s}\mu\dot{\theta} - \left(\frac{mv_\parallel^2}{2} + \mu B\right), \qquad (2.2)$$

where $\mathbf{A}$ is the magnetic vector potential: $\nabla \times \mathbf{A} = \mathbf{B}$. We can obtain the characteristic of the particles and therefore the tools to write the guiding center Vlasov equation by writing the action of the Lagrangian and taking the derivative of it with respect to the coordinate. The explicit passages to do this are shown below for the gyrocenter transformation, since the two processes are very similar. Alternatively, we could also write the 2-form Lagrangian and evaluate the Poisson-bracket of this new system and then apply it to the coordinates to obtain their characteristics [78].

As a second step, the time fluctuations of the electric potential $\delta\varphi$ and the magnetic one $\delta\mathbf{A}$ are introduced in the model [75, 79]. The smallness parameter associated with these fluctuations is $\epsilon_\delta = e\delta\varphi/T \sim \delta B/B$, such that $\epsilon_B = \epsilon_\delta^2$, which is a common approach in many gyrokinetic codes (see sec. 3.1). As previously, we want to find a transformation as in 2.1, but this time to the gyrocenter coordinates, which take into account the aforementioned electromagnetic perturbations:

$$\mathbf{Z} = \underbrace{(\mathbf{x}(\theta), v_\parallel(\theta), \mu(\theta), \theta)}_{\text{local coordinates}} \longrightarrow \mathbf{Z}_{gy} = \underbrace{(\mathbf{R}(\theta_{\cancel{gy}}), p_z(\theta_{\cancel{gy}}), \mu_{gy}(\theta_{\cancel{gy}}), \theta_{gy})}_{\text{gyro center coordinates}}, \qquad (2.3)$$

This can be accomplished as before taking in account in the Lie Transformations the perturbations in the electromagnetic potentials. The pedex *gy* will be dropped from now on for simplicity sake. We hypothesize that the perpendicular vector potential is zero: $A_\perp = 0$, leaving $\delta\mathbf{A} \simeq \delta A_\parallel\mathbf{b}$. The electromagnetic perturbations break the time conservation of μ. In order to restore it similar Lie-transforms are applied and using the Hamiltonian representation at the second order the following gyrocenter particle lagrangian is yielded [75, 79]:

$$\mathcal{L}_{gy}(\mathbf{R}, p_z, \mu, \theta) = \frac{q_s}{c}\mathbf{A}^*(\mathbf{R}) \cdot \dot{\mathbf{R}} + \frac{m_s c}{q_s}\mu\dot{\theta} - H_0 - \epsilon_\delta H_1 - \epsilon_\delta^2 H_2, \qquad (2.4)$$

where p_z is the canonical gyrocenter momentum:

$$p_z = mv_\parallel + \frac{q_s}{c}\langle\delta A_\parallel(\theta)\rangle_\theta, \qquad (2.5)$$

The gyro average over the fast gyromotion is represented by the notation $\langle...\rangle_\theta$. It can be defined for a general function dependent on the gyroradius and consequently the

gyroangle $F(\mathbf{R} + \boldsymbol{\rho}(\theta))$ in order to cancel its dependence on the gyromotion:

$$\langle F(\mathbf{R} + \boldsymbol{\rho}(\theta)) \rangle_\theta = \frac{1}{2\pi} \int_0^{2\pi} F(\mathbf{R} + \boldsymbol{\rho}(\theta)) d\theta . \tag{2.6}$$

In the so called *drift-kinetic* approximation, the gyroaverage is not computed for the particle: the quantity is approximated to be the one computed at the guiding center position. In other words: $\langle F(\mathbf{R} + \boldsymbol{\rho}(\theta)) \rangle_{\theta,dk} = F(\mathbf{R})$. The extended magnetic potential $\mathbf{A}^*$ is defined as:

$$\mathbf{A}^* = \mathbf{A} + \frac{c}{q_s} p_z \mathbf{b}. \tag{2.7}$$

We can consequently also define an extended magnetic field:

$$\mathbf{B}^* = \nabla \times \mathbf{A}^* = \mathbf{B} + \frac{c}{q_s} p_z \nabla \times \mathbf{b} . \tag{2.8}$$

The particle Hamiltonian H is decomposed in its different orders: $H = H_0 + H_1 + H_2$, where, in the long wavelength approximation, each of them is defined as:

$$H_0 = \frac{p_z^2}{2m} + \mu B , \tag{2.9}$$

$$H_1 = q \left(\langle \delta\varphi \rangle_\theta - \frac{p_z}{m_s c} \langle \delta A_\parallel \rangle_\theta \right) , \tag{2.10}$$

$$H_2 = \frac{q_s^2}{2m_s c^2} \langle \delta A_\parallel \rangle^2 - \frac{m_s c^2}{2B^2} |\nabla \delta\varphi|^2 . \tag{2.11}$$

Integrating the particle Lagrangian (eq. 2.4) multiplied by the distribution function F_s over velocity space dW and real space dV and summing it to the field Lagrangian $\int (\delta\mathbf{E}^2 - \delta\mathbf{B}^2)/8\pi dV$, discarding the electric field perturbation because of the *quasi-neutrality* approximation [79], we yield the total gyrokinetic Lagrangian of the system up to $\mathcal{O}(\epsilon_\delta^2)$ contributions:

$$L = \sum_s \int \left(\left(\frac{q_s}{c} \mathbf{A}^*(\mathbf{R}) \cdot \dot{\mathbf{R}} + \frac{m_s c}{q_s} \mu \dot{\theta} - H_0 - \epsilon_\delta H_1 \right) F_s - \epsilon_\delta^2 H_2 F_{0,s} \right) dW \, dV - \epsilon_\delta^2 \int \frac{|\nabla \delta A_\parallel|^2}{8\pi} dV .$$

$$\tag{2.12}$$

In equation 2.12 we decomposed the total distribution function of a particle species into an equilibrium distribution function and a perturbation distribution function, this also has a smallness parameter ϵ_δ associated to it: $F_s = F_{0,s} + \epsilon_\delta \delta f_s$. Therefore, in eq. 2.12, we discarded the $\epsilon_\delta^3 H_2 \delta f_s$ term because of third order $\mathcal{O}(\epsilon_\delta^3)$.

We can find the characteristic and field equations using a variational approach [80, 81]. We can define a gyrokinetic action functional, integrating in time the total Lagrangian from eq. 2.12:

$$\mathcal{A}(\mathbf{Z}, \delta\varphi, \delta A_\parallel) = \int_{t_1}^{t_2} L(\mathbf{Z}, \delta\varphi, \delta A_\parallel) dt. \tag{2.13}$$

In order to get the gyrokinetic characteristic and field equations we can consider the minimization of a functional derivative of the action $\mathcal{A}$ in eq. 2.13 with respect to a certain function η multiplied by an arbitrary test function $\hat{\psi}$:

$$\frac{\partial \mathcal{A}}{\partial \eta}\hat{\psi} = \frac{d}{d\epsilon}\left[\int \mathcal{L}(\eta + \epsilon\hat{\psi}, \nabla\eta + \epsilon\nabla\hat{\psi})dW\,dV\,dt\right]_{\epsilon=0} = \tag{2.14}$$

$$= \int \left(\frac{\partial \mathcal{L}}{\partial \eta}\hat{\psi} + \frac{\partial \mathcal{L}}{\partial \nabla\eta}\nabla\hat{\psi}\right) dW\,dV\,dt = 0. \tag{2.15}$$

The equations of motion of a particle can be found by minimizing the action integral with respect to the particle phase-space coordinates $\mathbf{Z} = (\mathbf{R}, p_z, \mu, \theta)$ [80, 81]. From such minimization we can obtain the Euler-Lagrange equations for the particle [81]:

$$\frac{d}{dt}\frac{\partial \mathcal{L}_{gy}}{\partial \dot{Z}_\alpha} = \frac{\partial \mathcal{L}_{gy}}{\partial Z_\alpha}. \tag{2.16}$$

Substituting every gyrokinetic coordinate in equation 2.16 we get the particle characteristic equations:

$$\dot{\mathbf{R}} = \frac{\mathbf{B}^*}{B_\parallel^*}\frac{\partial}{\partial p_z}(H_0 + \epsilon_\delta H_1) + \frac{c\mathbf{b}}{qB_\parallel^*} \times \nabla(H_0 + \epsilon_\delta H_1), \tag{2.17}$$

$$\dot{p}_z = -\frac{\mathbf{B}^*}{B_\parallel^*} \cdot \nabla(H_0 + \epsilon_\delta H_1), \tag{2.18}$$

$$\dot{\mu} = 0, \tag{2.19}$$

$$\dot{\theta} = \omega_c, \tag{2.20}$$

where $B_\parallel^* = \mathbf{B}^* \cdot \mathbf{b}$. Again because of the third order generated by $F_s H_2$, the dependence from H_2 is lost. As imposed, the magnetic moment μ becomes an adiabatic invariant again. We can rewrite equations 2.17 to 2.20 extensively, expliciting the values of the Hamiltonians H_0 and H_1 from equations 2.9 and 2.10. We can do that by splitting the different contributions from the different orders:

$$\dot{\mathbf{R}} = \dot{\mathbf{R}}^{(0)} + \epsilon_\delta \dot{\mathbf{R}}^{(1)} \, , \tag{2.21}$$

$$\dot{p_z} = \dot{p_z}^{(0)} + \epsilon_\delta \dot{p_z}^{(1)} \, , \tag{2.22}$$

$$\dot{\mu} = 0 \, . \tag{2.23}$$

The 0th-order derivatives are the so called unperturbed trajectories:

$$\dot{\mathbf{R}}^{(0)} = \underbrace{\frac{p_z}{m}\mathbf{b}}_{=\mathbf{v}_\parallel} + \underbrace{\left(\frac{p_z}{m}\right)^2 \frac{mc}{qB_\parallel^*}\mathbf{b} \times \frac{\nabla B}{B}}_{=\mathbf{v}_{curv\mathbf{B}}} + \underbrace{\frac{c\mu B}{qB_\parallel^*}\mathbf{b} \times \frac{\nabla B}{B}}_{=\mathbf{v}_{\nabla B}} - \underbrace{\left(\frac{p_z}{m}\right)^2 \frac{cm}{qB_\parallel^*}\mathbf{b} \times \left(\mathbf{b} \times \frac{\nabla \times \mathbf{B}}{B}\right)}_{=\mathbf{v}_{\nabla p}} \, , \tag{2.24}$$

$$\dot{p_z}^{(0)} = -\mu\frac{\mathbf{B}^*}{B_\parallel^*} \cdot \nabla B = -\mu\frac{m}{p_z}(\mathbf{v}_\parallel + \mathbf{v}_{curv\mathbf{B}} + \mathbf{v}_{\nabla p}) \cdot \nabla B, \tag{2.25}$$

in 2.24 $v_\parallel$ is the 0th order component of the velocity parallel to $\mathbf{B}$. The other contributions are perpendicular to $\mathbf{B}$: $\mathbf{v}_{curv\mathbf{B}}$ and $\mathbf{v}_{\nabla B}$ are the drift velocities due to the curvature and the gradient of the magnetic field and, in general, account for the drifts due to the magnetic geometry. Finally, $\mathbf{v}_{\nabla p}$ is the so-called diamagnetic drift caused by the gradient of the pressure. In fact, combining equation 1.20 and 1.26 we yield: $\mathbf{b} \times (\nabla \times \mathbf{B})/B = -4\pi\nabla p/B^2$. The 1st-order derivatives are the perturbed components due to electromagnetic time perturbations:

$$\dot{\mathbf{R}}^{(1)} = \underbrace{\frac{c\mathbf{b}}{B_\parallel^*} \times \nabla\left(\langle\delta\varphi\rangle_\theta - \frac{p_z}{m}\langle\delta A_\parallel\rangle_\theta\right)}_{=\mathbf{v}_{\mathbf{E}\times\mathbf{B}}} - \frac{q_s}{cm}\langle\delta A_\parallel\rangle_\theta\frac{\mathbf{B}^*}{B_\parallel^*} \, , \tag{2.26}$$

$$\dot{p_z}^{(1)} = -q\frac{\mathbf{B}^*}{B_\parallel^*} \cdot \nabla\left(\langle\delta\varphi\rangle_\theta - \frac{p_z}{cm}\langle\delta A_\parallel\rangle_\theta\right) = -q\frac{m}{p_z}(\mathbf{v}_\parallel + \mathbf{v}_{curv\mathbf{B}} + \mathbf{v}_{\nabla p}) \cdot \nabla\left(\langle\delta\varphi\rangle_\theta - \frac{p_z}{cm}\langle\delta A_\parallel\rangle_\theta\right), \tag{2.27}$$

where $\mathbf{v}_{\mathbf{E}\times\mathbf{B}}$ is the drift due to electric fields, by definition it must be a 1st order perturbation. In the electrostatic case, all terms $\langle\delta A_\parallel\rangle_\theta$ are put to 0. In such a condition, for $\dot{\mathbf{R}}^{(1)}$, we see that the only 1st order term to survive is the ExB drift. In linear simulations, when solving equations 2.22 and 2.23 the characteristic will just retain the 0th order components (2.24 and 2.25) neglecting the terms proportional to ϵ_δ (2.26 and 2.27). In the non-linear case, the non-linear wave-particle interactions ($\dot{\mathbf{R}}^{(1)}$

and $\dot{p}_z^{(1)}$) are retained in the characteristic equations allowing the particles to follow the perturbed trajectories and redistribute in phase-space.

If we consider the derivative of the Action (eq. 2.15) with respect to the electromagnetic perturbations $\delta\varphi$ and $\delta A_\parallel$, we obtain the field equations. Taking as test function the electrostatic perturbation $\delta\varphi$ we get the gyrokinetic Poisson equation:

$$\frac{\partial \mathcal{A}}{\partial \delta\varphi}\delta\varphi = 0 \implies -\epsilon_\delta \sum_s m_s \int \nabla \cdot \left(\frac{c^2 F_{0,s}}{B^2}\nabla\delta\varphi\right) dW = \sum_s q_s \int \langle F_s\rangle_\theta^* dW \ . \quad (2.28)$$

Considering instead the derivative with respect to the parallel magnetic potential perturbation we yield the gyrokinetic Ampére equation:

$$\frac{\partial \mathcal{A}}{\partial \delta A_\parallel}\delta A_\parallel = 0 \implies \epsilon_\delta \sum_s \int \left[\frac{\mu_s}{B}\nabla^2\delta A_\parallel + \frac{q_s^2}{c^2 m_s}\delta A_\parallel\right] F_{0,s} dW + \epsilon_\delta\nabla^2 A_\parallel =$$
$$= \sum_s \frac{q_s}{m_s}\int p_z \langle F_s\rangle_\theta^* dW \ . \quad (2.29)$$

In equations 2.28 and 2.29, the operator $\langle...\rangle_\theta^*$ is the adjoint of the gyroaveraging operator. Fianally, it is possible to rewrite the gyrokinetic Vlasov equation to reproduce the evolution of distribution functions in the gyrokinetic approximation:

$$\frac{dF_s}{dt} = \frac{\partial F_s}{\partial t} + \dot{\mathbf{R}} \cdot \frac{\partial F_s}{\partial \mathbf{R}} + \dot{p}_z \frac{\partial F_s}{\partial p_z} = 0 \ . \quad (2.30)$$

Combining the characteristic equations 2.17 to 2.20, the field equations 2.28 and 2.29 with the gyrokinetic Vlasov equation 2.30, using appropriate boundary conditions, it is possible to reproduce the approximated kinetic behavior of a certain plasma geometry.

The theory hereby outlined is at the base of many girokinetic codes, as XGC, GENE and ORB5 [69, 82, 83]. In particular we will present in section 3.1 the principles of the PIC code ORB5. Furthermore, we will make use of this theory to derive the gyrokinetic dispersion relations of GAMs (section 2.3.2). Before moving to the physical theory of such instabilites we give an overview of the EPs dynamics in fusion devices.

2.2 Energetic Particles dynamics

Energetic Particles (EPs) are an ion species with suprathermal velocities $v_{th,EP} \ll v_{th,i}$, where $v_{th,EP}$ is the thermal velocity of EPs and $v_{th,i}$ is the thermal velocity of bulk ions. Given the high energies, EP species is very weakly collisional and therefore can exist

far from thermal equilibrium, as anisotropic non-Maxwellian distribution functions F_0. In a tokamak, such particles are generated by the heating systems (section 1.4), in particular ICRH and NBI. In this thesis we limit our studies to the EPs generated by NBI systems, therefore from now on any reference to EPs will be to NBI-generated EPs. NBI systems are characterized by the *injection energy*, this is the velocity at which neutral particles are injected in the plasma by this heating device. Typical tokamak NBI injection energies are below $100 \ keV$, in ASDEX-Upgrade (AUG) NBIs have energies ranging from $\sim 60 \ keV$ to $\sim 93 \ keV$ [84]. As it will be defined in section 2.4, such velocities are sub-alfvénic (namely they have a velocity lower than Alfvén velocity). Nevertheless, NBI systems in JT-60 SA and ITER are planned to have very powerful neutral injection systems, respectively at $500 \ keV$ [85] and $1 \ MeV$ [86], reaching super-alfvénic velocities. Plasma species, in general, can resonate with waves propagating through the plasma, provided they have thermal velocities comparable to the phase velocity of the wave. In particular, EPs are able to interact with AWs and GAMs. The details of such interaction mechanism are explained in the following section.

2.2.1 Inverse Landau Damping and wave-particle resonant interaction

Waves propagate with a phase velocity: $v_{ph} = \omega/k$, where ω is the frequency of the mode and k is the wave number. If a particle has a characteristic velocity close to v_{ph}, then it will experience the same phase of the wave for prolonged times. Therefore, the particle will coherently feel the electromagnetic forces generated by the wave perturbation over long enough times to be accelerated or decelerated. This mechanism goes under the name of Landau damping [87].

In particular, if a particle has $v < v_{ph}$, it will be accelerated by the wave, and the energy will be transferred from to the particle from the wave, damping it. Otherwise, if $v > v_{ph}$, the particle will be decelerated and the energy ceased to the wave, exciting it. Therefore, the net exchange of power between a particle species and the wave is dependant on the velocity-space gradients of the distribution function F_0. As we can see in fig. 2.2, if the phase velocity is located at a point in phase space of the F_0 which has a negative gradient $\partial F_0/\partial v|_{v_{ph,1}} < 0$ (dashed green line in fig. 2.2), there will be more particles accelerating than those decelerating. Hence, globally, the species will gain energy from the wave, damping it. On the other hand, if $\partial F_0/\partial v|_{v_{ph,2}} > 0$ (dashed red line in fig. 2.2), more particles at higher energies are slowed down than those accelerated, the mode acquires energy from the particles.
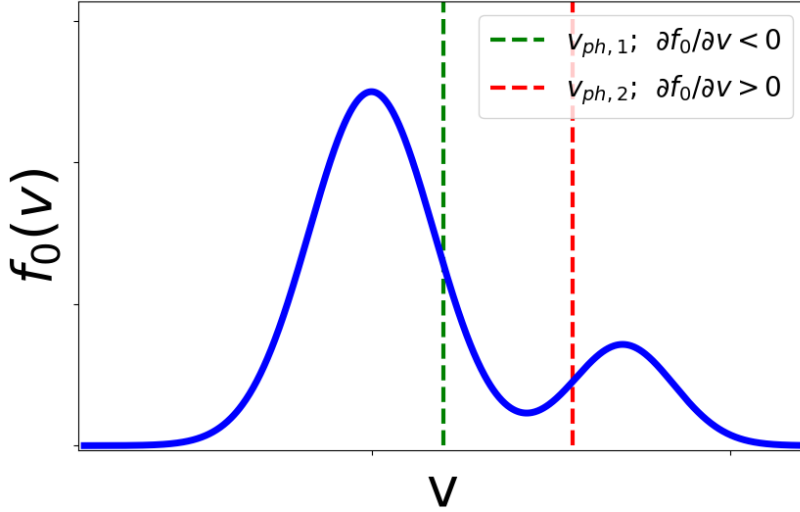
Figure 2.2: Visualization of two different waves propagating at different phase velocities v_{ph} and interacting with the F_0 at points with different velocity space gradients.

The wave with $v_{ph,1}$, **green** line, interacts with the particles around this velocity. Because $\partial F_0/\partial v|_{v_{ph,1}} < 0$, more particles at lower energy $v < v_{ph,1}$ are displaced toward higher energies than those with $v > v_{ph,1}$ slowed down. The particle species gains energy and the wave is damped.

The viceversa happens for the wave with $v_{ph,2}$, **red** line. Given $\partial F_0/\partial v|_{v_{ph,1}} > 0$, there are more particles at higher energy $v > v_{ph,2}$, which are slowed down, than those with $v < v_{ph,2}$. Consequently, in this case, the net exchange of energy is negative for the particles and positive for the mode.

We showed conceptually that the linear growth rate of these EP driven instabilities is proportional to the phase space gradient of the distribution function: $\gamma \propto \partial F_0/\partial v$. A more detailed analysis of the linear growth rate γ_L can be found in [88]:

$$\gamma_L = \frac{\pi}{2}\omega\frac{\omega_p^2}{k^2}\left.\frac{\partial F_0}{\partial v}\right|_{v=v_{ph}} \, , \tag{2.31}$$

where ω is the real frequency of the instability and k is the wave number defined as the inverse of the wave length: $k = 2\pi/\lambda$.

Better elaborated calculations regarding the growth rates of EP instability, with a particular focus on AWs, can be found in [47]. It is important to notice that the exciting mechanisms of these modes can involve radial pressure gradients as well. Specifically, the pressure gradient ∇p is crucial in inducing particle drifts perpendicular to the magnetic field. The frequency of such drifts can be defined as in [47]:

$$\omega_D = \frac{n}{q}\frac{\partial \varepsilon}{\partial \psi} \ , \tag{2.32}$$

where q is the safety factor at a given radial position, ε is the kinetic energy of the particle, ψ the radial coordinate as defined in eq. 1.32 and n is the toroidal mode number of the instability. The poloidal mode number is represented by m, so that the Fourier characteristic of a mode can be determined by the set (m, n):

$$\delta G = \hat{G}e^{i(n\phi - m\chi + ...)} \ . \tag{2.33}$$

After some calculations a new evaluation for the growth rate follows as shown in reference [47]:

$$\gamma_L \propto \omega\frac{\partial F_0}{\partial \varepsilon} - \frac{n}{q}\frac{\partial F_0}{\partial \psi} \ . \tag{2.34}$$

equation 2.34 not only shows that modes are excited by positive gradients in velocity space, as in equation 2.31, but also, in the case of AWs ($n \neq 0$), by negative radial gradients of density.

As mentioned above, EP populations have thermal velocities comparable to the phase velocity of two important instabilities, the GAM and the AW. Therefore, the EPs can resonate with these modes through the mechanism explained above. In conclusion, anisotropic distribution functions can drive EGAMs unstable (see sec. 2.3 for details). Whereas, AWs can be destabilized both by anisotrpy in phase space and density profile gradients (sec. 2.4). In the following sections, we are going to provide the reader with some general information about GAMs and AWs, their analytical derivation from MHD and gyrokinetic approaches and their dispersion relations.

2.3 Geodesic Acoustic Mode Theory

The geodesic acoustic mode (GAM) is a finite-frequency, toroidally-symmetric ($n = 0$) acoustic perturbation of density and electric potential in tokamaks [44]. There is also another family of toroidal instabilities called Zonal Flows (ZFs) [89]. ZFs can be only driven unstable non-linearly [90] interacting with AWs [57, 58] and turbulence [53, 66, 91], in particular with the so-called ion temperature gradient (ITG) instability [92]. The GAMs can be considered finite-frequency, mainly electrostatic ZFs, with a $(m, n) = (0, 0)$ perturbation of electrostatic potential and $(m, n) = (1, 0)$ perturbation of density as shown in fig. 2.3.
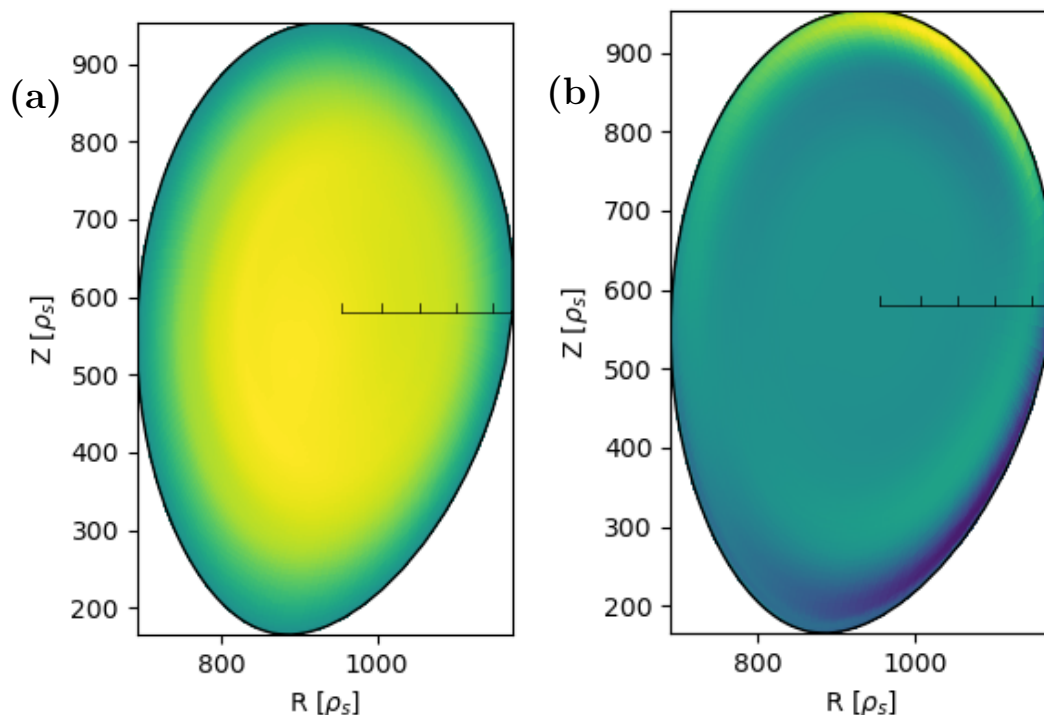
Figure 2.3: **a)** Poloidal cross section in AUG of $(m, n) = (0, 0)$ potential perturbation $(\widetilde{\delta\varphi})$ driven by a GAM. **b)** AUG poloidal cross section of a GAM $(m, n) = (1, 0)$ density perturbation (ρ_1).
The density perturbation plot has been obtained $T_{GAM}/4$ (with T_{GAM} period of the GAM) after the potential perturbation one, as prescribed by equation 2.48. The GAM shown in this plot has been taken from a simulation of those shown in Chapter 4

Unlike ZFs, they can be driven linearly by EPs. GAMs and ZFs together can be referred to as Zonal Structes (ZS). ZS are of great interest because of their capability of regulating turbulence and the corresponding transport [52, 53, 93]. Theoretical description of GAMs was first offered by Winsor et al [94] through a purely ideal MHD approach, yielding a valid estimate of the mode frequency, a similar derivation will be offered in section 2.3.1. Nevertheless, lacking kinetic considerations, like the Landau damping, evaluating the growth rate proves impossible for this model. Later, the dispersion relation of GAMs was derived using a gyrokinetic approach [95–97], enabling to the possibility of evaluating the growth rate. An example of this derivation is offered in section 2.3.2. It is found that GAMs are stabilized by collisionless Landau damping with thermal ions [98, 99]. On the other hand, EPs can excite this mode, producing the so called energetic-particle driven GAM or EGAM [48, 100–104]. EGAMs can be linearly driven by inverse Landau damping with the resonant EPs, that, unlike the bulk ions, have positive velocity gradients in F_0, see section 2.2. Consequently, EGAMs

qualify to be an effective mechanism for transferring energy from high-energy species to colder ones, as the wave-particle power exchange implies opposite contributions from EPs (which cede energy and drive the mode) and bulk ions (which absorb energy and damp the mode) [48, 105]. The inverse Landau damping provokes a phase-space redistribution of EPs from higher to lower velocities [106]. Linear drive mechanisms of EGAMs have been studied with either passing EPs [100, 102], as well as trapped particles [102], using a deeply trapped particle model [107, 108].

Experimental measurements found that the frequency of EGAMs is approximately 50% of the typical GAM frequency [103]. Analytical evaluations of the GAM dispersion relation and numerical simulations have provided supporting evidence for these observations [48, 49, 109, 110]. Nevertheless, it has also been discovered that various unstable branches exist at different frequencies [109].

The growth rate of GAM/EGAM is affected by many plasma parameters. Among them, the density of EPs (n_{EP}) plays a crucial role. Simulations and analytical derivations have demonstrated that an increase in EP concentration yields a higher growth rate of the mode. In fact, there exists a threshold value of the energetic particle fraction with respect to electron density (n_{EP}/n_e) which marks the transition from a damped mode to an excited one [49, 91, 100–102, 109, 110]. Moreover, the frequency of the GAM/EGAM typically decreases as the EP density fraction increases, due to a transition from a higher frequency GAM to a lower frequency EGAM. The safety factor profile q also affects the GAM growth rate, usually determining its radial position within the plasma [99, 111]. Finally, theoretical hints have indicated that plasma elongation impacts the growth rate [112]. Eventually, this hypothesis has been confirmed through numerical simulations [91, 111], demonstrating that both the frequency and growth rate decrease as elongation increases.

The growth rate of EGAM is greatly influenced by the velocity-space shape of the distribution function of EPs. First of all, as shown in eq. 2.31 and 2.34, anisotropies in velocity space are needed to drive the mode [47]. In particular, as explained in section 2.2, positive velocity gradients of the F_0 are necessary to drive EGAMs and result in the redistribution of a certain portion of EPs to lower energies [46]. Previous studies have used different analytical distribution functions with anisotropic properties, including bump-on-tail [46, 48, 102], slowing down with pitch dependency [100, 102, 104, 110] and single pitch Maxwellian [102]. The reader should notice that the pitch-dependent slowing down distribution function used so far was described through the parameter $\Lambda = \mu B / \varepsilon$, where μ represents the magnetic moment of the particle, ε denotes the total kinetic energy, and B represents the background magnetic field. In the present work, see section 3.3, the anisotropic slowing down F_0 are substantially different. In particular the analytical one will be defined as a function of the pitch angle and not the normalized perpendicular momentum, see section 3.3 for details avout the newly implemented

anisotropic EP distribution function. More realistic distribution functions have been implemented and tested, analytically and numerically to get closer to experimental cases [50, 59]. Indeed, it's the aim of this work to enquire into the effects of realistic distribution functions on EP dynamics.

In the next sections we show the MHD estimate of the GAM frequency and the gyrokinetic derivation of GAM dispersion relation.

2.3.1 MHD derivation of GAM frequency

Using MHD theory it's possible to derive GAM's frequency [94, 113] by linearization of the MHD equations (sec. 1.2.2). That is writing the physical quantities as a sum of an equilibrium and a perturbation contributions:

$$\rho = \rho_0 + \rho_1 \; , \tag{2.35}$$

$$\mathbf{u} = \underbrace{\mathbf{u}_0}_{0} + \mathbf{u}_1 = \mathbf{u} \; , \tag{2.36}$$

$$p = p_0 + p_1 \; , \tag{2.37}$$

where, the background velocity $\mathbf{u}_0$ has been assumed to be 0. Additionally, given the nature of the GAM, we can consider only electrostatic perturbations. Therefore, the perturbations of current and magnetic field can be considered to be 0: $\mathbf{J}_1 = 0$, $\mathbf{B}_1 = 0$. Using these considerations, if we take only the first order contributions of equations 1.23 and 1.24, we yield the following:

$$\rho_0 \frac{\partial \mathbf{u}}{\partial t} = -\nabla p_1 \; , \tag{2.38}$$

$$\frac{\partial p_1}{\partial t} = -\Gamma p_0 \nabla \cdot \mathbf{u} \; , \tag{2.39}$$

where Γ is the adiabatic index of plasma.

Furthermore, again because of the electrostatic nature of this phenomenon, the only perturbed velocity is the one arising from the perturbation of the electric field, the so called $E \times B$ drift:

$$\mathbf{u} = \mathbf{u}_E = c \frac{\mathbf{E} \times \mathbf{B}}{B^2} \; . \tag{2.40}$$

The electric field is considered to be generated by an electric "zonal" potential $\overline{\delta\varphi}$. With "zonal" quantity is meant that it is constant (or averaged) over a flux-surface. This means that it is constant along the poloidal and toroidal directions, implying that

its $(m, n) = (0, 0)$ Fourier component is different from zero. Hence, the only electric field is radially oriented:

$$\mathbf{E} = \mathbf{E}_r = -\nabla \overline{\delta\varphi} = -\frac{\partial \overline{\delta\varphi}}{\partial r} \mathbf{e}_r. \tag{2.41}$$

Plugging eq. 2.41 into 2.40, we yield that the velocity of the plasma equals $\mathbf{u} = c\mathbf{B} \times \nabla \overline{\delta\varphi}/B^2$. If we plug this last expression into equation 2.38 and we apply the operator $\nabla \cdot (\mathbf{B}/B^2 \times ...)$ we yield:

$$-\nabla \cdot \left(\frac{c\rho_0}{B^2} \frac{\partial}{\partial t} \nabla \overline{\delta\varphi} \right) = -\nabla \cdot \left(\frac{\mathbf{B}}{B^2} \times \nabla p_1 \right), \tag{2.42}$$

where we made use of the vector identity $\mathbf{B} \times (\mathbf{B} \times \nabla \overline{\delta\varphi}) = (\mathbf{B} \cdot \nabla \overline{\delta\varphi})\mathbf{B} - B^2 \nabla \overline{\delta\varphi}$, discarding the first term of the right hand side, because $\nabla \overline{\delta\varphi} \perp \mathbf{B}$. Also, we let $\mathbf{B}$ be constant with respect to the derivative operator ∂_t, consistently with the initial hypothesis of electrostatic perturbations. If we apply another time derivative to eq. 2.42, we let the derivative operator commute with the spatial differential operator using the small inverse aspect ratio approximation ($\epsilon = a/R_0 \ll 1$) and we substitute the expression for $\partial p_1/\partial t$ from eq. 2.39, we yield:

$$c \frac{\rho_0}{B^2} \frac{\partial^2}{\partial t^2} \nabla^2 \overline{\delta\varphi} = -c\Gamma p_0 \left(\nabla \cdot \left(\frac{\mathbf{B}}{B^2} \times \nabla \right) \right)^2 \overline{\delta\varphi} . \tag{2.43}$$

The operator in eq. 2.43 can be rewritten as follows:

$$\nabla \cdot \left(\frac{\mathbf{B}}{B^2} \times \nabla \right) = \left(\frac{\mathbf{b}}{B} \times 2\mathbf{k} \right) \cdot \nabla, \tag{2.44}$$

where $\mathbf{k} = \mathbf{b} \cdot \nabla \mathbf{b}$ is the magnetic field curvature. If we consider eq. 2.41, we can rewrite the differential operator $\nabla = \mathbf{e}_r \partial_r$. We can define the geodesic curvature k_s as the surviving part of the operator in eq. 2.44:

$$k_s = (\mathbf{b} \times \mathbf{k}) \cdot \mathbf{e}_r = \frac{\sin\chi}{R_0} . \tag{2.45}$$

If we plug eq. 2.45 into 2.43 and average on a magnetic flux-surface, we get the relation for the natural frequency of the GAM:

$$\left(\frac{\partial^2}{\partial t^2} + \omega_{GAM}^2 \right) \frac{\partial^2 \overline{\delta\varphi}}{\partial r^2} = 0, \tag{2.46}$$

with $\omega_{GAM} = \sqrt{2\Gamma p_0 \langle k_s^2 \rangle / \rho_0}$, and $\langle k_s^2 \rangle_\chi = 2/R_0^2$. What we got from MHD theory

is an estimate of the GAM frequency. As theorized in reference [114], the GAM frequency should be adjusted with respect to the elongation of the plasma k_δ by a factor $\sqrt{2/(1 + k_\delta^2)}$.

If we use the linearized form of the continuity equation (1.22):

$$\frac{\partial \rho_1}{\partial t} + \rho_0 \nabla \cdot \mathbf{u} = 0, \tag{2.47}$$

it is possible to study the density perturbation dynamics and compare it with the one from the potential. In fact if we plug the velocity expression (2.40), equation 2.44 and 2.45 into eq. 2.47, using the Fourier transformation for the time derivative from equation 2.46 ($\partial_t = i\omega_{GAM}$), we yield:

$$\rho_1 = -i \frac{2\rho_0 \sin \chi}{\omega_{GAM} R_0 B_0} \frac{\partial \overline{\delta\varphi}}{\partial r}. \tag{2.48}$$

From eq. 2.48 we infer that the density perturbation will be located in the same radial position of the electric field ($\partial_r \overline{\delta\varphi}$), it will be out of phase by $\pi/2$ with respect to the potential perturbation and will present a poloidal dependency, making it a $(m, n) = (1, 0)$ mode, as mentioned above (fig. 2.3).

The MHD theory used so far, was helpful to give an approximate estimate of the frequency of the mode. Nevertheless, missing the kinetic effects, such as the Landau damping (sec. 2.2), it was unable to offer an estimate of the growth rate. To do so we need a kinetic derivation of the GAM dispersion relation. In particular in the next section we will use a gyrokinetic approach starting from the concepts presented in sec. 2.1

2.3.2 Gyrokinetic description and dispersion relation

In the present section we will derive the general dispersion relation for GAMs using a background Maxwellian distribution function for the ion species i:

$$F_{0,i} = \frac{1}{(2\pi)^{\frac{3}{2}} v_{th}^3} exp \left(-\frac{v_\parallel^2 + v_\perp^2}{v_{th}^2} \right), \tag{2.49}$$

with $v_{th} = \sqrt{2T_i/m_i}$, following the steps outlined in [98, 115, 116]. In order to yield the GAM dispersion relation, we will make use of the gyrokinetic formulas (sec. 2.1) and some other hypotesis highlighted in Appendix A to yield the gyrokinetic equation (eq. 2.50):

In order to obtain the dispersion relation of GAM, we will utilize gyrokinetic formulas (section 3.1.1) and specific assumptions outlined in Appendix A, where the passages to

yield the GK equation (2.50) are shown. These considerations will allow us to derive the ion gyrokinetic equation where we will start from for our derivation:

$$(\omega_{tr}\partial_\chi - i\hat{\omega})\delta K_i = -i\hat{\omega}\frac{F_{0,i}q}{T_i}\left(\widetilde{\delta\varphi} - \frac{\omega_d}{\hat{\omega}}\overline{\delta\varphi}\right), \tag{2.50}$$

where $\omega_{tr} = v_\parallel/qR_0$ is the transit frequency of the particle, ∂_χ is the poloidal derivative, $\hat{\omega}$ is the complex frequency of the GAM, consisting both of the real frequency ω and the growth rate γ: $\hat{\omega} = \omega + i\gamma$. The perturbation of the ion distribution function was split in an adiabatic term and a non-adiabatic one [117]:

$$\delta f_i = -\underbrace{\frac{q}{T}F_{0,i}\widetilde{\delta\varphi}}_{\text{adiabatic component}} + \underbrace{\delta K_i}_{\text{non-adiabatic component}}, \tag{2.51}$$

where the adiabatic component is the part of the ion distribution function perturbation which adjust according to the potential perturbation while the non-adiabatic one is the rest of the distribution function, corresponding to something like an inertial term, for details refer to Appendix A. The perturbation of the electrostatic potential furthermore has been splitted in a flux averaged (zonal) component $\overline{\delta\varphi}$ and a non-zonal one $\widetilde{\delta\varphi}$. Finally, the magnetic drift frequency is:

$$\omega_d = \frac{k_r cm}{qBR_0}(\frac{v_\perp^2}{2} + v_\parallel^2)sin\chi . \tag{2.52}$$

The following ordering has been used to obtain eq. 2.50. The gyroaverage operator is considered to be one $\langle...\rangle_\theta = 1$. The smallness parameter $\epsilon \ll 1$ is introduced, such that $\omega_d/\hat{\omega} \sim k_r/\rho_L \sim \epsilon$. We also assign the non-zonal component of the electric potential perturbation to be much smaller than the zonal one $\widetilde{\delta\varphi}/\overline{\delta\varphi} \sim \epsilon$. A similar ordering applies to the non-adiabatic part of the distribution function: $\delta K_i/F_{0,i} \sim \epsilon$. Furthermore, electrons are hypothesized to be adiabatic, see Appendix A for details, and in eq. 2.50 only the deeply passing particle dynamics has been taken in consideration (ω_{tr} terms). We can split the non-zonal quantities in sine and cosine components: $\widetilde{\delta\varphi} = \widetilde{\delta\varphi}_c cos\chi + \widetilde{\delta\varphi}_s sin\chi$ and $\delta K_i = \delta K_{i,c} cos\chi + \delta K_{i,s} sin\chi$. Substituting this into eq. 2.50 remembering that $\omega_d = \omega_{d,s} sin\chi$ we can get the expression of the non-zonal distribution perturbation of the ions:

$$\delta K_{i,c} = \frac{iF_{0,i}q}{T_i}\frac{\hat{\omega}}{\omega_{tr}^2 - \hat{\omega}^2}\left(i\hat{\omega}\widetilde{\delta\varphi}_c + \omega_{tr}\widetilde{\delta\varphi}_s - \omega_{tr}\frac{\omega_{d,s}}{\hat{\omega}}\overline{\delta\varphi}\right), \tag{2.53}$$

$$\delta K_{i,s} = \frac{iF_{0,i}q}{T_i}\frac{\hat{\omega}}{\omega_{tr}^2 - \hat{\omega}^2}\left(i\hat{\omega}\widetilde{\delta\varphi}_s - \omega_{tr}\widetilde{\delta\varphi}_c - i\omega_{d,s}\overline{\delta\varphi}\right). \tag{2.54}$$

To find $\widetilde{\delta\varphi}$ we can utilize the simplified form of the quasi-neutrality condition, which derives from Poisson equation 2.28 (see Appendix A for details):

$$\left(1 + \frac{1}{\tau_e}\right)\widetilde{\delta\varphi} = \frac{T_i}{q}\langle\delta K_i\rangle_{\mathbf{v}}, \tag{2.55}$$

where $\langle...\rangle_{\mathbf{v}}$ is velocity space integration: $\langle...\rangle_{\mathbf{v}} = \int ...d^3v$. If we split $\widetilde{\delta\varphi}$ and δK_i into the sine and cosine contributions, from eq. 2.55 we yield:

$$\left(1 + \frac{1}{\tau_e}\right)\left(\widetilde{\delta\varphi}_c cos\chi + \widetilde{\delta\varphi}_s sin\chi\right) = \frac{T_i}{q}\left(\langle\delta K_{i,c}\rangle_{\mathbf{v}} cos\chi + \langle\delta K_{i,s}\rangle_{\mathbf{v}} sin\chi\right). \tag{2.56}$$

In order to get the dispersion relation we can find the $\langle\delta K_{i,c,s}\rangle_{\mathbf{v}}$ using the expressions from equations 2.53 and 2.54 and integrating them in phase-space. First of all, we can simplify them noticing that ω_{tr} is an odd function with respect to $v_{\parallel}$, unlike ω_d and $F_{0,i}$ (2.49) which are even by definition. This means that integrating in velocity-space all the terms proportional to ω_{tr} will cancel out. Additionally, we can simplify the integration switching to cylindrical coordinates:

$$\langle...\rangle_{\mathbf{v}} = \int_{-\infty}^{+\infty}...d^3v = 2\pi\int_{-\infty}^{+\infty}\int_{0}^{+\infty}...v_{\perp}\,dv_{\perp}\,dv_{\parallel}. \tag{2.57}$$

The first term of the right hand side of eq. 2.56 can be obtained using eq. 2.53 and 2.57 with the considerations above:

$$\langle\delta K_{i,c}\rangle_{\mathbf{v}} = -\frac{q\hat{\omega}\widetilde{\delta\varphi}}{T_i(2\pi)^{\frac{3}{2}}v_{th}^3}\left\langle\frac{\exp\left(-\frac{v_{\parallel}^2+v_{\perp}^2}{v_{th}^2}\right)}{\omega_{tr}^2 - \hat{\omega}^2}\right\rangle = -\frac{q\hat{\omega}\widetilde{\delta\varphi}}{T_i 2^{\frac{3}{2}}\sqrt{\pi}v_{th}}\int_{-\infty}^{+\infty}\frac{\exp(-v_{\parallel}^2/v_{th}^2)}{\omega_{tr}^2 - \hat{\omega}^2}dv_{\parallel}. \tag{2.58}$$

In order to solve the integral in the right hand side of eq. 2.58 we can utilize the so called plasma dispersion function (PDF) [118]:

$$Z(z) = \frac{1}{\sqrt{\pi}}\int_{-\infty}^{+\infty}\frac{\exp(-y^2)}{y - z}dy = -\sqrt{\pi}\exp(-z^2)(Erfi(z) + i), \tag{2.59}$$

where $Erfi$ is the imaginary error function. Other relevant integrals can be evaluated with the PDF:

$$\frac{1}{\sqrt{\pi}}\int_{-\infty}^{+\infty}\frac{\exp(-y^2)}{y^2 - z^2}dy = \frac{Z(z)}{z}, \tag{2.60}$$

$$\frac{1}{\sqrt{\pi}} \int_{-\infty}^{+\infty} \frac{y^2 \exp(-y^2)}{y^2 - z^2} dy = 1 + zZ(z) \,, \tag{2.61}$$

$$\frac{1}{\sqrt{\pi}} \int_{-\infty}^{+\infty} \frac{y^4 \exp(-y^2)}{y^2 - z^2} dy = \frac{1}{2} + z^2 + z^3 Z(z) \,. \tag{2.62}$$

By mean of equation 2.60 and the following normalizations: $y = v_{\parallel}/v_{th}$, $\omega_0 = v_{th}/qR_0$ and $z = \hat{\omega}/\omega_0$ we can find the explicit expression of the integral in eq. 2.58:

$$\int_{-\infty}^{+\infty} \frac{\exp(-v_{\parallel}^2/v_{th}^2)}{\omega_{tr}^2 - \hat{\omega}^2} dv_{\parallel} = \frac{v_{th}}{\omega_0^2} \int_{-\infty}^{+\infty} \frac{\exp(-y^2)}{y^2 - z^2} dy = \sqrt{\pi} \frac{v_{th}}{\omega_0^2} \frac{Z(z)}{z} \,. \tag{2.63}$$

Inserting 2.63 in 2.58 we yield:

$$\langle \delta K_{i,c} \rangle_{\mathbf{v}} = -\frac{q\widetilde{\delta\varphi}}{2^{3/2}T} zZ(z) \,. \tag{2.64}$$

With a similar derivation, using the definition of ω_d and eq. 2.61, we yield the sine component of δK_i:

$$\langle \delta K_{i,s} \rangle_{\mathbf{v}} = \frac{q}{2^{(3/2)}T} \left(-zZ(z)\widetilde{\delta\varphi}_s + \frac{k_r c m v_{th}^2}{qB\,R_0\omega_0} N(z)\overline{\delta\varphi} \right) , \tag{2.65}$$

$$N(z) = z + (1/2 + z^2)Z(z) \,. \tag{2.66}$$

Inserting equations 2.64 and 2.65 into 2.56 and solving separately for the sine and cosine components we get the following results:

$$\widetilde{\delta\varphi}_c = 0 \,, \tag{2.67}$$

$$\widetilde{\delta\varphi}_s = \frac{k_r c m\, v_{th}^2 N(z)}{2^{(3/2)}qB\,R_0\hat{\omega}D(z)}\overline{\delta\varphi} \,, \tag{2.68}$$

with $D(z) = (1 + 1/\tau_e)/z + Z(z)$. To get the dispersion relation we need higher order terms from the flux-surface averaged ($\overline{(...)}$ operator) equation and the gyro-averaged quasi-neutrality equation (the combination is the vorticity equation):

$$q\overline{\langle\langle \delta K_i \rangle_\theta\rangle_{\mathbf{v}}} = \frac{m_i c^2}{B^2} k_r^2 \overline{\delta\varphi} \,, \tag{2.69}$$

$$\hat{\omega}\overline{\langle\langle \delta K_i \rangle_\theta\rangle_{\mathbf{v}}} = -\overline{\langle\omega_d\langle \delta K_i \rangle_\theta\rangle_{\mathbf{v}}} \,. \tag{2.70}$$

Combining equations 2.69 and 2.70 we can obtain a simplified first-order form of the vorticity equation:

$$\hat{\omega}\frac{mc^2k_r^2}{qB}\overline{\delta\varphi} = -\overline{\langle\omega_d\langle\delta K_i\rangle_\theta\rangle_{\mathbf{v}}}\,. \tag{2.71}$$

Dividing the sine and cosine components, considering the definition of ω_d and performing the flux average we get:

$$\hat{\omega}\frac{mc^2k_r^2}{qB}\overline{\delta\varphi} = -\langle\omega_d\delta K_i\rangle_{\mathbf{v}}\,, \tag{2.72}$$

whose last term can be integrated in phase space using eq. 2.62. Substituting eq. 2.72 into 2.68 we get the GAM dispersion relation:

$$z + q^2\left(F(z) - \frac{N^2(z)}{D(z)}\right)\,, \tag{2.73}$$

with $F(z) = z(z^2 + 3/2) + (z^4 + z^2 + 1/2)Z(z)$. By taking a value of the safety factor q at a given radial position and establishing the plasma temperatures, it is possible to numerically solve equation 2.73, for example finding the poles of the inverse of 2.73 [49]. Alternatively, we can find explicit expressions for the GAM frequency $\omega = Re(\hat{\omega})$ and growth rate $\gamma = Im(\hat{\omega})$ from eq. 2.73, assuming moderate values of safety factor (usually $1.5 < q < 3$) and low values of wavenumber:

$$\omega = q\omega_0\sqrt{\frac{7}{4} + \tau_e}\,\sqrt{1 + \frac{2(23 + 16\tau_e + 4\tau_e^2)}{q^2(7 + 4\tau_e)^2}}\,, \tag{2.74}$$

$$\gamma = -\frac{\sqrt{\pi}}{2}q^4\omega_0\sqrt{\frac{7}{4} + \tau_e}\left[\exp(-Re(z)^2)(Re(z)^2 + 2\tau_e + 1) + \right.$$
$$\left. + \frac{q^2}{4}k_r^2\rho_i^2\exp\left(-Re(z)^2/4\right)\left(\frac{Re(z)^4}{128} + f_1Re(z)^2 + f_2\right)\right]\,, \tag{2.75}$$

where $f_1 = (1 + \tau_e)/16$ and $f_2 = 3/8 + 7\tau_e/16 + 5\tau_e^2/32$, and z as defined above. It is clear that both the frequency and the growth rate depend on the safety factor and the plasma temperatures, while γ is being strongly influenced also by the radial wave number k_r. It is interesting to notice that the growth rate γ can be only negative, because of the maxwellian distribution function, which is isotropic in parallel velocity (eq. 2.31, 2.34) [47]. It possible to derive dispersion relation for F_0 that actually drive GAMs linearly unstable like double bump-on-tails [49]. A similar derivation for the

asymmetric slowing down will be offered in sec. 4.1.

After having given an overview of the analytical theory concerning the GAM we can move on to the theory concerning the other EP driven instability treated in this thesis: the Alfvén Wave.

2.4 AW Theory

In MHD, Shear Alfvén Waves [43] are a perturbation that travels along magnetic field lines causing a perpendicular perturbation of the magnetic field $\delta\mathbf{B} \perp \mathbf{B}_0$. As it will be shown in sec. 2.4.1 they don't cause any perturbation of pressure and density, therefore they are of non-compressible nature. They can have different mode numbers $n \neq 0$ and can be excited both by velocity-space and real-space gradients [47] (eq. 2.34). Hence, unlike GAMs, also velocity-isotropic distribution functions as Maxwellians or isotropic slowing down with a radial profile can drive them unstable [73, 119]. The radial position of such modes changes with the profile of EP density [45, 120]. In fact, on-axis profiles trigger Alfvén modes (AMs) in the outer radial domain, while, off-axis peaked EP profiles excite AMs in the core [58, 62]. The eigenvalue code LIGKA [121] can evaluate the nature of the AW, by calculating the local kinetic shear Alfvén continuum (see next sections for details). LIGKA can therefore determine if the mode lies in the continuum Alfvén spectrum, if it is an energetic particle driven mode (EPM) [45, 120], or if, lying in the gaps of the Alfvén continuum due to toroidicity, it is an eigenfunction of the system, namely a toroidal Alfvén eigenmode (TAE) [119]. An example of a poloidal scalar potential perturbation caused by an AW is shown in figure 2.4, in particular in this case the perturbation is a EPM located close to the core. We will give an overview of these different natures of AWs in section 2.4.1.

2.4.1 MHD treatment of AWs

It is possible to derive the characteristic of Alfvén Waves starting from the MHD set of eqation (1.22 to 1.25 in section 1.2.2). Using a linear perturbation approach, we can split all the quantities in an equilibrium component (constant in time) and a first-order perturbation component: $\mathbf{y}(\mathbf{x},t) = \mathbf{y}_0(\mathbf{x}) + \delta\mathbf{y}(\mathbf{x},t) + o(\delta\mathbf{y})$. Assuming $\mathbf{v}_0(\mathbf{x}) = 0$, and introducing a displacement vector $\boldsymbol{\xi}(\mathbf{x},t)$ such that: $\delta\mathbf{v} = \partial\boldsymbol{\xi}/\partial t$, we can find a linearized version of the momentum (1.23), energy (1.24) and the combined Ohm and Faraday's laws (1.25), (1.19) [9]:

$$\rho_0 \frac{\partial^2 \boldsymbol{\xi}}{\partial t^2} = -\nabla \delta p + \frac{1}{4\pi}\left((\nabla \times \delta\mathbf{B}) \times \mathbf{B}_0 + (\nabla \times \mathbf{B}_0) \times \delta\mathbf{B}\right), \qquad (2.76)$$
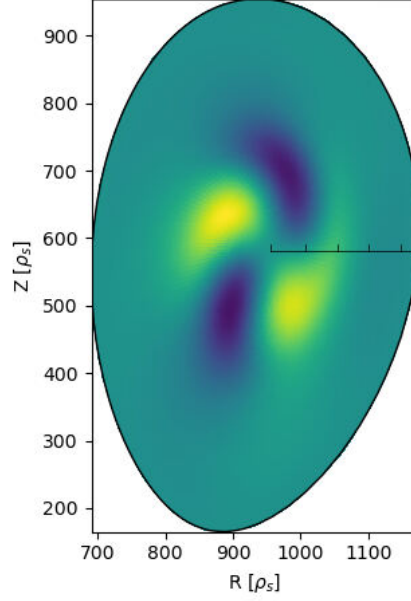
Figure 2.4: Poloidal cross section in AUG of $(m, n) = (2, 1)$ potential perturbation $(\widetilde{\delta\varphi})$ caused by a EP-driven AW (EPM). The AW is taken from one of the simulations shown in Chapter 5

$$\delta p = -\boldsymbol{\xi} \cdot \nabla p_0 - \gamma p_0 \nabla \cdot \boldsymbol{\xi} \,, \tag{2.77}$$

$$\delta \mathbf{B} = \nabla \times (\boldsymbol{\xi} \times \mathbf{B}_0) \,. \tag{2.78}$$

Substituting equations 2.77 and 2.78 into 2.76 we get the force-operator equation of linearized MHD [9]:

$$\rho_0 \frac{\partial^2 \boldsymbol{\xi}}{\partial t^2} = \mathbf{F}(\boldsymbol{\xi}) \,, \tag{2.79}$$

Assuming that the time dependency of the displacement vector can be written as follows: $\boldsymbol{\xi}(\mathbf{x}, t) = \boldsymbol{\xi}(\mathbf{x})e^{-i\omega t}$, we can recast eq. 2.79 into:

$$-\rho_0 \omega^2 \boldsymbol{\xi} = \mathbf{F}(\boldsymbol{\xi}) \,. \tag{2.80}$$

As $\mathbf{F}(...)$ is a self adjoint operator [9], the eigenvalues ω^2 of the systems are real, therefore ω can be purely real or imaginary, originating oscillating or exponentially growing modes. Secondly, another consequence of this is the fact that the modes will be orthogonal to each other. Solving the system 2.80 can be very difficult, given

the arbitrarily complex magnetic field geometry. Nevertheless, if we pick a simplified geometry with a uniform magnetic field, and assume the displacement vector to be $\boldsymbol{\xi} = \hat{\boldsymbol{\xi}} e^{-i(\omega t - \mathbf{k} \cdot \mathbf{x})}$, where $\mathbf{k}$ is the wave vector, the Fourier transform of the operator $\mathbf{F}(\boldsymbol{\xi})$ simplifies into:

$$-\rho_0 \omega^2 \boldsymbol{\xi} = \gamma p_0 (\mathbf{k} \cdot \boldsymbol{\xi}) \mathbf{k} + \frac{1}{4\pi} \left(\mathbf{k} \times [\mathbf{k} \times (\boldsymbol{\xi} \times \mathbf{B}_0)] \right) \times \mathbf{B}_0 \,. \tag{2.81}$$

Furthermore, if we hypothesize $\mathbf{B} = B_0 \hat{\mathbf{e}}_z$, and $\mathbf{k} = k_\perp \mathbf{e}_y + k_\parallel \mathbf{e}_z$ we can recast equation 2.81 in matrix form:

$$\begin{pmatrix} \omega^2 - k_\parallel v_A^2 & 0 & 0 \\ 0 & \omega^2 - k_\perp^2 v_s^2 - k^2 v_A^2 & -k_\perp k_\parallel v_s^2 \\ 0 & -k_\perp k_\parallel v_s^2 & \omega^2 - k_\parallel^2 v_s^2 \end{pmatrix} \cdot \boldsymbol{\xi} = 0 \,, \tag{2.82}$$

where $v_A = \sqrt{B_0^2 / \mu_0 \rho_0}$ is the Alfvén speed and $v_s = \sqrt{\gamma p_0 / \rho_0}$. By setting the determinate of the matrix to 0 we yield three possible solutions:

$$\omega_A^2 = k_\parallel^2 v_A^2 \,, \qquad \omega_{F,S}^2 = \frac{k^2}{2} (v_s^2 + v_A^2) \left(1 \pm \sqrt{1 - 4 \frac{k_\parallel^2}{k^2} \frac{v_s^2 v_A^2}{(v_s^2 + v_A^2)^2}} \right) \,. \tag{2.83}$$

The first solution of the system 2.82, ω_A, is the Shear Alfvén Wave (SAW), the second and third ones $\omega_{F;S}$ represent respectively the fast and slow magneto-sonic waves. The details of such magneto-sonic waves go beyond the aim of this thesis, in fact SAWs are more easily destabilized by EPs, the interested reader may refer to [9]. SAW are purely transverse waves with $\delta\mathbf{B}$ and $\boldsymbol{\xi}$ both perpendicular to $\mathbf{B}_0$. They only bend magnetic field lines and a transversal displacement of the plasma, without compression of the plasma.

Cylindrical configuration

If we adopt a cylindrical configuration, called the *straight tokamak*, a configuration similar to the screw-pinch described in Chapter 1, the magnetic field will be non-uniform: $\mathbf{B}(r) = B_\chi(r) \mathbf{e}_\chi + B_z(r) \mathbf{e}_z$. Therefore, it allows a safety factor profile to be defined, $q(r)$. Finally, assuming a periodicity both in the poloidal direction χ and the axial one z the perturbations can be written in the form:

$$\boldsymbol{\xi} = \sum_{m,n} \boldsymbol{\xi}_{m,n}(r) e^{i \left(n \frac{z}{R_0} - m\chi - \omega t \right)} \,, \quad \delta\varphi = \sum_{m,n} \delta\varphi_{m,n}(r) e^{i \left(n \frac{z}{R_0} - m\chi - \omega t \right)} \,, \tag{2.84}$$

where m, n are the poloidal and the "axial" mode numbers. If we use this representation and plug it into the *linear Vorticity equation for SAWs* [43] we get the so called Hain-Lüst equation [43, 122]:

$$\frac{1}{r^2}\frac{\partial}{\partial r}\left[r^3\left(n-\frac{m}{q}\right)^2 - r^3\frac{R_0^2}{v_A^2}\omega^2\right]\frac{\partial}{\partial r}\left(\frac{\delta\varphi_{m,n}}{r}\right) =$$
$$= \frac{m^2-1}{r^2}\left[\left(n-\frac{m}{q}\right)^2 - \frac{R_0^2}{v_A^2}\omega^2\right]\delta\varphi_{m,n} + \left(\frac{\partial}{\partial r}\frac{R_0^2}{v_A^2}\right)\omega^2\left(\frac{\delta\varphi_{m,n}}{r}\right) . \tag{2.85}$$

The solutions to this equation are [43]:

$$\omega_{m,n} = k_{\parallel,m,n}v_A(r) , \quad k_{\parallel,m,n} = \frac{1}{R_0}\left(n-\frac{m}{q(r)}\right) . \tag{2.86}$$

A visualization of eq. 2.86 is presented in figure 2.5 (left). From eq. 2.86 and fig. 2.5 we can infer that the frequency spectrum is continuous across the radial direction of the plasma cylinder, in fact, $v_A(r)$ and $q(r)$ change continuously with the radius r. As a consequence of this inhomogeneous configuration we have that a wave packet on a finite radial section will disperse. This phenomenon is called *phase mixing*, for details refer to [62, 123]. Furthermore, we notice that the spectra of different waves intersect in some points where the following condition is met:

$$k_{\parallel,m,n} = -k_{\parallel,m+1,n} \implies q(r) = \frac{2m+1}{2n} = \frac{m+1/2}{n} . \tag{2.87}$$

In the next section, we will see that in the toroidal geometry these are the points where the continuum spectrum, (fig. 2.5 left), opens in gaps where automodes of the system are, the so called toroidal alfven eigenmodes (TAEs) [119, 124]. It is interesting to notice from eq. 2.87 that the intersection points, or the TAEs, are not located on the rational surfaces $q = m/n$ but rather exactly in between them. We can imagine each mode to be sitting on a rational surface and they will superimpose constructively in the middle of the two adjacent surfaces.

Toroidal Geometry

If we adopt the toroidal geometry, with the coordinate set (r, χ, ϕ), we can set the magnetic field to be $\mathbf{B}(r, \chi) = B_\chi(r, \chi)\mathbf{e}_\chi + B_\phi(r, \chi)\mathbf{e}_\phi$. Assuming the periodicity also in the toroidal direction ϕ we can define the perturbations as:

$$\boldsymbol{\xi} = \sum_{m,n} \boldsymbol{\xi}_{m,n}(r)e^{i(n\phi - m\chi - \omega t)} \ , \quad \delta\varphi = \sum_{m,n} \delta\varphi_{m,n}(r)e^{i(n\phi - m\chi - \omega t)} \ . \tag{2.88}$$

If we use this ansatz in the SAW vorticity equation, we get a new eigenmode equation for SAWs very similar to eq. 2.85 but with the contributions from the dominant poloidal modes $(m, m \pm 1)$ [125]:

$$\frac{1}{r^2}\frac{\partial}{\partial r}\left[r^3\left(n - \frac{m}{q}\right)^2 - r^3\frac{R_0^2}{v_A^2}\omega^2\right]\frac{\partial}{\partial r}\left(\frac{\delta\varphi_{m,n}}{r}\right) =$$

$$= \frac{m^2 - 1}{r^2}\left[\left(n - \frac{m}{q}\right)^2 - \frac{R_0^2}{v_A^2}\omega^2\right]\delta\varphi_{m,n} + \left(\frac{\partial}{\partial r}\frac{R_0^2}{v_A^2}\right)\omega^2\left(\frac{\delta\varphi_{m,n}}{r}\right) + \tag{2.89}$$

$$+ \frac{\partial}{\partial r}\left[\epsilon\frac{R_0^2}{v_A^2}\omega^2\frac{\partial}{\partial r}(\delta\varphi_{m+1,n} + \delta\varphi_{m-1,n})\right] \ ,$$

where ϵ is the inverse aspect ration, as defined in sec. 1.4. The Alfvén wave contiunuum can be obtained by setting the determinant of the coefficients of the second order derivatives to zero, yielding the following frequency spectrum branches[125]:

$$\omega_{m,n}^2 = \frac{k_{\|,m,n}^2 v_A^2 + k_{\|,m+1,n}^2 v_A^2 \pm \sqrt{(k_{\|,m,n}^2 v_A^2 - k_{\|,m+1,n}^2 v_A^2)^2 + 4\epsilon^2 + \frac{r^2}{a_0^2}k_{\|,m,n}^2 v_A^2 k_{\|,m+1,n}^2 v_A^2}}{2\left(1 - \epsilon^2\frac{r^2}{a_0^2}\right)} \ , \tag{2.90}$$

where $k_{\|,m,n}$ is defined as in eq. 2.86. When the influence of toroidal effects is taken into account, the continuum spectrum of the SAW undergoes changes, as can be observed by comparing figure 2.5 on the left with figure 2.5 on the right. In figure 2.5 (left), which corresponds to the screw-pinch limit and is calculated based on equation 2.86 for modes with adjacent poloidal harmonics (m, n) and $(m + 1, n)$, the two branches of the continuum intersect where the condition 2.87 is satisfied, namely in between the resonant surfaces $q = m/n$ and $q = (m + 1)/n$.

Nevertheless, when taking into account the toroidicity, as shown in the right panel of figure 2.5, a gap appears in the continuum spectrum at the very position where the cylindrical continuum of modes m and $m + 1$ crossed (dashed, opaque lines in fig. 2.5 (right)). Within this gap, a mode called the Toroidal Alfvén Eigenmode (TAE) [43, 119, 126] can exist. Referring to the description provided in [43], the sum of the eigenfunctions making up a TAE, $\delta\hat{\varphi}_{m,n}$ and $\delta\hat{\varphi}_{m+1,n}$, is peaked at the radial position where the TAE gap is located. The two eigenfunctions propagate in opposite direction (condition 2.87) and since they are poloidally close to each other their phases can

superimpose constructively (on the low field side LFS) and let the TAE arise as a standing wave, which has weak coupling to the continuum. As a consequence, TAEs are less affected by the usual damping mechanisms associated with SAWs, like the continuum damping mentioned above.

TAEs are marginally stable but can be destabilized through resonant interaction with EPs, as discussed in section 2.2. Once excited, they interact with EPs, causing their radial transport from the plasma core of the tokamak and resulting in the loss of EPs [127]. For their capital role in the EP dynamics, and their capability to interact non-linearly with GAMs, these modes have been investigated in this thesis.
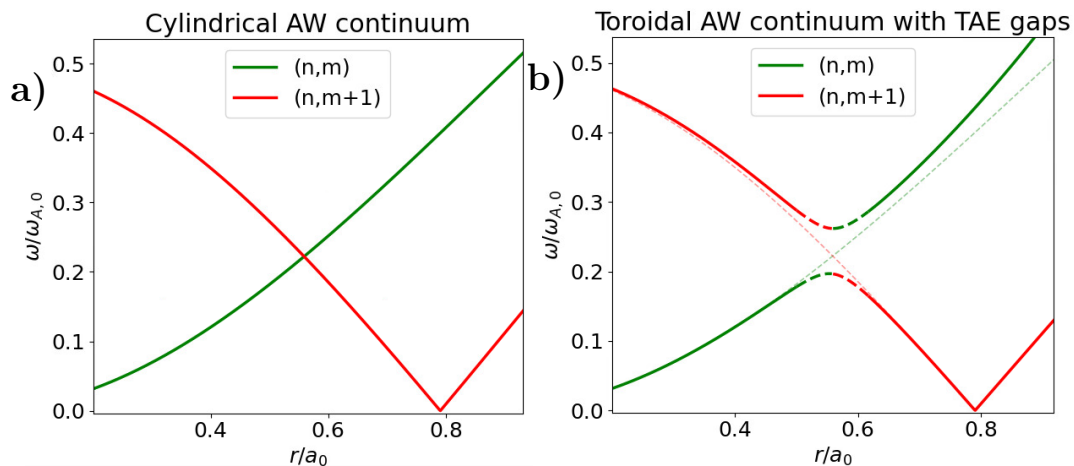
Figure 2.5: **a)** AW continuum spectrum for cylindrical geometries (equation 2.86), **b)** AW spectrum in a toroidal geometry with TAE gaps (equation 2.90). In the right image we see the original cylindrical AW continuum (dashed lines).
The plots have been obtained from equations 2.86 and 2.90 considering arbitrary values: $q = 2 + 0.8r^2$, $n = 2$, $m = 4$ and $\epsilon = 0.5$.

As a final remark about TAE, it is worth to mention that in addition to the TAEs, other gap Alfvén eigenmodes exist due to asymmetries in the equilibrium such as ellipticity and triangularity in the poloidal cross-section. These asymmetries create coupling between higher mode numbers harmonics, for example, $(m, m \pm 2)$ or $(m, m \pm 3)$. These gaps open in the continuum at higher frequencies and are referred to as the ellipticity-induced Alfvén eigenmode (EAE) [128, 129] and the triangularity-induced Alfvén eigenmodes (NAE or non-circularity-induced Alfvén eigenmode).

We have now provided the reader with the basic theory regarding the two EP driven instabilities studied in this work. We can now proceed to present the non-linear wave-wave mechanisms that exist between these two modes in the next section. As we will see in Chapter 5, such non-linear interactions are able to strongly influence the growth

rate and dynamics of both the modes. It is therefore very important to introduce the theoretical basis of such phenomenon.

2.5 AW and EGAM non-linear interactions

The aim of this section is providing the reader with an analytical introduction to the non-linear interactions between the Alfvén Waves (n=1) and the Zonal Structures (ZS) (n=0). This is a phenonemenon which has been explained theoretically [57, 58] and simulated on computer [58]. In this work we try to determine if this phenomenon is at the base of the EP dynamics observed experimentally in the NLED-AUG case [59, 70], eventually its effects will prove to be crucial for the reconstruction of experimental observation for our case, see Chapter 5. In particular, Toroidal Alfvén Eigenmodes (TAE), driven unstable by EPs in the gaps of the SAW spectrum, can interact non-linearly via wave-wave coupling with Zonal Flows (ZF) [58, 130, 131].

In order to present a summarized thoeretical background, we briefly summarize here the steps presented in Ref. [57]. As before, we consider $\delta\phi$ and $\delta A_\parallel$ as our field perturbation variables, namely the electrostatic potential and the parallel component of the vector potential. We assume the electrostatic potential to be the sum of the two different contributions (ZS and TAE): $\delta\phi = \delta\phi_Z + \delta\phi_T$. When deriving the vorticity equation it will be useful to consider that the TAE component can be divided again into the pump TAE and its complex conjugate: $\delta\phi_T = \delta\phi_0 + \delta\phi_0^*$. We write the well known non-linear vorticity equation for ZF [43, 45, 132] in order to find the ZF behaviour:

$$
\underbrace{\frac{e^2}{T_i}\langle(1-J_k^2)F_0\rangle_{\mathbf{v}}\delta\phi_Z}_{IT} - \underbrace{\sum_s\langle\frac{e_s}{\omega}J_k\omega_d\delta K\rangle_{\mathbf{v},Z}}_{CCT} =
$$

$$
= -\frac{ic\Lambda_Z}{\omega_Z B_0}\left[\underbrace{\frac{c^2 k_\perp''^2\partial_l\delta\psi_{k'}\partial_l\delta\psi_{k''}}{4\pi\omega_{k'}\omega_{k''}}}_{MX} + \underbrace{\langle e(J_k J_{k'} - J_{k''})\delta L_{k'}\delta K_{k''}\rangle_{\mathbf{v}}}_{RE}\right].
$$

(2.91)

Eq. 2.91 consists of the following terms: the inertia term (IT), the curvature coupling term (CCT), the Maxwell (MX) and Reynolds (RE) stresses. In eq. 2.91 the field line bending (FLB) term, which is normally present in the GK vorticity equation is missing because, being the case for ZF, it lacks electromagnetic contributions. In the equation $J_k = J_0(k_\perp\rho)$ is the zero-order Bessel function accounting for the finite Larmor radius effect (FLR), which comes from the exact gyroaverage operator $\langle...\rangle_\theta$. δK is the non-adiabatic response of the distribution function of the the species s, as defined in eq. 2.50. The subscripts Z and k are used in both $\delta\phi$ and δK to differentiate the

ZS contribution from the components of the various waves involved in the three-wave interaction. In fact, k refers the wave number associated with the ZS, while k' and k'' correspond to the pumping waves, namely the TAE and its complex conjugate. $\Lambda_k = \sum \mathbf{b} \cdot \mathbf{k}'' \times \mathbf{k}'$, the operator $\langle ... \rangle_\mathbf{v}$ refers to velocity-space integration, l is the coordinate along the magnetic field line. It implies that ∂_l is the derivative along the field lines and other notation is standard. According to the three wave theory [90]: $\mathbf{k} = \mathbf{k}' + \mathbf{k}''$. As MX and RE contributions to eq. 2.91 are negligible, we can find the solution for $\delta\phi_Z$ considering the expression of the non adiabatic EP response from the non-linear gyrokinetic equation [117]:

$$(-i\omega + v_\parallel \partial_l + i\omega_d)\delta K = -i\frac{e_s}{m}QF_0 J_k \delta L_k - \frac{c}{B_0}\Lambda_k J_{k'}\delta L_{k'}\delta K_{k''}, \qquad (2.92)$$

where $QF_0 = (\omega\partial_\varepsilon - \omega_*)F_0$, with $\varepsilon = v^2/2$ and $\omega_* F_0 = \mathbf{k} \cdot \mathbf{b} \times \nabla F_0/\Omega$, $\delta L = \delta\phi - v_\parallel \delta A_\parallel/c$. Considering the non-linear EP response in terms of the drift orbit center coordinates $\delta K_Z^{NL} = e^{i\lambda_{dZ}}\delta H_{dZ}^{NL}$, with $\lambda_{dZ} = \hat{\lambda}_{dZ}cos\chi = k_Z \hat{\rho}_d cos\chi$. Using this notation, it is possible to recast eq. 2.92 in a new form. We can divide it into the surface averaged and the poloidally varying components. Being $\omega_d = \omega_{tr}\partial_\chi \lambda_{dZ}$, the surface averaged component of δK_Z^{NL} equals 0 in the CCT component (eq. 2.91). Hence, we use the modified varying component of eq. 2.92 and plug it into the CCT component of eq. 2.91:

$$\text{CCT} = -\frac{\pi}{4}\hat{H}\frac{c}{B_0}\frac{e^2}{m}\frac{n_{0E}}{\omega_Z}\frac{k_\perp^2}{\omega_0^2}\hat{G}|\hat{A}_0|^2 \sum_m |\Phi_0|^2, \qquad (2.93)$$

where $\hat{H} = k_\theta(k_{r,0} + k_{r,0*})$ and $\hat{G} = \langle \omega_{*,E}\hat{v}_{d,E}^2(F_{0E}/n_{0E}) \times (\delta(\omega_0 - k_\parallel v_\parallel - \omega_{tr}) + \delta(\omega_0 - k_\parallel v_\parallel + \omega_{tr}))\rangle_\mathbf{v}$, in this expression the FLR effects have been neglected ($\langle ... \rangle_\theta \simeq J_k \simeq 1$). Assuming that the contribution of MX and RE stresses in eq. 2.91 are negligible, plugging eq. 2.93 into the non-linear vorticity equation 2.91 and doing some algebra we yield:

$$\partial_t \hat{\chi}_{iZ}\delta\phi_Z = i\frac{\pi}{4}\frac{k_\perp^2}{k_Z}\hat{D}\hat{G}|\hat{A}_0|^2 \sum_m |\hat{\Phi}_0|^2 e^{2\gamma_L t}, \qquad (2.94)$$

where $\hat{\chi}_{iZ} = \chi_{iZ}/(k_Z^2 \rho_i^2) \simeq 1.6q^2/\sqrt{a/R_0}$, with χ_{iZ} being the neoclassical polarization, $\hat{D} = cn_E T_i k_\theta/(B_0 n_0 m_i \rho_i^2 \omega_0^2)$. Performing a straightforward integration, it can be determined that a pumping TAE destabilizes a ZS with a growth rate twice that of the TAE.

$$\delta\phi_{ZF} \sim e^{2\gamma_L t} \implies \gamma_{ZF} = 2\gamma_L. \qquad (2.95)$$

The outcome shown in 2.95 has been observed in both hybrid simulations [131] and

gyrokinetic simulations [73]. Additionally, Vannini et al. demonstrated an interesting inverse driving mechanism, as outlined in their gyrokinetic study [58]. In this study, a strong ZS, in that case an EGAM, can non-linearly induce instability in an Alfvenic Mode (AM).

The theoretical framework adopted by Vannini et al. follows the pattern employed by Qiu [57], wherein the starting point is the non-linear vorticity equation. Since this case involves electromagnetic modes, the field line bending (FLB) term becomes significant and must be retained, unlike eq. 2.91. As before, Maxwell and Reynolds stresses can be disregarded, and the mode subscript, previously represented by k, is explicitly denoted by the mode number in the form (m, n), which characterizes the non-linearly driven AM.

$$\underbrace{\frac{c^2}{4\pi\omega_{m,n}^2}B_0\partial_t\frac{k_\perp^2}{B_0}\partial_t\delta\psi_{m,n}}_{FLB} + \underbrace{\frac{e^2}{T_i}\langle(1-J_0^2(\Gamma_{m,n})F_0\rangle_{\mathbf{v}}\delta\phi_{m,n}}_{IT} - \underbrace{\sum_s\langle\frac{e_s}{\omega}J_k\omega_d\delta K\rangle_{\mathbf{v},m,n}}_{CCT} = 0.$$

(2.96)

Following the steps presented in [58], and assuming similar hypothesis as those above, we can recast the CCT term in the following form:

$$CCT_{m,n} = -i\frac{q_{sp}}{\omega}J_0(\Gamma_{m,n})e^{i(n\phi-m\theta)}\left\langle\frac{1}{4\pi^2}\int_0^{2\pi}\int_0^{2\pi}e^{-in\phi'}e^{im\theta'}e^{i\lambda_{d,m,n}}\omega_{tr}\partial_{\theta'}\delta K_{m,n}^{NL}d\phi'd\theta'\right\rangle_{\mathbf{v}}.$$

(2.97)

To know the solution to eq. 2.97, we need to know how EPs are redistributed in phase-space by the AM. Consequently, we make use again of the non-linear gyrokinetic Vlasov equation as in eq. 2.92, where, again, the non-linear non-adiabatic response of EPs is $\delta K_{m,n}^{NL}$.

$$(\partial_t + \omega_{tr}\partial_\theta)\delta K_{d,m,n}^{NL} = -\frac{c}{B_0}e^{-i\lambda_{d,m,n}}\Lambda_{m,n}J_0(\Gamma_{k'})\delta L_{k'}\delta K_{k''}^L.$$

(2.98)

In equation 2.98 the mode coupling term $\Lambda_{m,n}$ establishes a connection between the excited mode with helicity (m, n) with the two pumping modes with helicities (m', n') and (m'', n''). This coupling imposes the following constraints: $n = n' + n''$ and $m = m' + m''$. Solving eq. 2.98, plugging the result into eq. 2.97, and subsequently inserting both into eq. 2.96, we find that the growth rate of the non-linearly driven AW can be expressed by the following relation, as shown in [58]:

$$\gamma_{AM}^{NL} = \gamma_{AM} + \gamma_{EGAM}.$$

(2.99)

So far, theory has foreseen two scenarios: firstly, when a ZS is driven non-linearly by an AW in the case where the growth rate of the ZS is less than that of the Aw ($\gamma_{ZS} < \gamma_{AW}$) [57]; and secondly, when an AW is driven by a pump EGAM in the situation where $\gamma_{ZS} > \gamma_{AM}$ [58].

It is worth to notice that the theory mentioned above was developed without assuming a specific nature of the EP distribution function, as it solely dealt with perturbations of the distribution function δf. The derivations obtained for the variational quantities remain valid regardless of the initial F_0 chosen.

One of the purposes of this thesis is to demonstrate that the theories above are also applicable to the case of experimental like distribution function [50], trying to push the simulations to more realistic scenarios [59] (see Chapter 5). Finally, this theoretical description does not involve estimates of threshold values for the EP density that make the non-linear interactions between AWs and ZSs possible. Furthermore, the agreement between theory and simulation results is jeopardized by the complex experimental equilibrium and the very steep q profile (fig. 3.2). Consequently, we do not expect a perfect quantitative match of numerical results with the predicted values of growth rates, we rather aim for a qualitative agreement (see Chapter 5).

Before moving to the results, we give a brief description of the numerical framework we used for our studies. We will give an overview of the functioning of the non-linear gyrokinetic code ORB5 (sec. 3.1). Subsequently, we will introduce the experimental equilibrium and parameters of the case adopted for our simulations (section 3.2). Finally we will introduce the reader to the two new experimental like EP distribution functions used in our simulations (sec. 3.3).

3 Numerical Model

So far, we have provided an explanation of the fundamental theoretical background necessary for understanding of the physical phenomena investigated in this work. In this chapter, we will focus on the implementation of the previously discussed theoretical models into a computational framework, whose purpose is reconstructing the observed EP physical phenomena within a specific experimental setup in ASDEX-Upgrade.

Firstly, we will provide an overview of the numerical implementation of the gyrokinetic model (discussed in section 2.1) into the particle-in-cell (PIC) code ORB5 [69] (section 3.1). Subsequently, we will present the plasma parameters and framework utilized in our ORB5 simulations. These parameters have been measured from an experimental equilibrium in ASDEX-Upgrade, known as the NLED-AUG case [70, 71]. The NLED-AUG case represents an experimental setup specifically designed to maximize the phenomena of non-linear EP dynamics (sec. 3.2).

Finally, we will introduce the two new anisotropic EP distribution functions designed to reproduce experimental distribution functions originated from NBI (sec. 3.3). These distribution functions are used throughout this thesis to enhance the numerical reconstruction of the experimental setup considered in this work.

3.1 Numerical tool: ORB5

ORB5 [69, 133, 134] is a gyrokinetic, global, non-linear, electromagnetic, particle in cell (PIC) code. It solves the Vlasov-Maxwell system of equations [75, 76, 81] sampling distribution functions with markers, using a Monte Carlo method. Electromagnetic fields are solved with a finite element method (FEM). The details about the code implementation can be found in [69, 81], here only the main aspects will be outlined. As in all the gyrokinetic codes, the ordering of the different terms plays an important role in the implementation of the gyrokinetic theory as outlined in sec. 2.1. In ORB5, the spatial perturbations caused by the stationary magnetic field geometry are considered to be an order of magnitude smaller than the time-varying perturbations of the fields. The smallness parameter associated with the geometric variations is referred to as $\epsilon_B = \rho_{th}/L_B$, where ρ_{th} represents the thermal Larmor radius and $L_B = |\nabla B/B|^{-1}$ the characteristic scale of the spatial gradient of the magnetic field.

On the other hand, the smallness parameter associated with time perturbations is denoted by $\epsilon_\delta \sim |\mathbf{B}_1|/B \sim c|\mathbf{E}_{1\perp}|/(Bv_{th}) \sim (k_\perp \rho_{th})e\delta\varphi/T_i$, where $\mathbf{E}$ denotes the electric field, v_{th} represents the thermal velocity, $k_\perp$ the perpendicular wave number, and $\delta\varphi$ represents the perturbation of the electrostatic potential. Similarly to other gyrokinetic codes, in ORB5, the relationship $\epsilon_B = \epsilon_\delta^2$ holds. As a consequence, the equations in ORB5 consider spatial perturbations up to the first order, $\mathcal{O}(\epsilon_B)$, and temporal perturbations up to the second order, $\mathcal{O}(\epsilon_\delta^2)$.

The set of spatial coordinates used in ORB5 is as follows.

- Radial coordinate: $s = \sqrt{\frac{\psi}{\psi_{edge}}}$, where ψ is the poloidal flux (eq. 1.32),

- toroidal coordinate: ϕ,

- poloidal coordinate: $\chi = \frac{1}{q(s)}\int_0^{\chi_{geo}} \frac{\mathbf{B}\cdot\nabla\phi}{\mathbf{B}\cdot\nabla\chi'_{geo}}d\chi'_{geo}$, where χ_{geo} is the poloidal geometrical angle.

ORB5 can simulate multiple particle species. Usually two (ions and electrons) or three (ions, electrons, and fast ions, as in our cases) species are involved, but many ion or fast ion species can be included too, to study different plasma scenarios (H, D, T, He and different combinations) or impurities.

The code ORB5 is designed to solve the gyrokinetic Vlasov equation, which rules the evolution of the particle distribution function in a plasma. In addition, ORB5 also solves the gyrokinetic field equations (sec. 2.1), such as the polarization equation (Poisson equation, eq. 2.28) and, in the electromagnetic model, the parallel Ampère's law (eq. 2.29).

The gyrokinetic model implemented in ORB5 describes the behavior of the plasma species without considering collisions or sources. This is expressed as total derivative (d/dt) of the species distribution function F_s set to zero:

$$\frac{dF_s}{dt} = 0 \ , \tag{3.1}$$

The total distribution function is divided into a background component, referred to as $F_{0,s}$, which satisfies the unperturbed Vlasov equation, and a perturbed distribution function, denoted as δf_s. The Vlasov equation 3.1 then becomes:

$$\frac{d\delta f_s}{dt} = -\frac{dF_{0,s}}{dt} \ . \tag{3.2}$$

This formulation allows to study the dynamics of the perturbations in the plasma. In eq. 3.2 $F_{0,s}$, is usually written as a function of the kinetic energy, the adiabatic invariant μ, and the gyrocenter position $\mathbf{R}$.

The full theoretical derivation of the GK model implemented in ORB5 can be found in [79, 135]. Further details about ORB5 model and implementation are provided in the following sections.

3.1.1 ORB5 gyrokinetic model

As mentioned above, the distribution function of each species, denoted as F_s, is split into a time-independent distribution function $F_{0,s}$, also called initial or background distribution function, and a time-dependent part δf_s. Under the assumptions that $dF/dt = 0$ and $\partial F_{0,s}/\partial t = 0$, the kinetic Vlasov equation 2.30 is solved for the time-dependent δf_s by utilizing the characteristics of the particles (see sec. 2.1), we will use the so called *mixed variable* approach [136, 137]:

$$\frac{d}{dt}\delta f_s = \frac{\partial \delta f_s}{\partial t} + \dot{\mathbf{R}} \cdot \nabla \delta f_s + \dot{v}_\parallel \frac{\partial \delta f_s}{\partial v_\parallel} + \dot{\varepsilon} \frac{\partial \delta f_s}{\partial \varepsilon} = -\dot{\mathbf{R}} \cdot \nabla F_{0,s} - \dot{v}_\parallel \frac{\partial F_{0,s}}{\partial v_\parallel} - \dot{\varepsilon} \frac{\partial F_{0,s}}{\partial \varepsilon}, \quad (3.3)$$

where $\mathbf{R}$ are the gyrocenter coordinates, $\varepsilon = v_\parallel^2/2 + \mu B$ and $\mu = v_\perp^2/(2B)$. Equation 3.3 holds in the general case for non-Maxwellian distribution functions, as for the distribution functions introduced in this thesis (sec. 3.3). As shown in sec. 2.1, the gyrokinetic characteristics of the particles can be written as summation of different orders contributions: $\dot{\mathbf{R}} = \dot{\mathbf{R}}^{(0)} + \varepsilon_\delta \dot{\mathbf{R}}^{(1)}$, $\dot{v}_\parallel = \dot{v}_\parallel^{(0)} + \varepsilon_\delta \dot{v}_\parallel^{(1)}$, $\dot{\varepsilon} = \dot{\varepsilon}^{(0)} + \varepsilon_\delta \dot{\varepsilon}^{(1)}$, $\dot{\mu} = 0$. For the ORB5 equation description hereby presented, we use the formulation in $v_\parallel$ rather than the momentum p_z. The 0th-order derivatives are the so called unperturbed trajectories and are similar to those in eq. 2.24 and 2.25 :

$$\dot{\mathbf{R}}^{(0)} = v_\parallel \mathbf{b}^* + \frac{\mu}{q_s B_\parallel^*} \mathbf{b} \times \nabla B \,, \quad (3.4)$$

$$\dot{v}_\parallel^{(0)} = -\frac{\mu}{m_s} \mathbf{b}^* \cdot \nabla B \,, \quad (3.5)$$

$$\dot{\varepsilon}^{(0)} = 0 \,, \quad (3.6)$$

where $\mathbf{b}^* = \nabla \times \mathbf{A}^*/B_\parallel^*$ Whereas, the 1st-order components are the trajectory derivative perturbations due to electromagnetic time-perturbations of electrostatic potential φ and parallel electromagnetic potential $A_\parallel$. In this mixed variable approach we split the electromagnetic parallel potential in a Hamiltonian and a symplectic parts: $A_\parallel = A_\parallel^h + A_\parallel^s$. The equations we get for the first order contributions are similar to equations 2.26, 2.27:

$$\dot{\mathbf{R}}^{(1)} = \frac{\mathbf{b}}{B_\parallel^*} \times \nabla \langle \phi - v_\parallel A_\parallel^s - v_\parallel A_\parallel^h \rangle - \frac{q_s}{m_s} \langle A_\parallel^h \rangle \mathbf{b}^* , \tag{3.7}$$

$$\dot{v}_\parallel^{(1)} = \frac{q_s}{m_s} \left[\mathbf{b}^* \cdot \nabla \langle \phi - v_\parallel A_\parallel^h \rangle + \frac{\partial}{\partial t} \langle A_\parallel^s \rangle \right] - \mu \frac{\mathbf{b} \times \nabla B}{B_\parallel^*} \cdot \nabla \langle A_\parallel^s \rangle , \tag{3.8}$$

$$\dot{\varepsilon}^{(1)} = v_\parallel \dot{v}_\parallel^{(1)} + \mu \nabla B \cdot \dot{\mathbf{R}}^{(1)}, \tag{3.9}$$

where

$$B_\parallel^* = \mathbf{b} \cdot (\nabla \times \mathbf{A}^*) \quad \text{and} \quad \mathbf{A}^* = \mathbf{A} + \frac{m_s c}{q_s} v_\parallel \mathbf{b} . \tag{3.10}$$

In the fully non-linear terms we also have contributions of multiplied perturbed fields (2nd order terms) and we can write the magnetic potential as follows:

$$\mathbf{A}^* = \mathbf{A} + \left(\frac{m_s c}{q_s} v_\parallel + \langle A_\parallel^s \rangle \right) \mathbf{b} . \tag{3.11}$$

In the linear limit, when solving eq. 3.3 the characteristic will just retain the 0th order components neglecting the terms proportional to ε_δ. In the non-linear case, instead, the non-linear wave-particle interactions are computed letting the particles to follow the perturbed trajectories, otherwise retaining the 1st order components. From a physical point of view, in order to evaluate the wave-particle (WP) non-linear dynamics, sometimes it is sufficient to retain the non-linearities only for the EP species. This approximation can save some computational time.

In order to have a closed system of equation we need to introduce closures for the fields quantities. To this purpose, Poisson and Ampére equations are derived from a variational formulation of the problem [76] and are coupled to the systems of equation previously shown:

$$-\nabla \cdot \left[\left(\sum_{s=i,f} \frac{q_s^2 n_s}{T_s} \rho_s^2 \right) \nabla_\perp \phi \right] = \sum_{i,e,f} q_s n_{1,s}, \quad n_{1,s} = \int \langle \delta f_s \rangle dW , \tag{3.12}$$

$$\left(\sum_{i,e,f} \frac{\beta_s}{\rho_s^2} - \nabla_\perp^2 \right) A_\parallel^h = \mu_0 \sum_{i,e,f} j_{\parallel,1,s} + \nabla_\perp^2 A_\parallel^s, \quad j_{\parallel,1,s} = q_s \int v_\parallel \langle \delta f_s \rangle dW, \tag{3.13}$$

where $n_s = \int F_{0,s} dW$, with $dW = B_\parallel^* dv_\parallel d\mu d\alpha$ being the phase space volume,

$\beta_s = 4\pi \frac{k_B n_s T_s}{B_0^2}$ is the fluid to magnetic pressure ratio, $\rho_s = \sqrt{m_s T_s}/(q_s B)$ is the gyroradius of the particles at thermal velocity.

The code ORB5 adopted a mixed variable formulation in order to solve the so called *cancellation problem* [137]. It prescribes to use both the variables p_z and $v_\parallel$ and then applying a pull-back procedure to the weights of the particles [138]. The idea is to split the parallel vector potential $A_\parallel$ into a the symplectic part $A_\parallel^s$, which is found with the ideal Ohm's law:

$$\frac{\partial}{\partial t} A_\parallel^s + \mathbf{b} \cdot \nabla \phi = 0 \ , \tag{3.14}$$

and a Hamiltonian part $A_\parallel^h$, solved via the mixed-variable Ampére law (eq. 3.13):

$$\left(\sum_s \frac{\beta_s}{\rho_s} - \nabla^2 \right) A_\parallel^h = \mu_0 \sum_s \delta J_\parallel + \nabla^2 A_\parallel^s \ . \tag{3.15}$$

At the end of every time step, we assign $A_\parallel^s$ to be equal to the total $A_\parallel$: $A_{\parallel,2}^s = A_{\parallel,1} = A_{\parallel,1}^s + A_{\parallel,1}^h$, and we put $A_{\parallel,2}^h = 0$. Subsequently, in the linear case, the weights are reassigned according to the pullback transformation so that the distribution F_s is not affected by this change of variables:

$$\delta f_{s,2} = \delta f_s^{sympl} = \delta f_{s,1} + \frac{q_s \langle A_{\parallel,1}^h \rangle_\theta}{m_s} \frac{\partial F_{0,s}}{\partial v_\parallel} \ . \tag{3.16}$$

Adopting this mixed variable formulation, we can take longer time steps generating the same numerical error of smaller times steps without the formulation.

3.1.2 Numerical implementation

In ORB5 all the quantities use normalized units. Normalizations are based on: the main species ion mass m_i, the ion charge q_i, the magnetic field on axis B_0, the electron temperature at a certain radius (usually $s = 0$) $T_e(s = 0)$ and the volume averaged electron density $\bar{n}_e$. In particular, lengths are normalized with respect to the ion sound Larmor radius: $\rho_s = \sqrt{m_i T_e}/q_i B_0$, and times with respect to either the cyclotron frequency $\omega_{ci} = q_i B_0/m_i c$ or the Alfvén frequency $\omega_A = v_A/R_0$.

As mentioned above, the perturabtion of the distribution function δf is discretized with markers p. To every marker a weight w_p and a volume Ω_p are assigned. The fields are discretized using a FEM with B-Splines. The modes of our interest are mainly aligned along the magnetic surfaces where $m \simeq nq(s)$. Hence, a Fourier filter is applied to retain only the modes within the interval $n \in [n_{min}, n_{max}]$ for the toroidal and $m \in [-nq(s) \pm \Delta m]$ for the poloidal mode number.

The code collects many values from the simulation, sampling various quantities, for our case mainly electromagnetic potentials are used, at regular intervals. The electromagnetic data collected is usually in Fourier components, this allows to involve less data for a complete 3D representation of the fields and to effectively represent the waves in Fourier components, highlighting the contributions from the different toroidal and poloidal mode numbers,

3.2 Numerical framework: NLED-AUG case in ASDEX-Upgrade

In this section we introduce briefly the experimental-relevant set used to run the simulations for this work with the code ORB5. The so called NLED-AUG [70] case is based on the ASDEX-Upgrade (AUG) shot #31213 at 0.84 s. This experimental setup is the base case of the *Non-Linear Energetic particle Dynamics* (NLED) project [70]. This is supposed to be an enabling case to study the non-linear EP dynamics for reactor relevant conditions.

In this experimental setup of AUG, EPs with an energy of 93 keV were introduced into the plasma through an off-axis NBI with an injection angle of 7.13° with respect to the magnetic axis. The electron temperature profile is very low and was designed to maximize the EP dynamics. In fact, as it can be notice from fig. 3.2, the $T_e(s)$ is very low in the core ($\sim 0.7 keV$ on axis) and it's peaked off-axis close to $s \sim 0.3$. The reason for this is twofold. Firstly, all the drift waves instabilities, such as the ITG, are minimized, letting the EP dynamcis become dominant. Furthermore, the ion Landau damping is minimized by the low ion temperature. Secondly, the temperature ratio is approximately $T_{EP}/T_{bulk,i} \sim 10^2$, a condition which will be present in reactors (in a burning plasma α particles are generated at $3.5 MeV$, while the background plasma temperature is around $30 keV$, the temperature ratio is similarly $\sim 10^2$). The magnetic equilibrium of the system is shown in figure 3.1 (left), the corresponding safety factor $q(s)$ profile is shown in figure 3.1 (right). The tilted NBI produces an off-axis peaked density profile of the EPs, presented in figure 3.2. As it is clear from fig. 3.1 this equilibrium configuration presents a weakly reversed shear in the plasma core, as well as a steep gradient of the q value in the outer region ($s \sim 1$). Moreover, the EP pressure is taken into account when determining the equilibrium state.

As we mentioned above, the NLED-AUG case was specifically designed to enquire into the EPs dynamics. The EP pressure too is relatively high, reaching a magnitude similar to that of thermal ions. The EP pressure ratio β_{EP} is on the same order of magnitude as the thermal ion beta $\beta_{EP} \sim \beta_{th,i}$. This very peculiar characteristic of the NLED-AUG case allows a rich variety of nonlinear instabilities driven by EPs to develop

during the experimental shots, making it exceptionally interesting for our research targets. Table 3.1 provides an overview of some of the key parameters that characterize ASDEX-Upgrade shot #31213.

Further information about the NLED-AUG case can be found in reference [71].
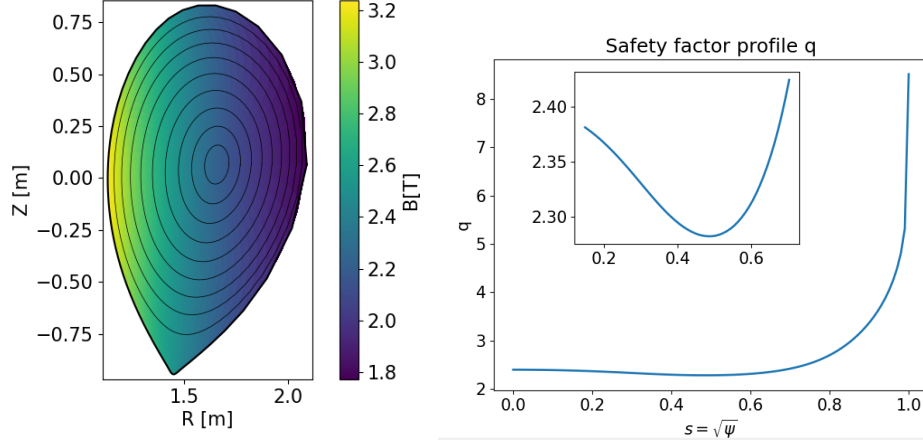
Figure 3.1: (Left): NLED-AUG case magnetic equilibrium, with flux surfaces equispaced in s; (Right): safety factor profile $q(s)$
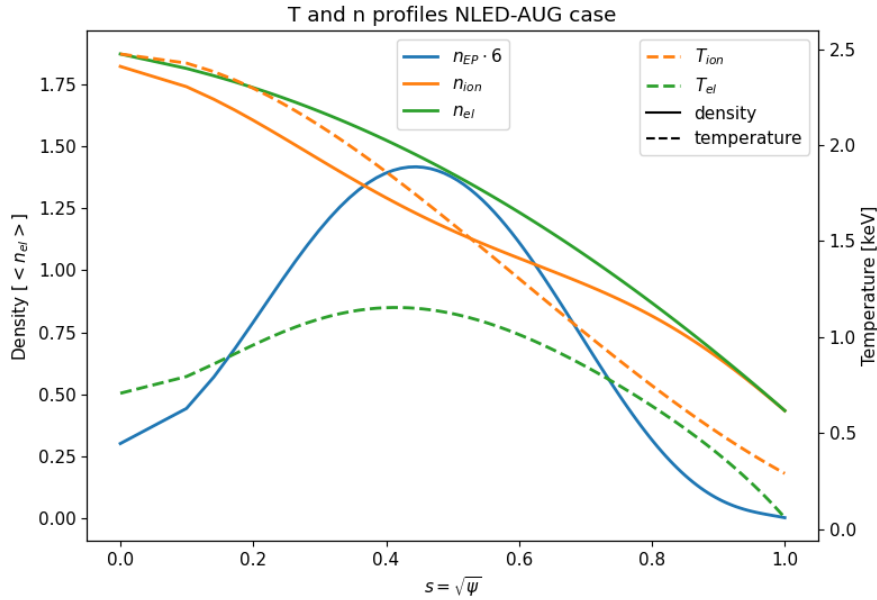
Figure 3.2: NLED-AUG case, shot #31213 in AUG, temperature and density profiles [50]

$a_0\ [m]$	$R_0\ [m]$	$B_0\ [T]$	$\Omega_{ci}\ [rad/s]$	$\omega_A\ [rad/s]$
0.482	1.666	2.202	1.054×10^8	4.98×10^6

$T_e|_{s=0}\ [keV]$	$T_i|_{s=0}\ [keV]$	$n_e|_{s=0}\ [m^{-3}]$	$n_i|_{s=0}\ [m^{-3}]$	$n_{EP}|_{s=0}\ [m^{-3}]$
0.709	2.48	1.672×10^{19}	1.6018×10^{19}	6.98×10^{17}

Table 3.1: Parameters of NLED-AUG case [50]

Magnetic instabilities from the NLED-AUG case were measured using Mirnov coils positioned at the ASDEX-Upgrade chamber wall. The collected data can be presented as frequency plots. The toroidal disposition of the probes also allows for the determination of the toroidal mode number n. As an example, figure 3.3 shows the frequency spectra observed during shot #31213 in AUG. The green lines in the plot prove the presence of Alfvénic activity, specifically an $n = 1$ EPM-TAE, within the frequency range of $100 - 200 kHz$. Additionally, EGAM ($n = 0$) activity is observed around $50 kHz$. Throughout this thesis, we will often refer to figure 3.3 as it serves as our reference case for comparing simulation results with experimental measurements gathered from the NLED-AUG case.
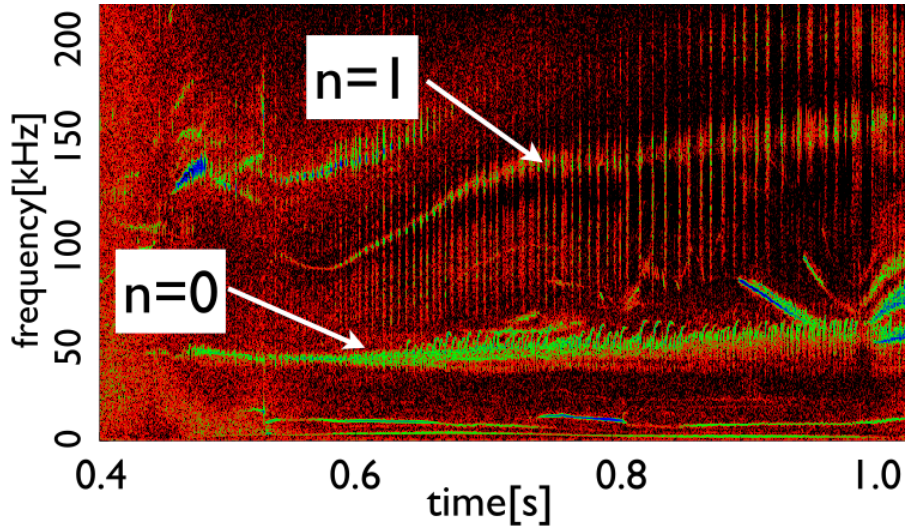
Figure 3.3: Frequency spectrogram in time of Mirnov (pick-up) coil measurements from AUG shot #31213. We can distinguish $n = 1$ AW contributions at $\sim 100 - 150 kHz$ and $n = 0$ EGAM contribution at $\sim 50 kHz$, adapted from [62]

In particular, we want to focus our attention on the EPM-TAE burst at $t = 0.84\ s$ which subsequently triggers an EGAM. This phenomenon is clearly visible in fig. 3.4, which provides a closer view of the previous spectrogram around $t = 0.84\ s$ and highlights the presence of this complex non-linear dynamics in NLED-AUG case. The

main objective in this thesis is to reproduce this phenomenon through simulations using a numerical setup that closely resembles experimental conditions. To achieve this, we utilize the experimental equilibrium, temperature and density profiles, as well as the EP distribution function from the NLED-AUG case in our simulations [50, 59] (refer to Chapters 4 and 5 for more details).
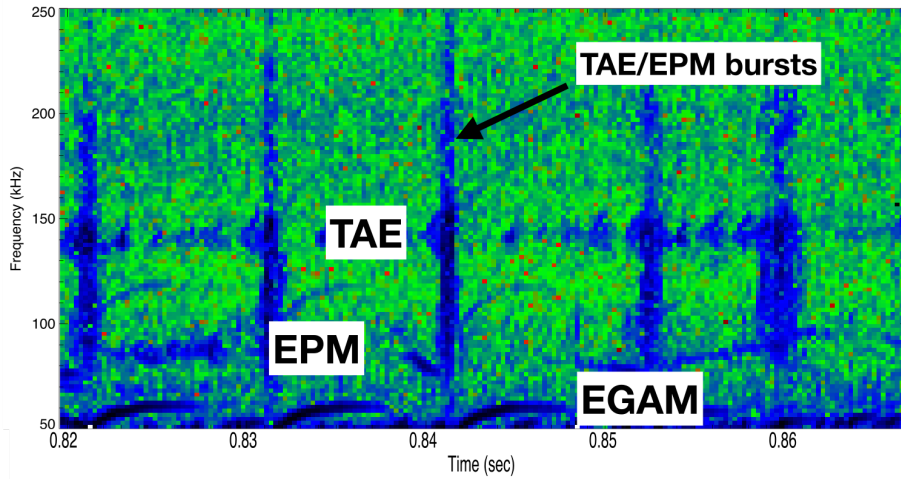
Figure 3.4: Detail of figure 3.3 close to $t \sim 0.84 \ s$. We can notice the rich non-linear dynamics emerging from the coupling of the EPM-TAE burst and the EGAM, adapted from [139]

3.3 Experimental like distribution functions

In this section we will present to the reader the two new equilibrium distribution functions which were implemented and tested in ORB5 during the work for this thesis. The results presented in Chapter 4 and 5 are produced using and modulating the parameters of these distribution functions. As explained in the previous Chapter, distribution functions have a strong impact on GAM/AW behaviour. As the EP instabilities growth rates are determined by the phase space gradients (as seen in sec. 2.2), the initial phase space distribution function has a crucial role in the dynamics of such instabilities. The investigation of EGAM/AW stability is motivated by the desire to understand the effect of different phase space shapes on the behavior of these modes. To this purpose, we have introduced two new anisotropic distribution functions, whose aim is to reproduce closely the experimental distribution function of EP produced by NBIs in the NLED-AUG case. In particular, we implemented a novel analytical distribution function that accounts for pitch-angle dependent slowing down particles. This distribution function will be presented in detail in section 3.3.1. Furthermore, we inserted as input in ORB5 a numerical experimental-like distribution function derived

from RABBIT [140], a Fokker-Plank solver for EP slowing down distributions generated by NBI, details in sec. 3.3.2. Following, in section 3.3.3 the two distribution function structures will be compared qualitatively and quantitatively. This comparison will provide valuable insights into the influence of phase space shapes on mode stability of the two distribution functions, and will be fundamental for the interpretation of the results in Chapters 4 and 5.

3.3.1 Analytical anisotropic EP distribution function

The new analytical distribution function which was implemented during this work is different from any previous distribution function studied for such cases. Being anisotrpic, it is fundamentally distinct from the isotropic distributions: Maxwellian or isotropic slowing down. In fact, as mentioned in section 2.2 we need anisotropy in parallel velocity to trigger an EGAM linearly. It is also different from the other anisotrpic distribution functions like the double-bump-on-tail F_0. Which is a well known distribution function used to study the linear stability of EGAMs [48]. In order to have an anisotropic pitch-dependent slowing down F_0 we have to design a function of energy and parallel velocity, both are normalized with respect to the sound speed $v_s = \sqrt{T_e/m_i}$. The equilibrium distribution function, as presented in eq. 3.2, was written as follows:

$$
F_{0,s}(v, \xi, \psi) = \underbrace{n_{val}(\psi)}_{\text{radial density}} \underbrace{\frac{2\sqrt{\frac{2}{\pi}}}{\sigma_\xi[\text{erf}(\frac{\xi_0+1}{\sqrt{2}\sigma_\xi}) - \text{erf}(\frac{\xi_0-1}{\sqrt{2}\sigma_\xi})]}}_{\text{gaussian normalization term}} \underbrace{\exp\left(-\frac{(\xi-\xi_0)^2}{2\sigma_\xi^2}\right)}_{\text{gaussian term}} \times
$$

$$
\times \underbrace{\frac{3\,\Theta(v_\alpha - v)}{4\pi(v_c^3(\psi) + v^3)}}_{\text{slowing down term}} \quad \underbrace{\frac{1}{ln\left(1 + (\frac{v_\alpha}{v_c(\psi)})^3\right)}}_{\text{slowing down normalization term}} \quad .
$$

(3.17)

The analytical Anisotropic Slowing Down (ASD) distribution function (eq. 3.17) was obtained as a product of a slowing down in energy, characterized by the absolute value of velocity $v = \sqrt{2\varepsilon}$ (4th and 5th right hand side (RHS) terms of eq. 3.17), and a Gaussian in the normalized parallel velocity $\xi = v_\parallel/|v|$ (ξ can range only from -1 to 1) centered in ξ_0 (2nd and 3rd RHS terms in eq. 3.17), characterized by a width σ_ξ. The ASD distribution function depends radially on the magnetic flux coordinate ψ, normalized with respect to its value at the separatrix, through the normalized species radial density profile $n(\psi)$. In eq. 3.17, $\Theta(v_\alpha - v)$ is the Heaviside function. This

function equals 1 for values of $v < v_\alpha$ and 0 elsewhere, where v_α is the injection velocity of the NBI, and $v_c(\psi)$ is the critical velocity of plasma, which is calculated from bulk plasma parameters (especially T_e) hence depending again on the radial coordinate ψ. The function erf is the error function: $\mathrm{erf}(z) = 2/\sqrt{\pi} \int_0^z e^{-t^2} dt$.

This distribution function was constructed on purpose to create a versatile tool to study the physics of anisotropy through a simple analytical parametrization of anisotropy itself through the two parameters ξ_0 and σ_ξ. The parameters range between values that have a precise physical meaning. The preferred pitch ξ_0 range between:

- -1/+1: the preferred pitch of the EPs ξ_0 is completely antiparallel/parallel to the magnetic field. Therefore, particles will be mainly deeply passing.

- 0: the EPs are injected mainly perpendicular to the magnetic axis. The generated particles are mainly trapped. This configuration is unphysical for NBI injection devices. In fact, injection angles are usually closely parallel to the magnetic field lines because the NBI is oriented tangentially with respect to the magnetic axis in order to maximize the path of the beam through the plasma and hence the particle deposition and consequently minimize the damage to the wall opposite to the NBI.

As in ASDEX-Upgrade the NBI beams are oriented in the direction opposite to the magnetic field lines, in our simulations we let ξ_0 range between -1 and 0 (Chap. 4).

The other parameter σ_ξ is the standard deviation of the Gaussian in normalized parallel velocity and is representative of the width of the scattering of particles around the preferred pitch ξ_0. This value can range between:

- $\longrightarrow 0$: all the particles tend to be focused closely around the main pitch ξ_0. The lower limit 0 (single pitch) is unphysical to be reached by NBI generated F_0. For our simulations the lower limit is set to be 0.1 (Chap. 4, 5). Such value already creates a strong anisotropy in $v_\parallel$ and is well below the value of σ_ξ measured from the experimental-like F_0 generated from RABBIT (~ 0.2, see sec. 3.3.3 for details).

- $\longrightarrow \infty$: the particles tend to distribute isotropically with respect to $v_\parallel$, the anisotropy of F_0 is lost as we get closer to this limit. For simplicity, in our simulations we used $\sigma_\xi = 0.6$ as upper limit for this value. As it will be shown in Chap. 4, this value is already very close to an isotropic slowing down case.

An example of this parametrization of the anisotropy of the distribution function through ξ_0 and σ_ξ can be observed in fig. 3.5. In this case the values were $\xi_0 = -0.6$ and $\sigma_\xi = 0.4$. ORB5 distribution functions are represented in the phase space used in fig.

3.5. The two coordinates used in the figure are a parallel velocity $v_\parallel$, normalized with respect to the sound velocity $v_s = \sqrt{T_e/m_i}$, and a normalized energy $\varepsilon = v_\parallel^2/2 + \mu B$. In this representation $(v_\parallel, \varepsilon)$, all the points lying under the $\mu = 0 \implies \varepsilon = v_\parallel^2/2$ parabola are non physical, as such points have $\mu < 0$. Hence, the code will not consider them when sampling the F_0 with markers. Furthermore, it is interesting to notice the intrinsic difference between $v_\parallel$ and ξ. The first parameter is normalized with respect to a constant value v_s, while the latter is normalized with respect to the modulus of velocity $|\mathbf{v}|$ which varies with energy ε. This causes the characteristic curvature in the analytical ASD F_0 and implies a reduction in the width scattering of F_0, measured in $v_\parallel$ units, as we move to lower values of energy (or equivalently $|v|$).

In particular, in the picture, the pitch is highlighted by a red line. Because of the units of the axes $(v_\parallel, \varepsilon)$, a constant normalized parallel velocity ξ appears as a parabola. The scattering of the particles σ_ξ, as aforementioned, represents the width of this distribution in parallel velocity, in the picture in orange.
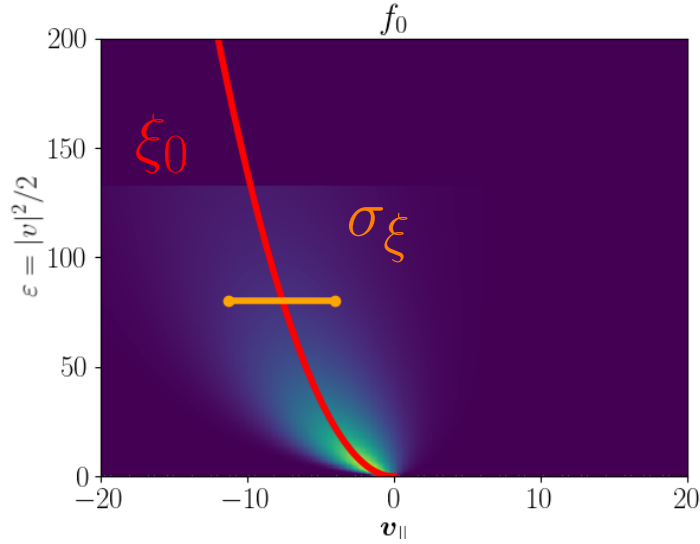
Figure 3.5: Analytical asymmetric slowing down (ASD) with pitch angle dependency defined by equation 3.17 ($\xi_0 = -0.6, \sigma_\xi = 0.4$), ξ_0 and σ_ξ are qualitatively represented on top of the F_0 plot

Part of the results presented in this thesis is a study of the physical effects of the anisotropy through this analytical F_0 parametrized by the values ξ_0 and σ_ξ. The other results will be obtained using the numerical experimental-like distribution function obtained from RABBIT [140] (see sec. 3.3.2). Therefore, using the ASD F_0 it is possible to demonstrate how simple parameters affect the growth rates of the modes (Chap. 4).

This will also provide additional confidence when it comes to studying simulations with more realistic distribution functions, as those obtained from RABBIT. Finally, this ASD distribution function is not a solution of the equilibrium Vlasov equation, because of the explicit dependence on the parallel velocity (eq. 3.17). This distribution function represents a further step in the direction of the experimental-like distribution functions with respect to the isotropic slowing down presented in [73] or the double-bump-on-tail from [58]. Meanwhile, it is also the step before moving to more realistic, numerical distribution functions (see next section).

3.3.2 RABBIT distribution function

In this section we will present the most realistic distribution function available to ORB5 so far. It is a fully numerical distribution function obtained from the Fokker-Planck solver RABBIT (for details refer to [42, 140, 141]). RABBIT solves the collisions for these EP beams in tokamak configurations and gives as output a numerical 3D matrix. The dimension are radius, energy and Legendre coeffiecients (for the $v_\parallel$ dependency). A numerical tool converts the Legendre coefficients into samples of the F_0 in parallel velocity and scales all the units accordingly to ORB5 normalizations. The matrix obtained from this numerical tool is then fed as input into ORB5, which has been equipped to read numerical distribution functions for the species. RABBIT has been run to reproduce the EP distribution functions generated by NBIs in NLED-AUG case, namely discharges #31213-6 in AUG [70] at $t = 0.84$ s. The four different distribution functions are shown in figure 3.6. As the ASD, they show a strong anisotropy in $v_\parallel$, and this shape is what ispired us to build an analytical distribution function defined in section 3.3.1. In section 3.3.3, we will attempt a comparison between the two distribution functions, even though, as it will be clear expecially from the results (Chap. 4 and 5), a direct parallelism between the two is not possible. Furthermore, the RABBIT distribution functions consist of three different injection velocities E, $E/2$, $E/3$, as typical for positive NBI injectors, as these are the different ionization states that the hydrogen molecule can have. The reader should notice that in fig. 3.6 the injection velocities appear to be different from shot to shot. This is due to the normalization with respect to the electron temperature which varies from shot to shot. On an absolute scale all the injection velocities are equal. These distribution functions were generated in the four different AUG shots using three different NBIs angles with respect to the axis of the machine. Shot 31213 has the most off-axis angle (7.13°), shot 31214 the most on-axis (6.07°) and 31215-6 a mid-range angle (6.65°). Shot 31216 has an additional on-axis NBI beam blip needed to measure the temperature profile. RABBIT was setup to calculate the steady state solution of F_0, in order to guarantee well defined gradients (as explained in [141]) which is an important feature for ORB5.
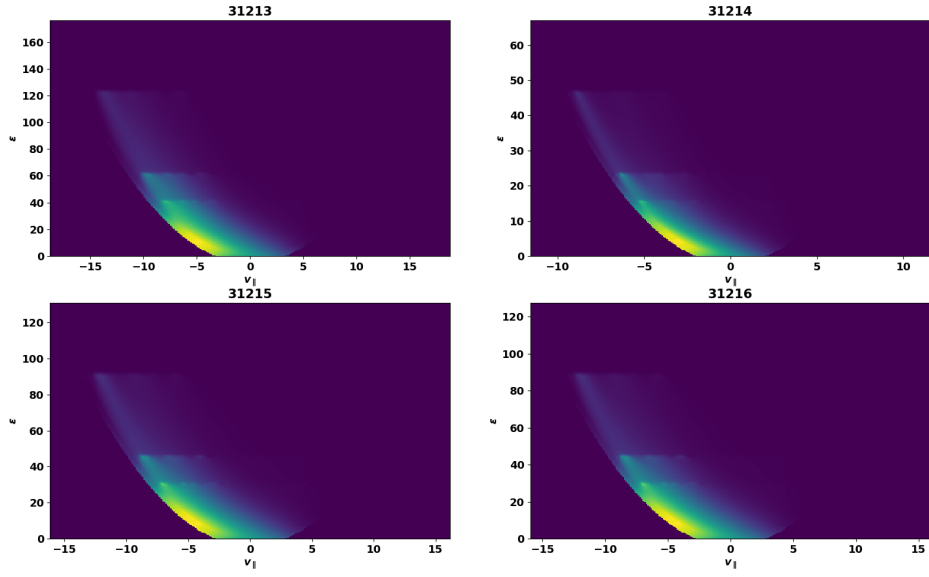
Figure 3.6: Realistic distribution functions generated from RABBIT, NLED-AUG case shots # 31213-6

To achieve experimental relevant conditions in our simulations, we provided ORB5 with the above described distribution functions and experimental radial profiles of density and temperature from the four various shot configurations. Figure 3.7 shows the EP density profiles derived from the four shots. These profiles were used for the normalization of the numerical 3D F_0 at each radial position.
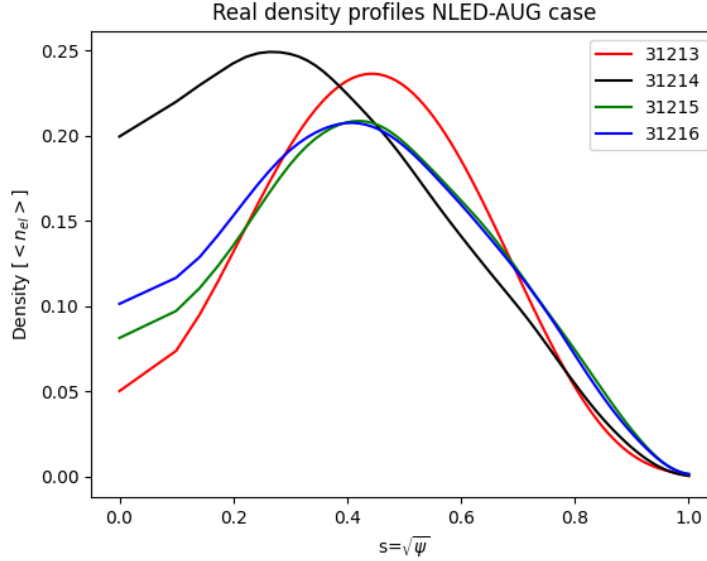
Figure 3.7: Realistic EP density profiles, NLED-AUG case shots # 31213-6, as function of $s = \sqrt{\psi}$ with ψ magnetic flux coordinate

After having presented the main feature of both the new anisotropic distribution functions, we can move on to present a more detailed comparison between the two distribution functions.

3.3.3 Comparison of analytical ASD and RABBIT F_0

The newly implemented ASD distribution function with pitch angle dependence is able to analytically model the distribution of particles along a preferred pitch angle. This characteristic is also present in the realistic RABBIT F_0 (refer to sec. 3.3.1 and 3.3.2).

The term "realistic" here has relative meaning. In fact, when comparing the RABBIT F_0 with the model described in equation 3.17, where ξ_0 and σ_ξ are arbitrary parameters, the former is evidently more realistic. This is because the RABBIT F_0 has been purposefully computed to faithfully reproduce the slowing down distribution functions resulting from NBI injections in tokamak plasmas. On the other hand, the analytical ASD distribution function serves as a relatively simple analytical reconstruction, which aims (though not necessarily achieves) to imitate the phase-space shape exhibited by the RABBIT F_0. Nevertheless, it accomplishes this goal using only a few parameters, allowing for the study of their effects by running simulations with varying values for ξ_0 and σ_ξ, as it will be shown in Chapters 4 and 5.

We developed a mathematical tool to attempt to measure the similarity between the ASD and the RABBIT F_0. This tool consider the RABBIT distribution function

at a given radius ψ_1, so that $F_0(v_\parallel, \varepsilon)|_{\psi_1}$. This plane is then cut at different values of energy ε so that we get 1D plots of the $F_0(v_\parallel)|_{\psi_1, \varepsilon_1}$ as the blue line in figure 3.8 (right) shows. Then two fits are performed. The Gaussian fit (dashed black line), which provides the values ξ_0 and σ_ξ, was obtained by taking a least squares approach to fit a Gaussian (Caruana algorithm). The Gaussian "moments" (dashed purple lines) were calculated by taking the ξ_0 as the mean, and σ_ξ as the square root of the variance of the RABBIT slice. By performing these fits for all the energy levels of the $F_0(v_\parallel, \varepsilon)$ we can plot the values of ξ_0 and σ_ξ from these fits as shown in figure 3.8 (left). If we take the RABBIT distribution function from shot #31213 at a radius $\rho_{tor} = 0.525$ the fits give the following values of ξ_0 and σ_ξ:
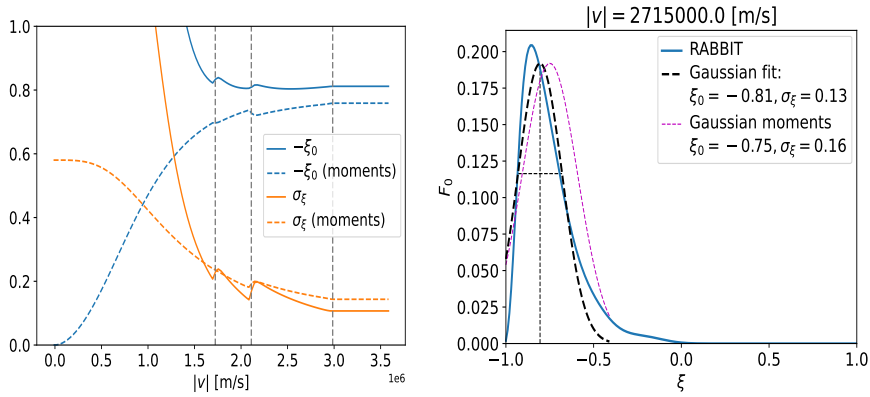
Figure 3.8: Left: trends of ξ_0 and σ_ξ in energy ($|v|$) fitting RABBIT F_0 slices with a Gaussian defined by ξ_0 and σ_ξ; right: comparison of a RABBIT F_0 slice with a Gaussian defined with certain parameters ξ_0 and σ_ξ

The vertical lines in fig. 3.8 (left) correspond to the injection energies $E_0 = 93\ keV$, $E_0/2$, and $E_0/3$. Figure 3.8 (right) shows an example of the Gaussian fits applied in figure 3.8 (left) at an energy $E_0/2 < E < E_0$. As we can see from fig. 3.8 (left) we get good constant values for ξ_0 and σ_ξ at higher energies. Above $E_0/3$ we get an average pitch $\langle \xi_0 \rangle$ around -0.8, and a σ_ξ around 0.2, these being functions of energy and radius. At lower energies instead the fitted values diverge and it becomes very hard to find an agreement between the RABBIT F_0 (the fitted data) and the ASD F_0 (the fit Gaussian). At low energies, this is mainly due to the fact that the RABBIT F_0 shows an isotropization phenomenon (due to the collisions) as we move to lower values of ε (see fig. 3.6). In fact, as we can see in the left plot of figure 3.8, the orange lines (representative of σ_ξ) both diverge to higher values (as mentioned in sec. 3.3.1, high values of σ_ξ correspond to high isotropy in the F_0). Since in the ASD F_0 the pitch is normalized with respect to the absolute value of velocity, this isotropization effect is

neglected and the distribution pitch and deviation is constant in energy by definition.

Furthermore, we note that even at a single large energy (as plotted in fig. 3.8, right), the pitch is not exactly represented by the Gaussian, but nonetheless a Gaussian can be considered a proxy for the more realistic RABBIT distribution function. As said above, from the figure it is clear that the anisotropic slowing down with pitch dependency is not always the best match with realistic distribution functions. Nevertheless, the simple analytical parametrisation with just two parameters is a very useful and versatile tool that offers a reasonable approximation to the key features of realistic distribution functions.

The evaluation of the distribution function in RABBIT involves some approximations, the most significant one being that it only calculates the flux-surface average of the distribution function, neglecting the poloidal dependency. Moreover, orbit effects during slowing down are neglected, this approximation is less severe because the first orbit (after ionization) is considered.

In contrast, other Monte Carlo-based models such as NUBEAM [142, 143] and ASCOT [144] do not have these limitations and can provide a distribution function depending on the horizontal, vertical spatial coordinates and the energy and pitch velocity-space coordinates (R, z, ε, ξ). However, these models are subject to Monte Carlo noise, which makes it difficult to calculate gradients and complicates their integration into codes like ORB5. Therefore, they are not straightforward choices as a source for ORB5.

A comparison between RABBIT and NUBEAM has been performed, the relevant moments of the distribution function (e.g. density, current, heating, pressure, neutron emission) from the two codes were compared. Good agreement was found [140, 141], and we note that the current is a good proxy for comparing the average pitch of two distribution functions. However, a direct comparison of the distribution functions has not been performed.

In conclusion, many differences have been found existing between the analytical ASD and the RABBIT distribution functions, so we refrain from inviting direct comparison of the results obtained with them. Nevertheless, we will look at the results from the simulations with the two different F_0 and we will highlight the similarities and differences. The details of this will be shown clearly in the result chapters (4, 5).

Using the analytical distribution function defined above (equation 3.17), we can also proceed to derive a stability analysis from the dispersion relation of EGAMs (see section 4.1), before showing numerical results obtained from ORB5 simulations. The effects of the new ASD distribution function are analyzed as a function of the two parameters which characterize the new slowing down distribution of energetic particles, ξ_0 and σ_ξ, along with the stability studies with the realistic RABBIT F_0.

4 Linear electrostatic simulations of EGAM

In this chapter we will present both analytical and numerical studies on the linear excitation of EGAMs. As outlined in sec. 2.3, EGAM is a very important EP instability which is being widely investigated for its importance in redistribution, confinement, transport of EPs in tokamak plasmas [106] and for its capability of regulate turbulence [52, 93]. The findings presented in this chapter, along with the other results in this thesis, are important steps toward the prediction of non-linear EP dynamics in experimentally relevant scenarios of burning plasmas [68].

To refine our numerical tool, the gyrokinetic code ORB5, we have tested it with experimentally relevant cases such as the NLED-AUG case (sec. 3.2). This test involved using both analytical and numerical anisotropic EP distribution functions. As a first step in this test we have studied the linear stability of EGAMs by varying the parameters of the ASD F_0 and also exploring different RABBIT F_0 distributions specific to the NLED-AUG case [50]. In both cases, we ran scans of simulations while varying the EP concentration, as this parameter is relevant for the stability of EGAMs [100, 101]. As it will be explained in more detail in sec. 4.2, we ran sets of linear electrostatic simulations with ORB5 [69], because the EGAM is a purely electrostatic mode (sec. 2.3).

The NLED-AUG case has already been studied using isotropic and anisotropic EP distribution functions. Namely, it was tested using isotropic slowing-down F_0 [73] and anisotrpic double bump-on-tail F_0 [48, 58, 145]. In the former case, isotropic EP distribution functions are unable to drive the GAM unstable and in the latter case they are very excited because of the shape of the double bump-on-tail which is purposefully designed to trigger the EGAM. In both cases, we are very far from the experimental condition which presents an anisotrpic distribution functions which originates from NBI deposition into the plasma. To this purpose, in this work the new distribution functions presented in sec. 3.3 are implemented in the gyrokinetic code ORB5 [69] to try to reproduce numerically the most faithful reconstruction of the experiment.

The content of this chapter is as follows. We will first present theoretical analysis of the newly implemented analytical distribution function, following the dispersion relation studies carried out in [100, 102, 109] (section 4.1). After that, we will briefly

introduce the ORB5 setup for the linear electrostatic simulations shown in this chapter (sec. 4.2). Subsequently, the numerical results of the simulations using analytical ASD are presented, with varying ξ_0 and σ_ξ parameters. In order to analyze which areas of the EP distribution function destabilize the EGAM we will use a diagnostic which measures the power exchange between the particles and the mode [48]. Along with the effects of the shape of the distribution function in phase space, we report and discuss the effects of other plasma parameters like ion temperature or EP concentration (section 4.3). Finally, experimental relevant distributions functions from Fokker-Planck solver code RABBIT [140] are introduce in ORB5 trying to reproduce realistic simulations of NLED-AUG case with experimental density and temperature profiles. Results are qualitatively compared with NLED-AUG case experimental data [70] and then discussed (section 4.4).

4.1 Linear dispersion relation

In this section we provide an analytical explanation to the results shown in section 4.3. We will derive the dispersion relation for EGAMs using the analytical ASD distribution function for EPs following closely the steps presented in Ref. [50, 100, 102]. As we did in section 2.3, we start from splitting the perturbed EP distribution function δf in an adiabatic and a non-adiabatic parts:

$$\delta f = q_s \frac{\partial f_0}{\partial \varepsilon} \frac{\delta \phi}{m_s} + \exp i \frac{mc}{QB^2} \mathbf{k} \times \ \mathbf{B} \cdot \mathbf{v} \delta K_g \ , \tag{4.1}$$

where the adiabatic response depends on the perturbed scalar potential $\delta \phi$ and the non-adiabatic part is δK_g. The latter satisfies the linear gyrokinetic equation [95] (already discussed in section 2.3):

$$\left(\omega - \omega_d + i \omega_{tr} \frac{\partial}{\partial \chi} \right) \delta K_g = -\frac{q_s}{m_s} \frac{\partial f_0}{\partial \varepsilon} J_0(k_\perp \rho_L) \omega \delta \phi \ . \tag{4.2}$$

In eq. 4.2 the transit frequency is $\omega_{tr} = v_\parallel / q R_0$, the particle drift frequency is $\omega_d = \overset{\wedge}{\omega}_d sin\chi = -k_r(v_\perp^2 + 2v_\parallel^2)/(2\Omega R_0)$, χ is the poloidal angle coordinate, $k_\perp$ is the perpendicular wave number, in GAMs $k_\perp \sim k_r$, $\rho_L = mcv_\perp / QB$ is the Larmor radius. $\Omega = q_s B / m_s c$ is the gyrofrequency, J_0 is the first kind Bessel function accounting for the finite Larmor radius (FLR) effects, Q is the charge of the particle and the mass-normalized energy of the particle is $\varepsilon = (v_\parallel^2 + v_\perp^2)/2$. Considering adiabatic electrons ($\omega/\omega_{tr,e} \sim \sqrt{m_e/m_i} \ll 1$), that is the electrons redistribute accordingly with the electric field perturbation having little inertia, and ignoring the FLR effects of electrons, eq. 4.2 can be trivially solved for electrons and the quasi-neutrality condition

can be written as [100]:

$$\frac{e}{T_e}(n_e + n_h)(\delta\phi - \overline{\delta\phi}) = -\frac{e}{T_e}n_c\delta\phi + \langle J_0(k_\perp\rho_{L,c})\delta K_{g,c}\rangle_v + \langle\frac{e}{m_s}\frac{\partial f_{0,h}}{\partial\varepsilon}\delta\phi + J_0(k_\perp\rho_{L,h})\delta K_{g,h}\rangle_v,$$
(4.3)

where the bar $\overline{(...)}$ is representative of a magnetic surface average and the operator $\langle...\rangle_v = \int ...dv^3$ is a velocity space integration, the subscripts c, h refer to thermal (cold) and energetic (hot) ion species, respectively.

The ordering is crucial for a correct solution of the equations with different order contributions. We define $\delta = n_h/n_c \ll 1$ as a smallness parameter and assume $T_c/T_h = O(\delta)$ which implies $\beta_h/\beta_c \sim 1$, with β being the fluid to magnetic pressure ratio. We hypothesize $\omega \sim \omega_{tr,h}$, $\omega_{d,h}/\omega \sim k_r\rho_{d,h} \sim O(\delta^{1/2})$ and $k_r\rho_{L,h} \sim O(\delta)$, with $\rho_{d,h}$ radial drift, in order to maximize the resonance drive for fast particles. For isotropic distribution functions $\rho_d \approx q\rho_{L,th}$, where $\rho_{L,th}$ is the thermal Larmor radius and q the safety factor value. For the thermal ion species: the radial drift is $k_r\rho_{d,c} \sim O(\delta)$ and the Larmor radius effects are of higher order: $k_r\rho_{L,c} \sim O(\delta^{3/2})$. We can then expand the perturbed electrostatic potential as a power series of $\delta^{1/2}$:

$$\delta\phi = \overline{\delta\phi} + \widetilde{\delta\phi}^{(1/2)} + \widetilde{\delta\phi}^{(1)} + \widetilde{\delta\phi}^{(3/2)} + ... ,$$
(4.4)

and we can do the same for the non-adiabatic response of the particles δK_g:

$$\delta K_g = \overline{\delta K_g} + \widetilde{\delta K_g}^{(1/2)} + \widetilde{\delta K_g}^{(1)} + \widetilde{\delta K_g}^{(3/2)} + ...$$
(4.5)

Using this power expansions, eq. 4.2 can be rewritten for all the orders presented in equations 4.4 and 4.5 as in eq. (3-9) of [100]. Such system can be combined with quasi-neutrality eq. 4.3 and solved order by order (up to the 3rd order) we yield the EGAM dispersion relation (see [100] for details):

$$-1 + \frac{\omega_G^2}{\omega^2} + \frac{\overline{\delta n_h}}{\overline{\delta\phi}}\frac{m\Omega}{en_ek_r^2} = 0,$$
(4.6)

where $\omega_G = \left(\sqrt{\frac{7}{4} + \frac{T_e}{T_i}}\right)\frac{v_{th}}{R_0}$ is the GAM frequency (sec. 2.3) and $v_{s,i}$ is the ion thermal velocity. In the left hand side of eq. (4.6) the last term contains the averaged EP density which is the integral in velocity space of the non-adiabatic component of the perturbation of the EP distribution function. If we write the integral in velocity space coordinates (ε, ξ) we yield:

$$\overline{\delta n_h} = \int \overline{\delta K_h^{(3)}}dv^3 = 2\pi \int_{-1}^{1}\int_{0}^{\infty}\overline{\delta K_h^{(3)}}(-\sqrt{2\varepsilon})d\varepsilon d\xi.$$
(4.7)

If we assume EPs are passing particles, we can recast the non-adiabatic EP response in the following way:

$$\overline{\delta K_h^{(3)}} = -\frac{\overset{\wedge}{\omega}_d^2 \left(\frac{e}{m_s}\frac{\partial F_0}{\partial \varepsilon}\right)}{2(\omega^2 - \omega_{tr}^2)}\overline{\delta \phi} \ . \tag{4.8}$$

Being

$$\frac{\partial F_0}{\partial \varepsilon} = \frac{\partial F_0}{\partial \varepsilon} + \frac{\partial \xi}{\partial \varepsilon}\frac{\partial F_0}{\partial \xi} \ , \tag{4.9}$$

considering the F_0 in eq. 4.9 to be the analytical ASD distribution function defined in eq. 3.17, the full derivative yields:

$$\frac{\partial F_0}{\partial \varepsilon} = F_0(\varepsilon, \xi)\left(-\delta(\varepsilon_\alpha - \varepsilon) - \frac{3}{2}\frac{\varepsilon^{\frac{1}{2}}}{\varepsilon^{3/2} + \varepsilon_c^{3/2}} + \frac{\xi}{\varepsilon}\frac{(\xi - \xi_0)}{2\sigma_\xi^2}\right) \ , \tag{4.10}$$

If we substitute expression 4.10 into 4.8 and that into 4.7, we yield the explicit integral of eq. 4.7 in terms of our coordinates as:

$$\overline{\delta n_h} = 2\pi\frac{k_r^2\overline{\delta \phi}q^2 e}{4\Omega^2 m}\int_{-1}^{1}\int_0^\infty \sqrt{2\varepsilon}\frac{(\varepsilon(1 + \xi^2))^2}{q^2 R_0^2\omega^2 - 2\varepsilon\xi^2}\frac{\partial F_0}{\partial \varepsilon}d\varepsilon d\xi =$$

$$= 2\pi A\int_{-1}^{1}\int_0^\infty \frac{\varepsilon^{\frac{5}{2}}(1 + \xi^2)^2}{q^2 R_0^2\omega^2 - 2\varepsilon\xi^2}exp\left(-\frac{(\xi - \xi_0)^2}{2\sigma_\xi^2}\right)\frac{\Theta(\varepsilon_\alpha - \varepsilon)}{\varepsilon^{3/2} + \varepsilon_c^{3/2}} \tag{4.11}$$

$$\left(-\delta(\varepsilon_\alpha - \varepsilon) - \frac{3}{2}\frac{\varepsilon^{\frac{1}{2}}}{\varepsilon^{3/2} + \varepsilon_c^{3/2}} + \frac{\xi}{\varepsilon}\frac{(\xi - \xi_0)}{2\sigma_\xi^2}\right)d\varepsilon d\xi \ ,$$

where the constant A equals:

$$A = \sqrt{2}\frac{2\sqrt{\frac{2}{\pi}}}{\sigma_\xi[erf(\frac{\xi_0+1}{\sqrt{2}\sigma_\xi}) - erf(\frac{\xi_0-1}{\sqrt{2}\sigma_\xi})]}\frac{0.75\ n_{val}}{\pi}\frac{1}{ln(1 + (\frac{\varepsilon_\alpha}{\varepsilon_c})^{3/2})}\frac{k_r^2\overline{\delta \phi}q^2 e}{4\Omega^2 m} \ . \tag{4.12}$$

Explicit integration of expression 4.11 in velocity space (ξ, ε) as in [100] is not possible due to the absence in the distribution function of a characteristic structure like the Dirac function. For the same reason, not even an explicit integration as in [109] is possible, because of the absence of the of the characteristic plasma dispersion function (eq. 2.76) in equation 4.11.

Nevertheless, it is still possible to investigate the stability of the EGAM examining the imaginary part of the complex frequency ω (namely the growth rate of the mode). In fact $\gamma = Im(\omega)$ in equation 4.6 is positive if the imaginary part of $\overline{\delta n_h}$ is positive

[102]. Without integrating explicitly eq. 4.11, we can plot the integrand function for some values of energy and parallel velocity, assuming the ω inside eq. 4.11 to equal its value computed numerically from the simulations (see section 4.3). If we vary the parameters ξ_0 between 0 and -1 and σ_ξ between 0.1 and 0.6 (see section 3.3.1), we can study the stability of the EGAM looking at the sign of the integrand function for each set of parameters (ξ_0 and σ_ξ). In particular, if we do so, we observe that the integrand sign is mostly positive at most of the energy levels as we pick values of $\xi_0 \sim 0.5$ and $\sigma_\xi \sim 0.2$. Moreover, we observe that the integrand is mostly negative or mixed (both positive and negative depending on the parallel velocity) for values of ξ_0 and σ_ξ different from those specified above. This result is consistent with the numerical results obtained from linear electrostatic simulations and shown in section 4.3.

Some figures representing the imaginary part of the integrand in eq. 4.11 computed at $\varepsilon \sim 30 keV$ and left as function of ξ are shown below in fig. 4.1. The only case showing positive values (hence positive growth rates [102]) is the case where the ASD parameters are $\xi_0 = -0.5$ and $\sigma_\xi = 0.2$ (fig. 4.1 a). The other cases ($\xi_0 = -0.5$, $\sigma_\xi = 0.6$) and ($\xi_0 = -0.1$, $\sigma_\xi = 0.2$) show a negative integrand and therefore the GAMs from the simulations using these ASD parameters will be damped (see section 4.3). As it was already discussed, in the ($\xi_0 = -0.5$, $\sigma_\xi = 0.6$) case, this negative growth rate is due to the fact that when $\sigma_\xi \longrightarrow \infty$ the ASD distribution function becomes isotropic in phase space and, hence, unable to excite n=0 modes (fig. 4.1.b). In fact, as mentioned in the sec. 2.3, n=0 modes need F_0 gradients in velocity space to be linearly triggered [47]. Meanwhile, low values of ξ_0 correspond to the case where most of the particles are perpendicular to the magnetic field. Therefore, most of them will have trapped trajectories, mitigating the effects of inverse Landau damping. In fact, the so trapped particles will be unable to resonate with the GAM hindering the excitation of the mode; this is the case of the simulation whose ASD has $\xi_0 = -0.1$, $\sigma_\xi = 0.2$ (fig. 4.1.c). We observe a specular effect for values of ξ_0 close to -1. In this case, most of the energetic particles are deeply passing and hence are too fast to resonate with the GAM. Therefore, EPs are unable to exchange energy with the mode at $v_{\parallel,res}$, hindering again the excitation of the mode. These results will be also found again numerically (as shown in section 4.3), demonstrating the validity of the theory hereby presented.
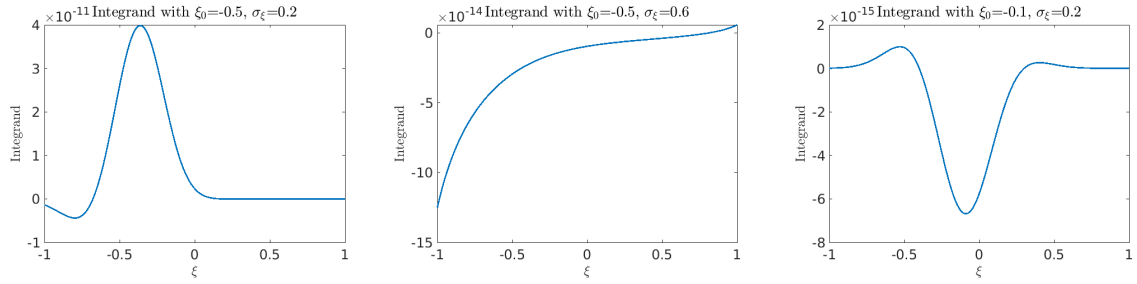
Figure 4.1: Plot of the integrand of eq. 4.11 computed at $\varepsilon \sim 30 keV$ as function of normalized parallel velocity ξ for the following ASD parameters: $\xi_0 = -0.5$, $\sigma_\xi = 0.2$ (a); $\xi_0 = -0.5$, $\sigma_\xi = 0.6$ (b); $\xi_0 = -0.1$, $\sigma_\xi = 0.2$ (c)

This analytical method can be used to theoretically validate the numerical results for extreme cases (strongly excited/damped modes), because such cases present integrands whose sign is constantly negative or positive for any value of ξ or ε. On the contrary, it's very hard to use it for an evaluation of an excitation threshold limit in terms of n_{EP}/n_e, ξ_0 or σ_ξ. In fact, for not strongly excited or damped modes, the integrand is partially negative and positive for different values of ξ and ε. In order to evaluate threshold values we have to consider the results obtained from ORB5 simulations presented in section 4.3.

The plots shown in fig. 4.1 are also useful to evaluate the main resonance velocity. Setting the growth rate (the imaginary part of the frequency ω) to 0, the denominator of the term $\frac{\varepsilon^{\frac{5}{2}}(1+\xi^2)^2}{q^2 R_0^2 \omega^2 - 2\varepsilon\xi^2}$ will go to 0 where the resonant condition for the power exchange between particles and the mode is matched. For example, for $\xi_0 = -0.5$, $\sigma_\xi = 0.2$, considering as before the real frequency from the simulation, the first resonant velocity is $v_\parallel = \sqrt{2\varepsilon\xi^2} = \sqrt{q^2 R_0^2 \omega^2} = 1.36 \cdot 10^5 \ m/s$. This value is comparable to the result from the Mode-Particle-Resonance (MPR) diagnostic [48], obtained from ORB5 simulations (see section 4.3.4 for details).

4.1.1 Simplified dispersion relation

Simplified dispersion relation can be obtained if we consider the distribution in ξ to be close to $\delta(\xi - \xi_0)$, in which case we have

$$F_0 = \frac{n_h}{2\sqrt{2}\pi \, ln(\varepsilon_c/\varepsilon_\alpha)}\delta(\xi - \xi_0)\Theta(1 - \varepsilon/\varepsilon_\alpha) \ . \tag{4.13}$$

Following the derivations envisaged in Refs. [100, 102] we yield the following dispersion relation:

$$-1 + \frac{\omega_G^2}{\omega^2} + N_b \left[\frac{3}{2}(1 - \xi_0^2 + 4\xi_0^4) \ln\left(1 - \frac{\omega_{ts}^2}{\omega^2}\right) + \left(\frac{1}{1 - \omega_{ts}^2/\omega^2} - 1\right) \right] = 0 \,. \qquad (4.14)$$

Here, $\omega_{ts} = \sqrt{2\varepsilon_\alpha}\, \xi_0 / (qR_0)$ is the EP transit frequency and $N_b = q^2 / (4\xi_0^2 \ln(\varepsilon_\alpha/\varepsilon_c))\, n_h/n_c$. The GAM frequency with Landau damping due to thermal ions ω_G can be found as a solution of the equation (from [115]):

$$\omega = -q^2 \omega_{Ti} \left(F(\omega/\omega_{Ti}) + N^2(\omega/\omega_{Ti})/D(\omega/\omega_{Ti}) \right) ,$$

with $F(x) = x(x^2 + 3/2) + (x^4 + x^2 + 1/2)Z(x)$, $N(x) = x + (1/2 + x^2)Z(x)$ and $D(x) = Z(x) + (1 + T_i/T_e)(1/x)$ [97]. Eq. 4.14 is strictly valid for deeply passing ions, i.e. $\xi_0 \sim \pm 1$. The logarithmic term in this equation, for $\omega < \omega_{ts}$ has complex values and gives a drive if the constant in-front of it is positive, which is always the case here. This shows there is no threshold in ξ_0 related to the distribution function, however some drive is necessary to overcome the finite Landau damping. The last term in eq. 4.14, along with the real part of the logarithmic term is responsible for shifting the frequency of the mode below the GAM frequency, as explained in Sec 2.3, this is the case for the EGAM. Eq. (4.14) can be easily solved numerically to obtain the modes frequency and growth rate. A rough estimate of the growth rate can be given in the limit $\omega \gg \omega_{Ti}$ and $\gamma/\omega_r \ll 1$, where the GAM frequency can be approximated with

$$\omega^2 = q^2 \omega_{Ti}^2 \left(\frac{7}{4} + \frac{T_e}{T_i} \right) - i\sqrt{\pi} q^2 \frac{\omega^5}{\omega_{Ti}^3} e^{-\omega^2/\omega_{Ti}^2} , \qquad (4.15)$$

giving a growth rate with respect to the real frequency:

$$\gamma/\omega_r \approx q^2 \left(\frac{3\pi}{16 \ln(E_b/E_c)\xi_0^2} \frac{n_h}{n_c}(1 - \xi_0^2 + 4\xi_0^4) - \frac{\sqrt{\pi}}{2} \frac{\omega_r^3}{\omega_{Ti}^3} e^{-\omega_r^2/\omega_{Ti}^2} \right) , \qquad (4.16)$$

with ω_r being the real frequency of the mode. This equation shows a threshold in the density ratio n_h/n_c, as well as dependence of the growth rate on the safety factor q [100, 102]. Given the previous considerations, the growth rate given here can be considered as the upper limit of this distribution with maximal anisotropy, namely a dependence from the pitch ξ_0 as a Dirac function ($\delta(\xi - \xi_0)$).

After these theoretical considerations about the stability of the GAM and the influence of various plasma parameters on it, using an analytical ASD EP distribution function, we will now proceed to show the numerical results. We firstly introduce to the numerical setup used for the ORB5 simulations, subsequently we present the results obtained

running the ASD F_0, and finally the results using the numerical RABBIT F_0.

4.2 Numerical setup

Before presenting the numerical results using the newly implemented anisotropic distribution functions we briefly present the numerical setup used in ORB5 for these simulations. As mentioned in section 3.2, the magnetic equilibrium and the profiles (see fig.s 3.1 and 3.2) are those from the NLED-AUG case in ASDEX-Upgrade, in particular from shot #31213 in AUG. Plasma parameters are reported in Table 3.1. The simulations included three species, deuterium ions, electrons and energetic particles. As aforementioned, the simulations were run linearly (otherwise, considering only the unperturbed trajectories for the particles of all the species, see sections 2.1 and 3.1). The fields equations were solved electrostatically, this means that only Poisson equation (eq. 3.12) was considered while the magnetic perturbation $\delta\mathbf{B}$ was set to 0 throughout the whole simulation. Being interested only in the GAM/EGAM contributions we could filter out all the modes with $n \neq 0$. The Δm was set to 5. A realistic electron to deuterium mass ratio was used: $m_e/m_D = 0.000272$. Furthermore, we adopted the approximation of adiabatic electrons since we wanted to focus on an electrostatic mode studying the kinetic effects only of energetic particles. Adiabatic electrons allow to run faster simulations, while the dynamics is not greatly affected. Considering kinetic electrons would contribute slightly to the damping of the mode but this effect is not dominant. Other numerical parameters as the time step, the (s, χ, ϕ) grid resolution and the number of markers for the different species are reported in Table 4.1.

$\Delta t[\omega_{ci}^{-1}]$	N_s	N_χ	N_ϕ	$N_{p,i}$	$N_{p,e}$	$N_{p,EP}$
10	512	256	32	10^8	10^8	10^8

Table 4.1: Numerical simulation parameters: Δt is the time step, $N_{(s,\chi,\phi)}$ are the grid resolution, N_p the total number of markers for each species

In the following section, the results from ORB5 simulations will be shown. In all these simulations the background plasma will have the same configuration and parameters, hereby described. We will change the ASD parameters ξ_0 and σ_ξ to check how the anisotropy shape affects the stability of the GAM/EGAM. We will also vary the temperature and the EP density fraction to study how these parameters affect stability (sec. 4.3.5).

4.3 Numerical results from NLED-AUG case

In this section we will describe the results of ORB5 simulations of the NLED-AUG case [70], shot #31213 in AUG, performed varying the parameters ξ_0, σ_ξ and n_{EP}. Excitation threshold values will be found numerically for these parameters.

The threshold values which will be presented in the following sections are not directly comparable to RABBIT distribution function cases. In fact, as already discussed in sec. 3.3.3, RABBIT distribution functions are not directly related to the analytical case obtained from eq. 3.17 for some value of its parameters. RABBIT distributions presents isotropization effects at lower energies, something missing in the analytical slowing down. Additionally, the analytical slowing down does not include the three injection velocities at E_0, $E_0/2$ and $E_0/3$ as in the RABBIT F_0. Nevertheless, keeping in mind these differences, we may expect some similarities in the behaviour between the simulations run with RABBIT F_0 and the ASD F_0 with $\xi_0 \sim -0.8$ and $\sigma_\xi \sim 0.2$. Furthermore, the trends of growth rate with respect of the f_0 parameters that will be found in the next sections will be observed also in the linear simulations for the RABBIT distribution functions. A comparison of the results using the ASD and the RABBIT F_0 will be presented in section 4.4.3.

In the next sections we will distinguish and analyze the effects obtained varying together or independently the two parameters ξ_0 and σ_ξ. To this purpose the following sections are organized as follows: firstly we focused our attention to the effects of the variation of each parameter independently from the other one. Hence, in section 4.3.1, growth rate trends with respect to σ_ξ are presented and, subsequently, in section 4.3.2 the trends with respect to ξ_0 are analyzed. Finally, a general scan in both the two parameters (ξ_0 and σ_ξ) is presented (section 4.3.3).

4.3.1 Stability effects of σ_ξ and threshold values

In this section we show a set of simulations as described above along a scan of values of σ_ξ ranging from 0.1 to 1. The value of ξ_0 will be kept constant at -0.5. Furthermore, an isotropic slowing-down was run as a reference case. As it was described in section 3.3.1, σ_ξ represents the scattering of the particles around the preferred pitch ξ_0. Therefore, it is representative of the anisotropy degree of the distribution function: the lower σ_ξ the more anisotropic the F_0, the higher the more isotropic. A distribution function F_0 is said to be isotropic in $v_\parallel$ when its derivative with respect to $v_\parallel$, computed at constant energy ε, is zero:

$$\left. \frac{\partial F_0}{\partial v_\parallel} \right|_{\varepsilon=const.} = 0 \ . \tag{4.17}$$

If σ_ξ approaches ∞, pitch-dependent slowing down (ASD) becomes equivalent to isotropic slowing-down distribution function. It can be shown analytically that such isotropic distribution functions in $v_\parallel$, provided they have everywhere negative gradients in energy ($\partial f / \partial \varepsilon < 0$), cannot excite EGAMs [47]. Furthermore, we expect such behavior also from the analytical observations from sections 2.3 and 4.1. The aim of this section is therefore to prove numerically that such analytical expectations are correct. Results are shown in figure 4.2. The left 4.2 plot presents the radial peak of scalar potential for the $n = 0$ modes in time, the right plot instead is a trend of growth rate γ and frequency ω as a function of σ_ξ. The left 4.2 plot shows that the ASD EP distribution functions, whose $\sigma \longrightarrow \infty$, don't trigger any EGAM, along with the isotropic slowing down (solid red line). On the other hand, small values of σ_ξ are able to drive EGAMs with higher growth rates since the gradients of F_0 are steeper. In conclusion, we can state that the growth rate quickly decreases and eventually becomes negative as σ_ξ values approach ∞. In particular, starting from values of $\sigma_\xi \sim 0.5$ we see that the results are closely comparable to those of isotropic slowing down F_0. This trend is particularly clear in fig. 4.2 (right), where the growth rates and the frequencies have been reported as function of the ASD standard deviation σ_ξ. Accordingly to the theoretical expectations (sec. 2.3), we notice that an increase in growth rate is usually matched by a drop in frequency.

The growth rates shown in fig. 4.2 (top right) were computed through a linear fit of the logarithm of the envelope of the electrostatic potential signals in time (shown in fig. 4.2 (left)). For purely linear growing modes the whole array of values in time was considered in the fit. Whereas, for stable modes just the part of the mode showing a decreasing behavior was considered, discarding the rest of the mode where the damping rate goes to zero, as the modes' amplitude gets overtaken by noise. For modes which present irregular behavior, especially at the beginning of the simulations, only the purely linearly growing parts of the modes were considered. Initial phases, where multiple frequencies may superimpose, were discarded and not included in the fit.

For this set of simulations where $\xi_0 = -0.5$ and $n_{EP}/n_e = 0.09$, we found the excitation threshold value at $\sigma_\xi \simeq 0.4$. As we can observe from fig. 4.5, this value is relevant, because the highest growth rates are found for mid-range ξ_0 values. It will be observed in section 4.3.3 that high values of ξ_0 present a non-monotonic trend with σ_ξ and therefore will have slightly higher threshold values for σ_ξ (see section 4.3.3 for details). Anyhow, as $\sigma_\xi \longrightarrow \infty$, the modes are always damped because of the isotropization of the distribution function.
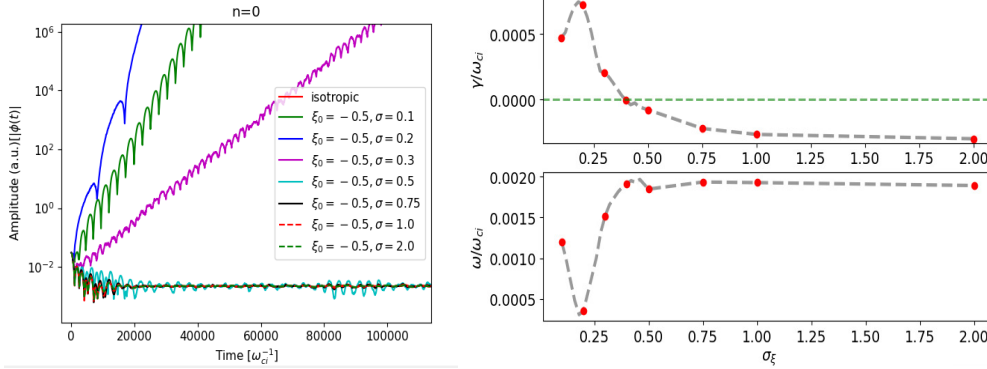
Figure 4.2: Scan with varying σ for $\xi_0 = -0.5$ in NLED-AUG case. Plot on the left shows the amplitudes of the scalar potential field in time. Plot on the right shows the growth/damping rate (top) and frequency (bottom) dependence on σ_ξ. The red dots in the plots on the right represent the correspondent γ and ω from the simulations in the left plot. The green dashed line in the top right figure represents the $\gamma = 0$ threshold

These results are crucial to prove one of the theoretical assumptions we made in sections 2.3, 3.3.1 and 4.1, namely that we can directly correlate the linear growth rate of GAM/EGAMs with the degree of anisotrpy of the EP distribution function. In this case, modeled by the parameter σ_ξ. In the next section we will analyze the dependence of the growth rate on the other parameter: ξ_0, this time keeping σ_ξ constant.

4.3.2 Stability effects of ξ_0 and threshold values

In this section, a scan has tested pitch-dependent slowing down with constant $\sigma = 0.25$ over ξ_0 ranging from 0 to -0.9. The results are plotted below. In figure 4.3, the mode amplitudes are shown in time. We observe a clear dependence of the stability on the pitch. Figure 4.4 shows the growth rate and the frequency trends with respect to the varying ξ_0.
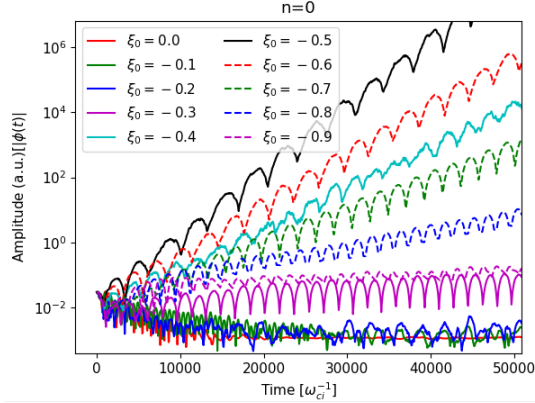
Figure 4.3: EGAM amplitudes in time from a scan of simulations using ASD F_0 with ξ_0 ranging from 0.0 to -0.9, at constant $\sigma = 0.25$ in NLED-AUG case configuration
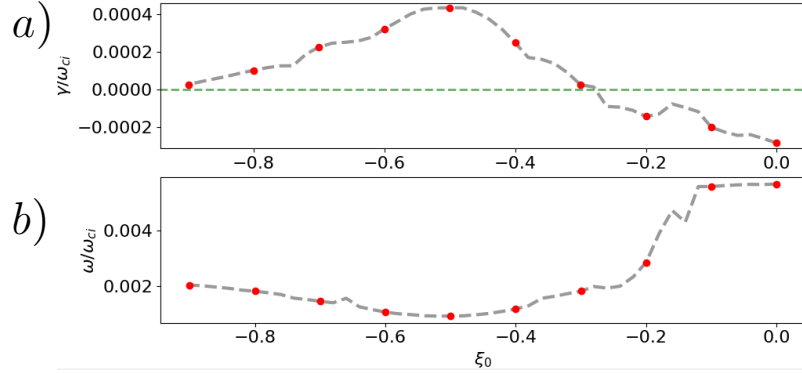
Figure 4.4: Growth rate γ **a)** and frequency ω **b)** of the simulation scan with varying ξ_0 shown in fig. 4.3. The red dots in the plots represent the correspondent γ and ω from the simulations in fig. 4.3

From both the plots in figures 4.3 and 4.4 we can observe an evident increase of growth rate for mid-range values of $\xi_0 \in (-0.3, -0.7)$, while the mode is constant or damped for values of $\xi_0 < -0.8 \vee \xi_0 > -0.2$. A theoretical model was proposed in references [100, 104] that predicted that the preferred pitch (ξ_0) must be greater than a certain value to trigger an EGAM. In reference [49], instead, a theory was advanced according to which both extremes values of ξ_0 (-1,0) have to be avoided in order to trigger an EGAM. It is important to remember that both these references obtained such conditions in a different phase space, where the normalized parallel velocity was replaced by the perpendicular energy fraction $\Lambda = \mu B / \varepsilon$. Nevertheless, the results shown in figure 4.3 and 4.4 and discussed in this section confirm the analytical predictions made so far.

In fact, the theoretical analysis proposed in section 4.1 offered an analytical explanation to such behavior. Figure 4.1, where the integrand of eq. 4.11 is plotted, predicts the behavior of these numerical simulations in function of both parameters ξ_0 and σ_ξ. Furthermore, using the considerations done in section 3.3.1, we can offer a simple physical explanation for this behavior. As we stated above, ASD distribution functions with $\xi_0 \sim 0$ correspond to EPs distributed mainly perpendicularly to the magnetic field, implying that most of them are trapped and unable to resonate with the mode leading to the damping of the GAM. Specularly, this happens with $\xi_0 \sim -1$ too, where most of the particles are deeply passing at velocities higher than the resonant velocity of the EGAM (see sec. 2.3), leading to the damping of the mode again. The only way for EPs at such energies (93 keV in AUG), to resonate with the mode is having a pitch angle that would let their parallel velocity be similar to the resonant velocity, otherwise having pitch angles close to the mid-range pitch $\xi_0 \sim -0.5$. This is actually what we observe in our simulations.

Finally, we also note that, as the growth rate increases for mid-range values of ξ_0, there is correspondent decrease of frequency (fig. 4.4,b). This results is similar to that obtained in the previous section and respond to the theoretical predictions (sec. 2.3). The frequencies shown in the plot in fig. 4.4 are Lorentzian fits of the frequency spectrum. In reality, in these simulations two modes (the GAM and the EGAM, which differ by a factor 2 in frequency) co-exist at the same time. For excited mode cases, the EGAM contribution is dominant, decreasing the Lorentzian fit of frequency values and vice versa. As already discussed, this is again in accordance with theoretical, numerical and experimental evidence [49, 103, 109].

As we will see in detail in section 4.3.3, the excitation threshold is crossed at different ξ_0 values for different σ_ξ and n_{EP}/n_e. Nevertheless, from the results reported in fig. 4.5, 4.3 and 4.4, it is clear that, whatever the other parameters are, the EGAM is excited for values of ξ_0 included in a certain interval $(\xi_{0,1}, \xi_{0,2})$, where usually $-1 \leq \xi_{0,1} \leq -0.5$ and $-0.5 \leq \xi_{0,2} \leq 0$. For our reference case, shown in figures 4.3 and 4.4 ($\sigma_\xi = 0.25$ and $n_{EP}/n_e = 0.09$), the ξ_0 threshold interval is $(\xi_{0,1}, \xi_{0,2}) \simeq (-0.9, -0.3)$ (fig. 4.4).

4.3.3 Simulation scan varying ξ_0 and σ_ξ

In this section we present the results of the EGAM growth rate of all the simulations from a scan in both ξ_0 and σ_ξ. As before, the scan has been yielded running ORB5 with the NLED-AUG case configuration (sec. 3.2). The code has been run linearly, electrostatically, considering adiabatic electrons [69, 146] in all the simulations considered. The ASD EP distribution function, used as input, was obtained implementing equation 3.17 picking ξ_0 and σ_ξ from a mesh of these two parameters with ξ_0 ranging between 0.0 and -0.9 and σ_ξ ranging between 0.1 and 0.6. The energetic particle concentration was

kept constant for all the cases, namely $n_{EP}/n_e \simeq 0.09$. The profiles used, as before, are taken experimentally from shot #31213 in AUG [50]. Figure 4.5 shows the qualitative behavior of the growth rate γ depending both on ξ_0 and σ_ξ. Clearly, as outlined in sections 4.3.1 and 4.3.2, both parameters influence γ. As expected, the growth rate is decaying for EP distributions with larger σ_ξ, while it is positive for values of ξ_0 included between -0.2 and -0.9. In figure 4.5, the magenta box is a scan with higher resolution. In fact, this area is particularly relevant because it is the part of the 2D plane (ξ_0, σ_ξ) where the stability threshold of the scan is located. We note that the highest growth rate for every σ_ξ level moves toward higher ξ_0 as σ_ξ increases (fig. 4.5). At the same time, we also note that for high values of ξ_0, as σ_ξ increases, we get a weak increase in growth rate before the isotropization effects prevail and the mode gets damped. This behavior is not observed for low values of ξ_0, for which the growth rate decreases monotonically as σ_ξ increases. It will be explained in detail in Sec 4.3.4 that for such high pitches, as σ_ξ increases, the positive gradient of F_0 in parallel velocity move in the area where the most unstable modes get most of their drive. This could be the reason that causes the excitation of the EGAMs in simulations where the ASD F_0 had high ξ_0 and $\sigma_\xi \sim 0.5$ as we can note from fig. 4.5. Anyhow as $\sigma_\xi \longrightarrow \infty$ the isotropization effects prevail and all the modes get damped no matter what ξ_0 they have.
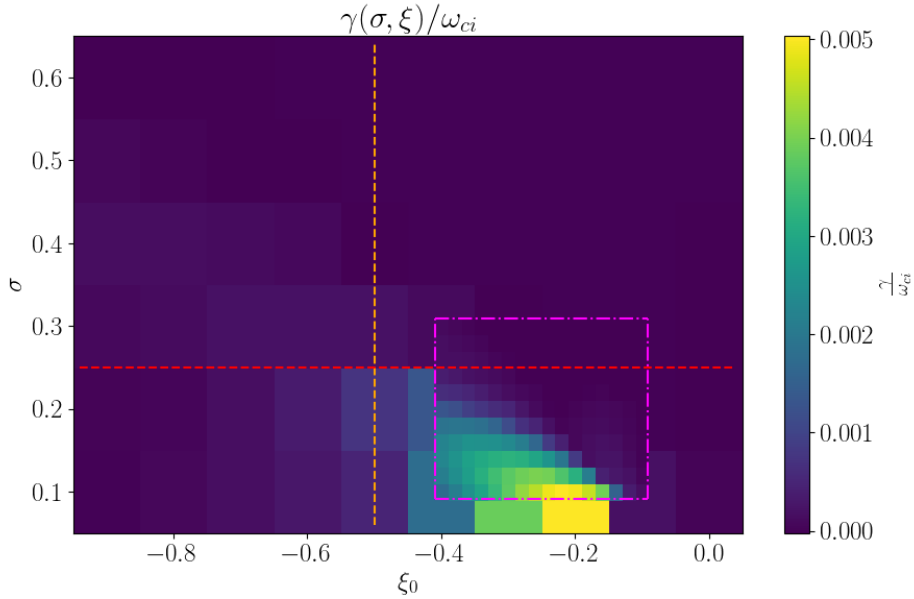
Figure 4.5: EGAM growth rate (γ/ω_{ci}) as function of ξ_0 and σ_ξ (NLED-AUG case)

In the previous subsections we found threshold values for the ASD parameters σ_ξ and ξ_0. As a reference, the two dashed lines in fig. 4.5 represent the sections along which

the scans in ξ_0 (red dashed line) and σ_ξ (orange dashed line) have been performed and shown respectively in section 4.3.2 and 4.3.1. In next section we will offer an insight on the evaluation of which areas of the EP distribution functions contributed to the excitation or damping of the GAM [48]. The tools presented in section 4.3.4 will enable us to determine why some ASD distribution function trigger the EGAM instability, and other do not, helping us to find the areas of F_0 with positive $v_\parallel$ gradients, which drive the EGAM, and resonant velocities crucial for a deep comprehension of the phenomenon of the destabilization of the EGAM. After that we will also move to a scan in EP density concetration aiming to find a threshold value also for this parameter (sec. 4.3.5).

4.3.4 Phase space analysis

In this section we present an analysis of the mode-particle power exchange measured through a particular diagnostic in ORB5 which is able to measure the power exchange in electrostatic modes between the plasma species and the electrostatic perturbation. The so called mode-particle-resonance (MPR) diagnostic for ORB5 was developed in order to analyze at which velocities the particles of a distribution function were contributing the most to the excitation or damping of the mode [48]. The resonance velocity can be analytically evaluated using eq. 41 of [48]:

$$v_{\parallel,res} = qR_0\omega_{GAM}, \tag{4.18}$$

where the frequency of the GAM is ω_{GAM}, q is the safety factor and R_0 the major radius of the tokamak. We yielded such an expression of the resonance velocity also in section 4.1 (see denominator of eq. 4.11). Plugging into eq. 4.18 the parameters of the NLED-AUG case, being $q \simeq 2.3$ (which is the average value of q where the EGAM is peaked betweeen $s \sim 0.4 - 0.6$, fig. 3.1 right), $R_0 = 1.66$ m, $\omega_{GAM} = 35560$ rad/s, from the $\xi_0 = -0.5$, $\sigma_\xi = 0.2$ simulation, we yield the first resonant velocity:

$$v_{\parallel,res} = qR_0\omega_{GAM} = 1.36 \cdot 10^5 \; m/s \; . \tag{4.19}$$

If we normalize eq. 4.19 with respect to the sound speed $v_s = \sqrt{k_B T_e/m_i} = 1.88 \cdot 10^5$ m/s, we yield:

$$v_{\parallel,res,norm} = \frac{v_{\parallel,res}}{v_s} = 0.723 \; . \tag{4.20}$$

Using the MPR diagnostic in ORB5 [48], we can save its values (saved on a phase-space grid) and plot them superimposed to the ASD distribution function as in fig. 4.6. It will be shown that this is a very convenient way to represent the MPR diagnostic because it will show which particles of the distribution in phase-space contribute to

the excitation or damping of the mode. We note that the parallel velocity at which most of the power is exchanged between the particles and the mode is approximately at $v_{\parallel,norm} \simeq 0.8$ (red cross in figure 4.6) very close to the analytical estimate from eq. 4.20, proving the accordance between the theory and the numerical simulations.

As the MPR power exchange is computed as the time derivative of the plasma kinetic energy, see eq. (1) in [48], the growth rate can be estimated from this kind of diagnostic according to eq. (5) and (6) of [48]:

$$\gamma = \sum_{sp} \gamma_{sp} = -\frac{1}{2} Re \left[\left\langle \frac{P}{\varepsilon} \right\rangle \right], \tag{4.21}$$

$$P = \sum_{sp} P_{sp} = \sum_{sp} \int \mathbf{J}_{sp} \cdot \mathbf{E} \, dV, \tag{4.22}$$

with $\mathbf{J}_{sp}$ calculated as in equation 3.13 being the current of the species and $\mathbf{E}$ the electrostatic field computed from the Poisson equation 3.12. Equation 4.22 offers the definition of P as the work done by the electrostatic field on the plasma. This definition implies that negative MPR power contributions $P(v_{\parallel}, \varepsilon) < 0$ (the majority in fig. 4.6) corresponds to the case where plasma kinetic energy decreases because the energy is transferred from the particles to the field. Therefore, $P(v_{\parallel}, \varepsilon) < 0$ represents a local positive power contribution for the mode, leading to the excitation of it. In fact, in 4.21 γ has the opposite sign with respect to P. Subsequently, for excited modes we will observe most of MPR diagnostic plots (as in fig. 4.6) to be rather negative and in damped ones to be positive.

As expected from the considerations in sections 2.3, 3.3, 4.3, we observe that the area of the distribution function contributing to the excitation of the mode has a positive gradient of the distribution function F_0 in $v_{\parallel}$ (red contour lines in figure 4.6). Meanwhile, we see also damping contributions on the left of the graph, in correspondence of negative gradients of F_0 with respect to $v_{\parallel}$. In general we can state:

$$\frac{\partial F_0}{\partial |v_{\parallel}|} > 0 \implies P_{sp} = \mathbf{J} \cdot \mathbf{E} < 0 \implies \gamma > 0 \implies \text{excitation contribution}, \tag{4.23}$$

$$\frac{\partial F_0}{\partial |v_{\parallel}|} < 0 \implies P_{sp} = \mathbf{J} \cdot \mathbf{E} > 0 \implies \gamma < 0 \implies \text{damping contribution}. \tag{4.24}$$

All the previous considerations can be observed in the following plot (fig. 4.6). It represent the MPR diagnostic from the simulation using the ASD F_0 with $\xi_0 = -0.5$ and $\sigma_\xi = 0.2$ superimposed to the same ASD F_0 in phase-space representation. In this plot the power exchanged between the mode and the particles (eq. 4.22) has been

integrated over time and normalized with respect a reference value of power.
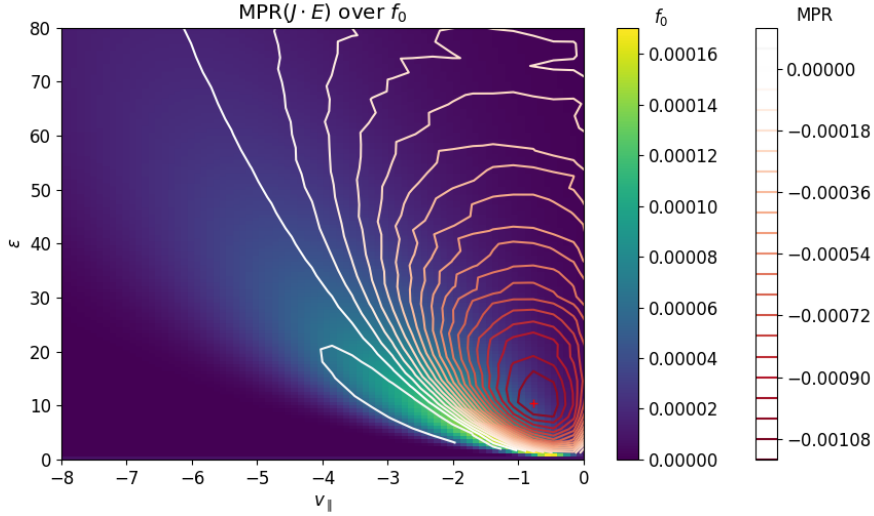
Figure 4.6: MPR diagnostic data $(J \cdot E)$ superimposed to $F_0(s = 0.5, v_{\parallel}, \varepsilon)$ taken from NLED-AUG case simulation with ASD F_0 ($\xi_0 = -0.5$, $\sigma\xi = 0.2$). A red cross is added to mark the location of the most negative value of the MPR. MPR diagnostic is measured in ORB5-normalized units

Other examples of this diagnostic will be used throughout this Chapter 4, for example in section 4.4, where we will use it to compare the ASD F_0 effects in phase space on the mode compared to those from the RABBIT F_0.

In next section we will present the results from numerical simulations using two different ASD distribution functions ($\xi_0 = (-0.5, -0.9)$, $\sigma_\xi = 0.2$) and varying the EP concentration to study the dependence of the growth rate and frequency on this plasma parameter. Threshold values for this parameter are found numerically.

4.3.5 Scans in energetic particle concentration and threshold values

In this section we scanned with respect to the volume averaged fast particle concentration $\langle n_{EP}/n_e \rangle$ two of the previous simulations, namely the one using ASD with $\xi_0 = -0.5$, $\sigma_\xi = 0.2$ and another one with $\xi_0 = -0.9$, $\sigma_\xi = 0.2$. Analyzing the two scans, we infer how the ξ_0 parameter influences the threshold values of EP concentration. Again, we ran the scans using the NLED-AUG case configuration described in section 3.2. Results are reported in figures 4.7 to 4.9. The former shows the modes in time for the two values of ξ_0 as $\langle n_{EP}/n_e \rangle$ varies between between $(0.02, 0.095)$ for $\xi_0 = -0.5$

and $(0.02, 0.20)$ for $\xi_0 = -0.9$. The latter shows the trends of γ and ω with respect to the EP concentration. It is well known that as the EP particle fraction increases the growth rate γ increases too [44, 91, 100–102, 109, 110]. Our results confirm this hypotesis, yielding steadily growing growth rates as $\langle n_{EP}/n_e \rangle$ raises. Nevertheless, as we can see from both figures below, the $\gamma = 0$ threshold value is found at different EP fractions for the two cases. The simulations with $\xi_0 = -0.9$ are all more stable with respect to the $\xi_0 = -0.5$ ones, consistently with previous results. Infact, the density threshold value for $\xi_0 = -0.9$ is higher:, $\langle n_{EP}/n_e \rangle_{thr} \simeq 0.045$, while for $\xi_0 = -0.5$: $\langle n_{EP}/n_e \rangle_{thr} \simeq 0.025$. It was difficult to precisely establish the exact threshold value because modes from the simulations near marginal stability show a decreasing behavior before a weakly linear growing phase.
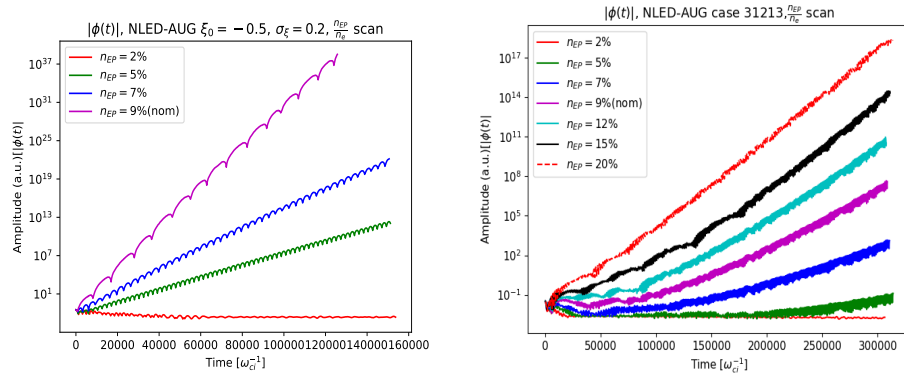
Figure 4.7: Scalar potential modes in time of $\frac{n_{EP}}{n_e}$ scan for $\xi_0 = -0.5$ (left) and $\xi_0 = -0.9$ (right) in NLED-AUG case
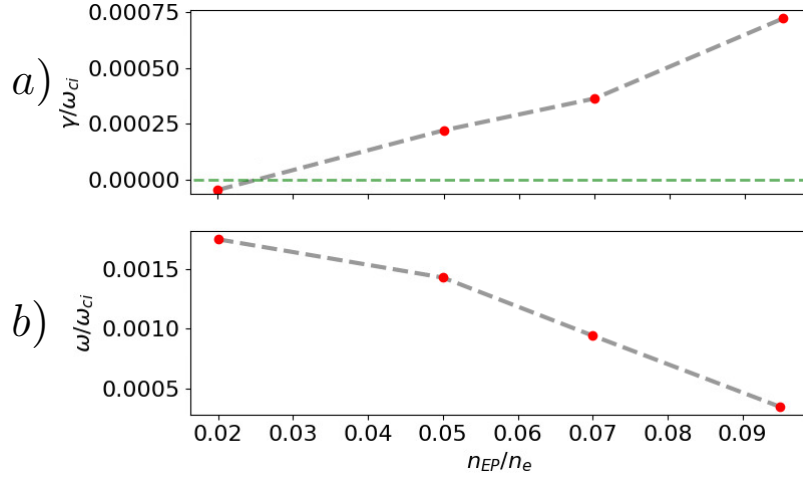
Figure 4.8: Growth rate (**a**) and frequency (**b**) dependence on $\frac{n_{EP}}{n_e}$ for EGAMs using an ASD with $\xi_0 = -0.5$ in NLED-AUG case. The red dots in the plots represent the correspondent γ and ω from the simulations in fig. 4.7(left). The green dashed line in the top figure represents the $\gamma = 0$ threshold
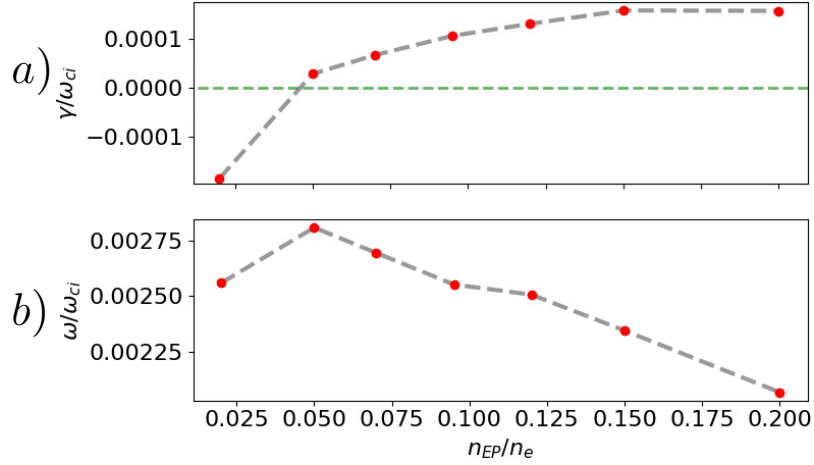
Figure 4.9: Growth rate (**a**) and frequency (**b**) dependence on $\frac{n_{EP}}{n_e}$ for EGAMs using an ASD with $\xi_0 = -0.9$ in NLED-AUG case. The red dots in the plots represent the correspondent γ and ω from the simulations in fig. 4.7(right). The green dashed line in the top figure represents the $\gamma = 0$ threshold

Such scans will be proposed also for the RABBIT distribution function in section 4.4. Before moving to the simulations with numerical EP distribution functions from RABBIT, in the next section we show a scan over ion temperature for a simulation of the previous set.

4.3.6 Effects of ion Temperature

Among the plasma parameters that can affect the growth or damping rate there's plasma temperature [44]. Bulk ions get heated by GAMs while damping them through the Landau damping (sec. 2.2). This is the reason why GAMs are believed to be a quite useful tool to transfer energy from the EP species to the bulk plasma [48]. The direct Landau damping also depends on resonant velocities and varying the temperature of thermal ions can move the gradients of the ion distribution function closer to these resonant velocities, enhancing the damping of the mode. Therefore, changing the temperature of the bulk ions strongly affects their damping effect on the EGAM. If we take eq. 4.18 and consider that GAMs can have higher poloidal sidebands with $m \geq 1$, we can infer that the resonant velocity has different values according to the different sidebands [48]:

$$v_{\parallel,res}^m = \frac{qR_0\omega_{GAM}}{m}.$$
(4.25)

In spite the fact that we can have multiple resonant velocities, numerical computations proved that the energy transfer between mode and thermal particles occurs mostly at the first resonant velocity [48]. The full width at half maximum (FWHM) of the Maxwellian distribution function of thermal ions is proportional to the square root of temperature:

$$\text{FWHM} \propto \sqrt{\frac{T_i}{m_i}}\ .$$
(4.26)

This can be seen qualitatively also in fig. 4.10.
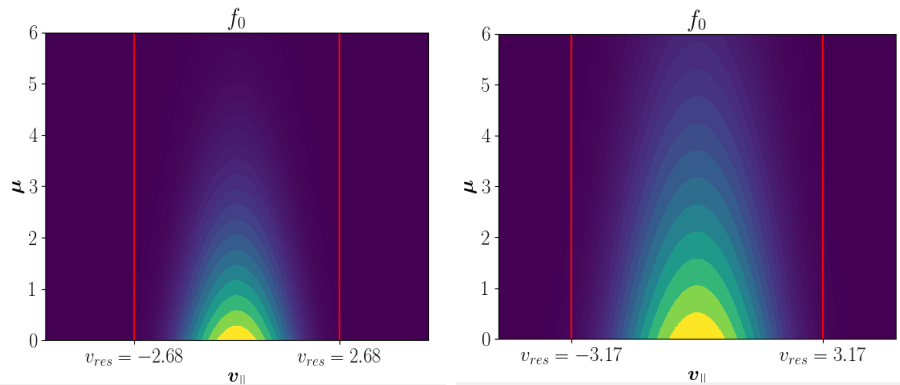
Figure 4.10: Distribution functions of thermal ions represented in $(v_\parallel, \mu)$ velocity space with $T_i/T_e = 2.5$ (left) and $T_i/T_e = 4.5$ (right), red vertical lines highlight resonant velocities as computed from eq. 4.25

As we observe in the figure 4.10, $v_{\parallel,res}$ intersect the ion distribution function in denser areas of the distribution function for higher values of $\tau = \frac{T_i}{T_e}$, and viceversa for lower values of τ. This implies that the GAM mode can redistribute more energy to the thermal ion species if T_i is higher leading to a stronger damping effect by the bulk ions. It is interesting to note that the resonant velocities for higher temperatures are also higher, the resonant velocity is, in fact, depending on ω_{GAM} which is:

$$\omega_{GAM} = \frac{v_{th}}{R_0}\sqrt{\left(\frac{7}{4} + \frac{T_e}{T_i}\right)}, \tag{4.27}$$

where $v_{th} = \sqrt{2T_i/m_i}$. So the final dependence of $v_{\parallel,res}$ is:

$$v_{\parallel,res} \propto \sqrt{\frac{T_i}{m_i}\left(\frac{7}{4} + \frac{T_e}{T_i}\right)}. \tag{4.28}$$

Comparing equation 4.28 to 4.26, we see that the FWHM grows faster than the $v_{\parallel,res}$ enabling the process for increasing T_i that was previously described and depicted in fig. 4.10.

In order to analyze the effects of ion temperature, a scan of simulations varying τ in a range of values has been permormed using the NLED-AUG case configuration with an ASD F_0 characterized by $\xi_0 = -0.5$ and $\sigma_\xi = 0.3$. Figure 4.11 and 4.12 clearly present the effect of ion temperature. Accordingly to theoretical expectations [44], in fig. 4.11 the fastest growing modes are those with lower values of τ. In figure 4.12, the growth rates are plotted as function of τ and we can see the γ trend is monotonically decreasing with τ. Meanwhile, the frequency shows the opposite behaviour, in fact, it increases with τ. Again, this is due to the transition from strongly growing EGAMs with low frequency to weakly growing EGAMs with higher frequency, getting closer to the frequency of damped GAMs. Moreover, the EGAM frequency can be written as in equation 4.27. Therefore, higher values of T_i correspond to higher values of GAM frequency.
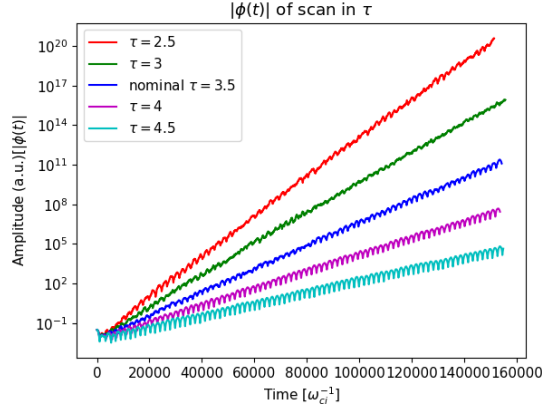
Figure 4.11: EGAM mode amplitudes in time of a scan in τ, ranging from 2.5 to 4.5, for NLED-AUG case
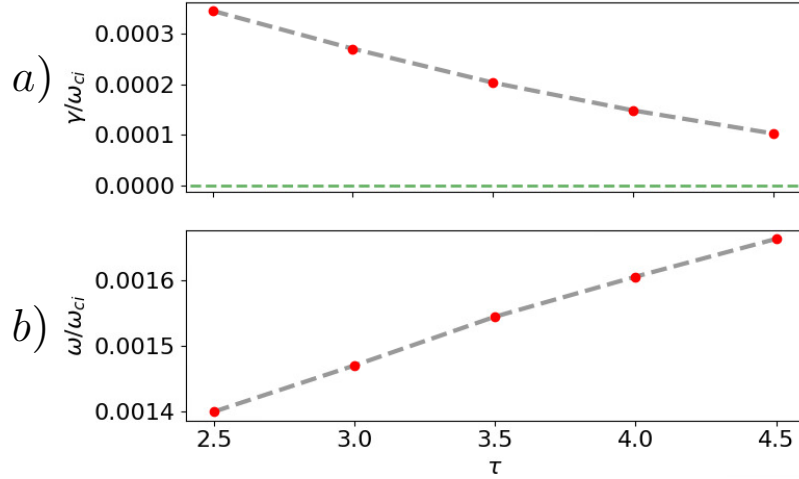
Figure 4.12: Growth rate γ/ω_{ci} (a) and frequency ω/ω_{ci} (b) of the scan in τ shown in fig. 4.11. The red dots in the plots represent the correspondent γ and ω from the simulations in fig. 4.11. The green dashed line in the top figure represents the $\gamma = 0$ threshold

In this section 4.3, we analyzed the dependence of the EGAM growth rate on the two parameters of the analytical ASD distribution function: ξ_0 and σ_ξ. Furthermore, we studied the influence on the stability of the GAM of relevant plasma parameters such as EP density concentration and ion temperature. We have found sensible influence from all these parameters. Moreover, we made use of the MPR diagnostic to enquire into the driving mechanisms of EGAMs generated by anisotropy. We have now the tools to investigate the linear stability of GAMs using the most realistic distribution function available to ORB5, namely the RABBIT F_0.

4.4 Numerical results using the RABBIT distribution functions

In this section we will show the results obtained running NLED-AUG case simulations as those shown in section 4.3. The only difference in the input was the distribution function. We used the four different distribution functions of the NLED-AUG case (shots #3123-6 in AUG) with the correspondent density and temperature profiles shown in section 3.3.2. As already explained, these distribution functions were produced changing the injection angle of the NBI with respect to the magnetic axis of the machine. Therefore not only we will have slightly different distribution functions, but also the radial density profiles will be peaked at different radial positions. Shot #31213 has the most off-axis angle (7.13°) and the most off-axis profile, peaked at $s \sim 0.4$, shot #31214 the most on-axis (6.07°) NBI and the radial peak at $s \sim 0.3$. Shots #31215-6 have a mid-range angle (6.65°) and density profiles. For clarity we show again the four RABBIT distribution functions in figure 4.13, details in section 3.3.2.
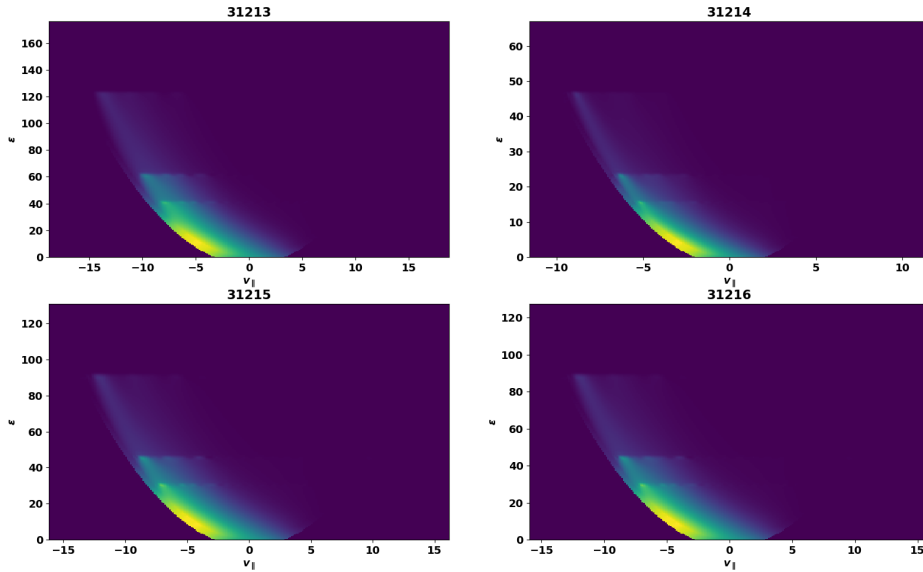
Figure 4.13: Realistic distribution functions generated from RABBIT, NLED-AUG case shots # 31213-6

The ORB5 linear electrostatic simulations' results using the different EP RABBIT distribution functions are plotted in figure 4.14. We immediately note that the modes are all damped, yielding negative growth rates, in spite the different injection angles. In fact, as we found in section 4.3, such NBI angles correspond to high pitch $\xi_0 \sim -0.9$

values which yield rather stable modes. Nevertheless the frequencies are still in in the range of $\omega \simeq 0.04\omega_A$, which are the frequency found in section 4.3 for the damped GAMs (figure 4.4 b)). We will see in next sections why the RABBIT distribution function has such negative growth rates if indirectly compared to the analytical ASD distribution function We will find EP density concentration thresholds for the different injection angles as done in section 4.3, finally a comparison with the experimental measurements will be offered.
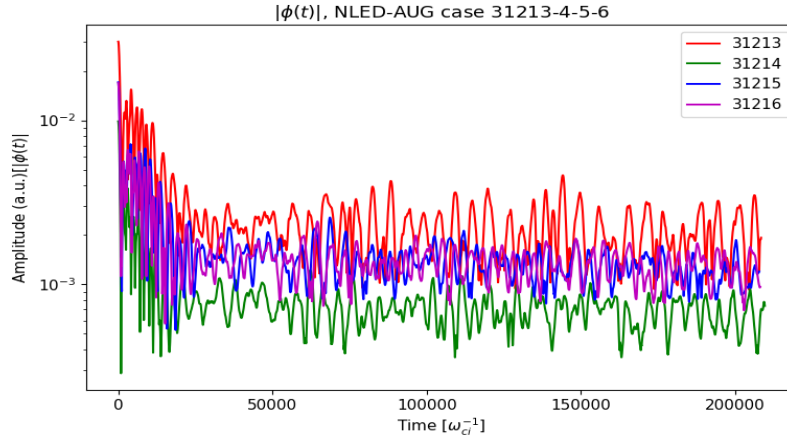
Figure 4.14: NLED-AUG case $n = \{0\}$ modes in time for the four shots, using the four different RABBIT distribution functions showed in fig. 4.13

4.4.1 MPR diagnostic from RABBIT distribution functions

In this section we offer a new phase space analysis as done in section 4.3.4, this time applied to the linear ORB5 simulation using the RABBIT F_0 from AUG shot #31213 (sec. 3.3.2). We present the MPR plot superimposed to the RABBIT distribution function in figure 4.15, in a similar fashion to what shown in figure 4.6. As in equation 4.10, we calculate the theoretical estimate for the normalized parallel resonant velocity, being $q \simeq 2.3$, $R_0 = 1.66$ m and $\omega_{GAM} = 2.04 \cdot 10^5$ rad/s:

$$\frac{v_{\parallel,res}}{v_{th,i}} = \frac{qR_0\omega_{GAM}}{v_{th,i}} = 4.15. \qquad (4.29)$$

The results represented in figure 4.15 offers much more complex structure than that shown in image 4.6. In the plot below, there are many peaks, both negative and positive, positioned in different points of the phase space correspondent to different point of the RABBIT F_0. In Fig 4.15, we observe that the highest negative peak, at which the positive contribution to the mode excitation takes place, is located in the middle of a

positive gradient area of the F_0 (see eq. 4.23) at $v_\parallel \simeq -4.85$. This $v_\parallel$ value is very close to the main resonant velocity found in eq. 4.29. Moreover, according to eq. (42) of [48], there can be many resonant velocities due to the exchange of energy taking place at higher poloidal harmonics ($|m| \geq 1$). Hence, we can find other resonant velocities using the following formula:

$$v_{\parallel,res}^{(m)} = \frac{qR_0\omega_{GAM}}{m}.$$

(4.30)

In fact, observing closely figure 4.15, we notice a smaller negative peak located near to another resonant velocity at $v_\parallel = -1.34$. If we consider m=3, and plug it into eq. 4.30, $v_{\parallel,res}^{(3)} \simeq 1.38$, very close to the secondary resonant velocity, found by the MPR diagnostic, at which a peak of the power exchange is found (fig. 4.15). In the figure we can find also other negative peaks either near the main resonance velocity (eq. 4.29) or the other poloidal mode velocities (eq. 4.30), at higher energies.

Furthermore, it is interesting to note the position of the positive peaks too, those causing the damping of the mode according to equation 4.24. In fact, most of these are located just above each of the three injection velocities (E_0, $E_0/2$, $E_0/3$). This result agrees with the theory [47]. According to the general Landau damping mechanism (equation 2.31) the areas of the distribution function where $\partial F_0/\partial\varepsilon < 0$ damp the mode. In fact, in correspondence of the injection velocities we have very steep negative gradients in energy (or absolute velocity $|v|$) which damp the mode. In other words, the largest part of particles in these discontinuities can be only accelerated, gaining energy from the mode and, therefore, generating a damping effect on the GAM.
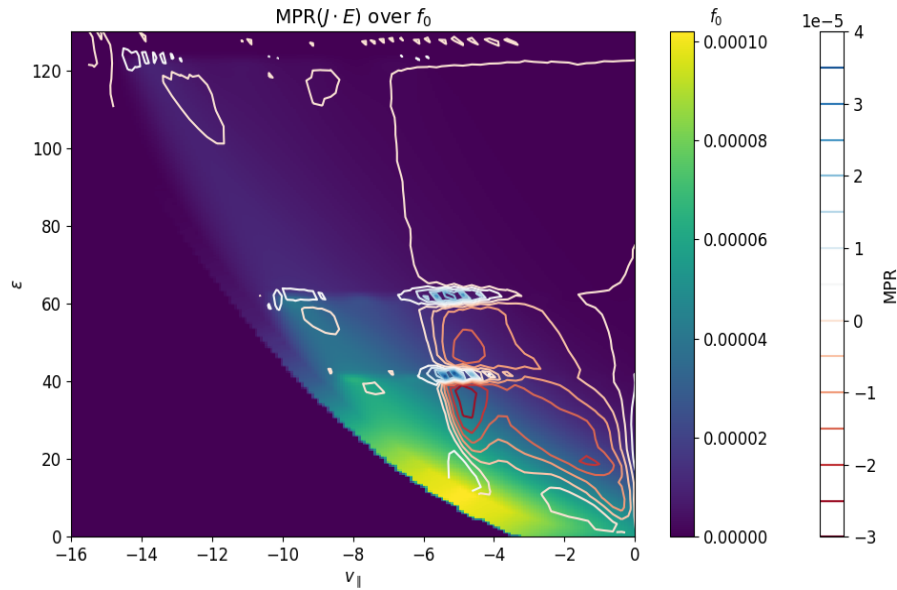
Figure 4.15: MPR diagnostic $(J \cdot E)$ superimposed to RABBIT $F_0(s = 0.5, v_\parallel, \varepsilon)$ of NLED-AUG case shot # 31213. The MPR diagnostic as well as the distribution function have been represented in ORB5-normalized units

In figure 4.16 we present a zoom of figure 4.15. In this plot, it is possible to observe more closely the position of the positive peaks of the MPR diagnostic along the steep negative gradients in energy (almost discontinuities) of the distribution function $\partial f_0 / \partial \varepsilon < 0$. Such negative gradients are due to the different injection velocities of the NBI caused by the different ionization states of the NBI fuel (deuterium). We immediately note that this RABBIT feature causes strong positive power exchange from the mode to the particles (eq. 4.24), causing the mode to be more damped than excited. This feature and, subsequently this strong negative drive in the GAM, was not present in the analytical ASD F_0. A more thorough comparison between the results using the RABBIT and the ASD distribution function will be offered in section 4.4.3. So far, we limit our observations to the fact that this injection velocities seem to cause substantial differences to the drive of the GAM between the analytical and numerical EP distributions.
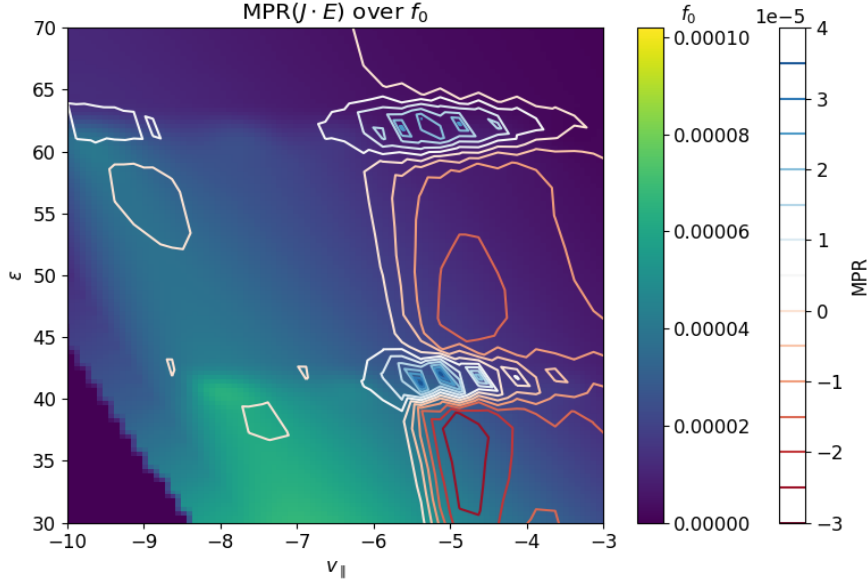
Figure 4.16: MPR diagnostic $(J \cdot E)$ superimposed to RABBIT $F_0(s = 0.5, v_\parallel, \varepsilon)$ of NLED-AUG case shot # 31213 (zoom of figure 4.15)

In this section we analyzed the MPR diagnostic measured from the NLED-AUG case simulation using the numerical RABBIT distribution function from shot #31213. We could see that the steep negative gradients in ε cause the mode to be rather damped. In the next section we will run scans in EP density concentration for the different injection angles of NLED-AUG case, as in section 4.3.5.

4.4.2 Results and threshold values for RABBIT distribution functions

In order to evaluate if and which effect the different injection angles of the NBI have on the stablity of the GAM, it is of interest to study the EP concentration threshold values for the RABBIT distribution functions #31213-4-6. Therefore, for these distribution functions, scans in the EP fraction have been run as in section 4.3.5. We have set $\langle n_{EP}/n_e \rangle$ to different values comprehended between 2% and 50%. It is important to mention that such high value of EP concentration is not realistic. In fact, as it will be shown in the next section, such high EP concentrations could easily lead to non-physical conditions. It is just an arbitrary value chosen for the purpose to clearly identify the threshold values and show that the growth rate of the EGAM increases along with EP concentration.

The results have been plotted and analyzed for the different distribution functions.

We analyze case by case the three shots, in order: #31213,4,6.

EP density threshold values for shot #31213

We performed with ORB5 a scan with the distribution function and the profiles from shot #31213. The scan was run with EP concentration up to $\sim 50\%$. As aforementioned, such a high concentration is a sort of upper limit in this kind of scans. In fact, $\langle n_{EP}/n_e \rangle$ is a volume-averaged values and for higher concentrations than this, there is a serious risk of encountering local values of EP concentration that exceed the electron concentration in the ORB5 code. This situation can lead to non-physical results, in fact in such cases we would break quasi-neutrality. Additionally, in such extreme cases, various quantities that rely on bulk plasma parameters lose their significance. For instance, the GAM frequency, which is dependent on T_i, becomes unreliable in these scenarios.

Figure 4.17 present the various modes, generated by the different $\langle n_{EP}/n_e \rangle$ values, in time on the left. On the right the figure shows the growth rates and frequencies of the modes as function of $\langle n_{EP}/n_e \rangle$. A continuous increase of growth rate γ with the EP fraction is observed, in accordance with literature [44, 91, 100, 102, 109]. On the other hand, as expected, measured frequencies drop as the modes transition from damped GAMs to excited EGAMS. From the plots in figure 4.17, we can infer a EP concentration threshold value for simulations with EP distribution function from shot #31213: $\langle n_{EP}/n_e \rangle_{thr} = 0.23$.
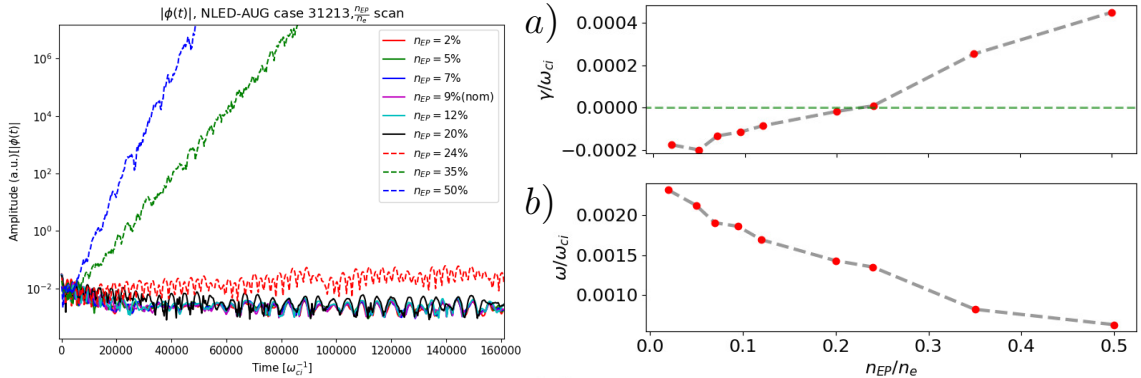
Figure 4.17: $\langle n_{EP}/n_e \rangle$ scan for NLED-AUG case shot #31213 simulations, modes in time (left), modes' growth rates (a) and frequencies (b) as function of $\frac{n_{EP}}{n_e}$ (right). The red dots in the plots on the right represent the correspondent γ and ω from the simulations in the left plot. The green dashed line in the top right figure represents the $\gamma = 0$ threshold

EP density threshold values for shot 31214

We perform the same scan in $\langle n_{EP}/n_e \rangle$ for simulations of NLED-AUG case shot #31214. In this shot the NBI angle was the most on-axis one (see section 3.3.2). Again, the upper limit of our scan was $\langle n_{EP}/n_e \rangle = 0.5$. The results are reproduced in figure 4.18 which is structured as fig. 4.17.

Based on these results, we observe the usual behavior of the growth rate and frequency depending on EP concentration. The former increases, the latter decreases as $\langle n_{EP}/n_e \rangle$ is increased. In the simulations of AUG case, shot #31214 (fig. 4.18), we find that the threshold value, indicating the transition to instability, is higher compared to case #31213. This implies that case #31214 is more stable, with the energetic particle beam being more on-axis with respect to shot #31213 (6.05° against 7.15°). This observation aligns with the discussions in section 4.3, as the more on axis cases (pitches $\xi_0 \sim -1$) have lower growth rates and higher threshold $\langle n_{EP}/n_e \rangle$ values than off-axis cases ($\xi_0 \sim -0.5$). By analyzing the plots in figure 4.18, we can determine a threshold value for case #31214 at approximately $\langle n_{EP}/n_e \rangle_{thr} \simeq 0.32$.
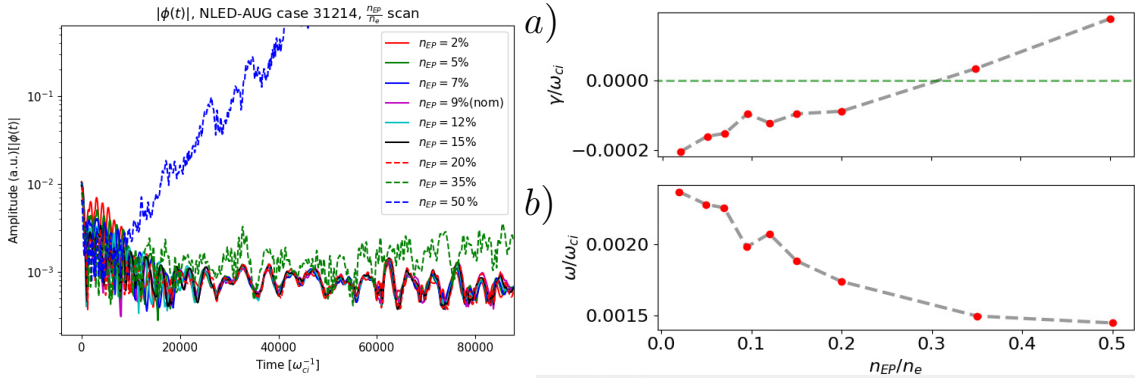
Figure 4.18: $\frac{n_{EP}}{n_e}$ scan for NLED-AUG case shot #31214, modes in time (left), modes' growth rates (a) and frequencies (b) as function of $\frac{n_{EP}}{n_e}$ (right). The red dots in the plots on the right represent the correspondent γ and ω from the simulations in the left plot. The green dashed line in the top right figure represents the $\gamma = 0$ threshold

EP density threshold values for shot 31216

For case #31216, the simulation scan varying EP concentration was repeated, and as before, we reached $\langle n_{EP}/n_e \rangle = 0.5$. We didn't ran a scan using the shot #31215 F_0 because the NBI injection angle for this case was the same of shot #31216 (6.65°). The results are shown in fig. 4.19. The trend observed is consistent with the previous cases: an increasing fraction of energetic particles leads to an increase in growth rate γ and a decrease in frequency ω (fig. 4.19). Since the injection angle is 6.65° (in

between the two previous NBI angles), we can estimate that the growth rate threshold would be found between the threshold values obtained for shots #31213 and #31214. Remarkably, our findings align with this expectation, and we can measure that in this case $\langle n_{EP}/n_e \rangle_{thr} \simeq 0.27$, as depicted in fig. 4.19.
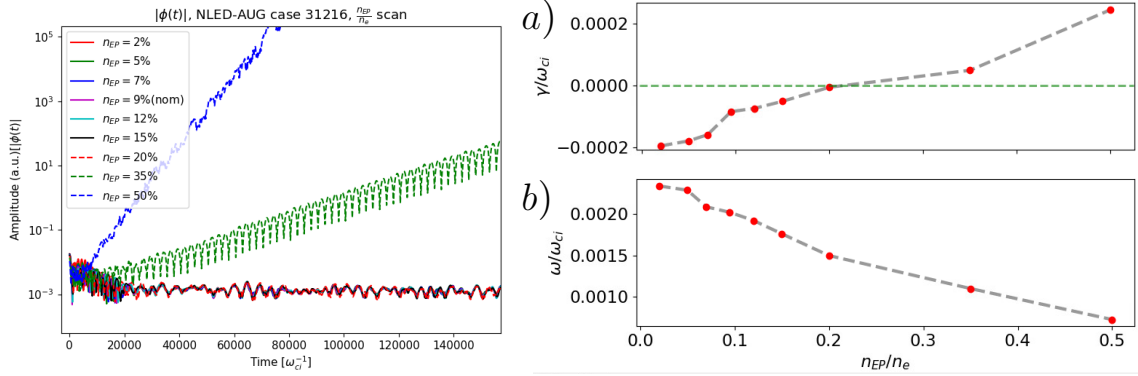

Figure 4.19: $\frac{n_{EP}}{n_e}$ scan for NLED-AUG case shot #31216, modes in time (left), modes' growth rates (a) and frequencies (b) as function of n_{EP}/n_e (right). The red dots in the plots on the right represent the correspondent γ and ω from the simulations in the left plot. The green dashed line in the top right figure represents the $\gamma = 0$ threshold

As we have observed, at nominal EP fraction $\langle n_{EP}/n_e \rangle = 0.09$ all the GAMs from linear electrostatic simulations using realistic RABBIT EP distribution functions are damped (fig. 4.14). In order to appreciate the different influences of the NBI angles, we ran scans in $\langle n_{EP}/n_e \rangle$, looking for threshold values for this quantity. Referring to the findings in 4.3, we can expect the most off-axis F_0 (shot #31213) to have the lowest threshold $\langle n_{EP}/n_e \rangle$ value and the most on-axis one (shot #31214) to have the highest threshold value. The simulations presented in this section validate such hypotesis, along with the theory presented throughout this thesis. In the next section we will perform a qualitative, indirect comparison between the simulations run with the analytical ASD EP distribution functions and those with the numerical RABBIT one.

4.4.3 Comparison with analytical ASD results

In this section we want to offer to the reader an indirect, qualitative comparison between the linear electrostatic results obtained running ORB5 set with the NLED-AUG case configuration using the analytical ASD and the numerical RABBIT EP distribution functions. To this purpose, we pick the #31213 F_0 and we need to pick an analytical ASD F_0 which resembles the RABBIT one. From the observations done in section 3.3.3, we see that the best fit of the #31213 RABBIT F_0 is an ASD with $\xi_0 \sim -0.8$ and

$\sigma_\xi \sim 0.2$. Nevertheless, for this comparison we will pick the ASD with $\xi_0 = -0.9$ and $\sigma_\xi = 0.2$, being this a lower limit for the growth rate (sec. 4.3.3) and not being too different from the $\xi_0 = -0.8$ case in terms of growth rate and frequency.

If we compare the threshold values from section 4.4.2 with those from section 4.3.5, we immediately note the very large difference between the threshold values obtained in the #31213 RABBIT case and the analytical slowing down whose parameters are $\xi_0 = -0.9$ and $\sigma_\xi = 0.2$.

As stated in the respective sections, the RABBIT case presents a threshold value of $\langle n_{EP}/n_e \rangle_{thr} \simeq 0.23$, while the analytical slowing down case has $\langle n_{EP}/n_e \rangle_{thr} \simeq 0.07$. This large discrepancy is caused by the significant difference in phase-space gradients between the two distribution functions, which strongly affects the driving and damping of the modes. This effect is clearly demonstrated with a comparison between fig. 4.15 (displaying the MPR diagnostic for RABBIT case 31213) and fig. 4.20 (plotting the MPR diagnostic for the analytical slowing down with $\xi_0 = -0.9$ and $\sigma_\xi = 0.2$, superimposed to the ASD F_0 in phase space). The main region of the drive is shared by both distribution functions (highlighted by the red-colored contour plot) and, in both cases, corresponds to areas with positive gradients of the distribution function in parallel velocities, as discussed in the previous sections. These positive gradients are capable of driving EGAMs unstable through inverse Landau damping (equation 2.31). Nevertheless, in the case of the RABBIT distribution function (fig. 4.15), this driving mechanism is hindered by the steep negative gradients in energy, as discussed in section 4.4.1, whose location coincides with the main region where the analytical distribution function simulation finds the peak and hence the highest contribution to the drive (figure 4.20).
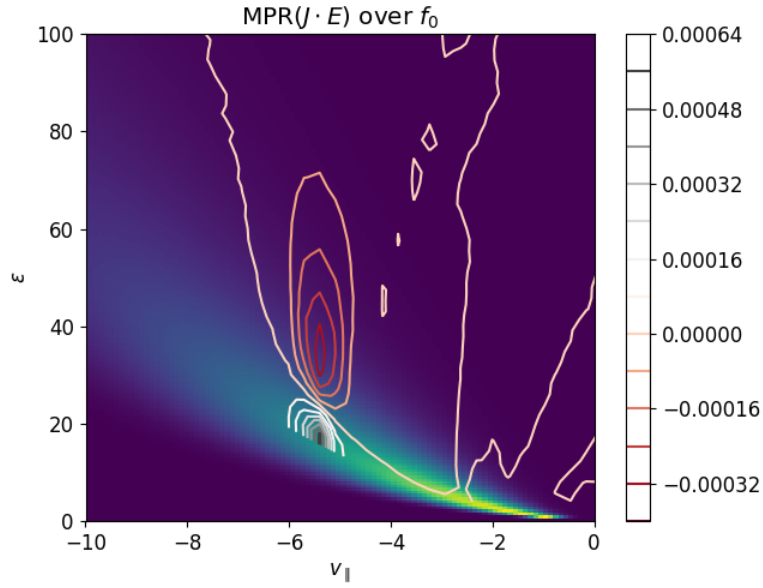
Figure 4.20: MPR diagnostic for the analytical slowing down with $\xi_0 = -0.9$ and $\sigma_\xi = 0.2$, superimposed to its F_0 in $v_\parallel, \varepsilon$ phase space

Additionally, we must consider the pitch angle scattering effect present in RABBIT distribution functions, particularly at lower energies where the majority of particles are concentrated. This isotropization effect, which is not accounted for in the analytical ASD distribution, leads to much less steep gradients in parallel velocity for the RABBIT F_0, thus hindering higher growth rates. When considering these combined effects, they could potentially explain the differences in growth rates observed in fig. 4.21 between the two distribution functions. Figure 4.21 shows the growth rates trends of the two scans of simulations of NLED-AUG case using in one case the ASD F_0 with $\xi_0 = -0.9$ and $\sigma_\xi = 0.2$ (blue dots in fig. 4.21) and in the other one the shot #31213 RABBIT F_0 (red crosses in 4.21). The figure is basically the superimposition of figure 4.9 **a)** and figure 4.17 **a)**, enabling us to compare directly how the EP density concentration $\langle n_{EP}/n_e \rangle$ affects the growth rates of simulations using the different EP distribution functions. Despite the divergence in growth rates observed at low EP concentrations, the simulations exhibit a similar trend for higher concentrations, suggesting a common dependence on the EP fraction, foreseen by literature [44].
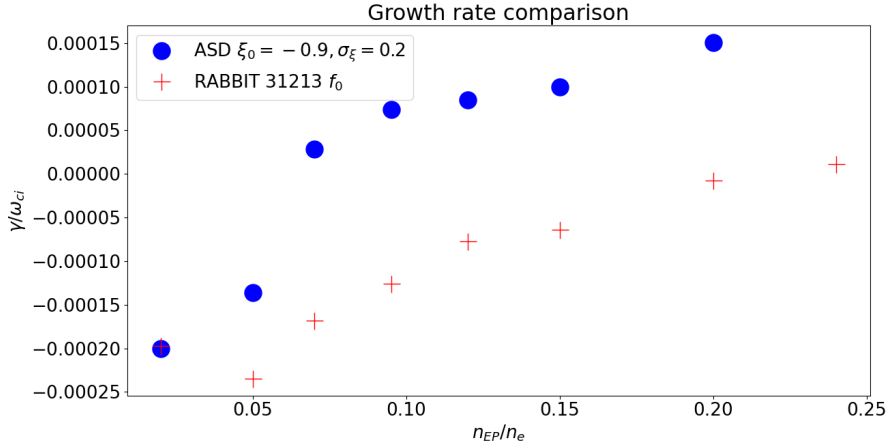
Figure 4.21: Growth rate comparison from the EP density scans using the RABBIT (red crosses) and ASD with $\xi_0 = -0.9$ and $\sigma_\xi = 0.2$ (blue dots) distribution functions

In conclusion, these results found in this whole section show that the linear drive of the RABBIT distribution functions is not enough to destabilize the EGAMs in the NLED-AUG case (at nominal $\langle n_{EP}/n_e \rangle$) as it will be explained in the next section, which will offer a comparison between the numerical results obtained running the NLED-AUG case in ORB5 with the RABBIT distribution functions and the experimental measurements of magnetic probes in AUG.

4.4.4 Comparison with experimental measurements

The results shown in the previous section are highly interesting and are consistent with the theoretical and numerical behaviors discussed in sections 4.1 and 4.3 regarding the dependencies of the GAM growth rate γ on ξ_0 and n_{EP}/n_e. The results also align with theoretical considerations from sections 2.3 and 2.2. However, when analyzing the data from the magnetic Mirnov (pick-up) coils that capture the magnetic perturbations in NLED-AUG cases (fig. 4.22), it is self-evident that the EGAM (green lines at around 50 kHz) is excited in everyone of the four cases. Observing the experimental measurements and consistently with our expectations, the most unstable case is the EGAM in the most off-axis case, shot #31213 (top left in fig. 4.22), while shot #31214 (top right in fig. 4.22), the most on axis EP distribution, exhibits the least instability. This observation agrees with the analytical and numerical findings from 2.3, 4.1 and 2.2, as well as numerical evidence from 4.3, which indicate that as ξ_0 approaches -1, the growth rate diminishes (sections 4.4.2, 4.3.2, 4.1).

We observe a rough agreement concerning the frequency between the simulations and the experimental measurements. In shot #31213 simulations, as depicted in figure

4.17 (right), the frequencies range from 17.5 to 38.5 kHz. This does not perfectly match the experimental measurements, nevertheless such result is comparable to the approximately 50 kHz measured in ASDEX-Upgrade and shown in figure 4.22 (top-left).

In our simulations we also managed to establish a stability ranking for the different NLED-AUG case shots, thus a stability ranking for the different NBI injection angles. This ranking could not be established comparing the growth rates of the mode at nominal EP concentration ($\langle n_{EP}/n_e \rangle = 0.09$) because in such conditions all the modes using RABBIT distribution functions were stable (fig. 4.14). Nevertheless, we could establish a stability order based on the scans in EP concentration. The RABBIT EP distribution which yields the lowest threshold EP concentration level can be considered to be the one causing the most unstable conditions for the GAM. According to this principle, as shown in section 4.4.2, the most destabilizing shot is #31213, the most stable is #31214 and shots #31215-6 are in between. Such results is matched qualitatively by the experimental measurements (fig. 4.22). In fact, we can observe that, as expected from theory, the most off-axis case (#31213) is causing the most intense EGAM signal, the most on-axis one (#31214) the least intense and mid range shots (#31215-6) an in between intensity of the signal.

However, despite we found a qualitative agreement in the dependence of growth rate trends on the EP concentration (section 4.4.2) and on the NBI injection angle, there is a quantitative difference. In the numerical simulations with experimental conditions and F_0, where the EP fraction is approximately 9%, all modes are damped. In contrast, in the experiments, the modes are all excited, even if with different growth rates. The threshold values for excitement in simulations with RABBIT F_0 are found at much higher EP fractions (sec. 4.4.2). This suggests that there must be a nonlinear effect, not accounted for in the electrostatic linear simulations, that drives EGAMs unstable even with such a small EP density concentration.

One possible explanation for this mismatch, as proposed in [57], is the nonlinear interaction between n=1 Alfvénic modes and EGAMs. In the same experiment, Alfvén modes such as TAE and EPM are present, as seen in figure 4.22 where such signals are observed at approximately 100-150 kHz. The excitation of these modes in the NLED-AUG case has been extensively studied in References [58, 73]. The contemporaneousness of EGAMs and TAEs, as observed in experiments, supports for the hypothesis of nonlinear interactions between these modes. Reference [57] demonstrated that Alfvén modes can trigger EGAMs, and conversely, EGAMs can nonlinearly excite Alfvén waves [58].

It is important to acknowledge that certain experimental uncertainties exist and could be involved in the observed damped behavior of GAMs in the simulations using RABBIT F_0. Firstly, among the shots analyzed, only shot #31216 had direct measurements of T_i through beam blips, while the T_i profiles of the other shots (#31213-4-5) were

reconstructed based on the data from shot #31216. It is possible that the actual T_i values in shots #31213-4-5 were smaller, leading to higher growth rates in the simulations (sec. 4.3.6). Secondly, tokamak discharges often produce impurities, the effects of which are not accounted for in these simulations. Neglecting the presence of impurities can have an impact on the plasma characteristics and the stability of modes. Additionally, the poloidal dependence of distribution function is neglected in both RABBIT and analytical ASD distribution functions.

Furthermore, it should be noted that the RABBIT distribution functions do not consider velocity diffusion effects. Including such effects would generate less steep negative gradients at the injection velocities, thereby reducing the damping effect caused by these discontinuities in F_0 (section 4.4.1).

Finally, there may be uncertainties in the q profiles, as the GAM damping is proportional to e^{-q^2}, this can sensibly shift the stability boundary for the EGAM. Considering all these factors, including the nonlinear interactions discussed earlier, it is expected that a more accurate estimation of the growth rate of EGAMs can be obtained for the NLED-AUG cases.

In conclusion, we can state that anisotropy is a crucial feature for distribution function for the linear stability of EGAMs. We found that analytical slowing-down with pitch dependency distribution functions can linearly excite EGAMs (section 4.3). Nevertheless, when using realistic distribution functions in ORB5 for simulations of the NLED-AUG case, such as those obtained from RABBIT, which present really high correspondent pitches ($\xi_0 \sim -1$), the linear stability thresholds values of EP concentration are found at much higher values than those observed in the experiment. From the experimental observations, weak EGAMs are found in phases without much Alfvenic activty (e.g. #31215), whereas when AWs are present, they reach considerably higher amplitudes (e.g. #31213). It is evident that both uncertainties in the linear parameters, such as q and F_0, as well as the non-linear electromagnetic effects discussed previously, play crucial roles in achieving quantitative agreement between simulations and experimental observations. These findings emphasize the complexity of the NLED-AUG case and highlight its importance for both linear and non-linear code validation excercises.

In the next chapter we will include non-linear electromagnetic physics into these simulations, aiming to achieve a better agreement between the ORB5 simulations and the experimental measurements. Such studies have already been started with simple distributions functions in ref. [73].
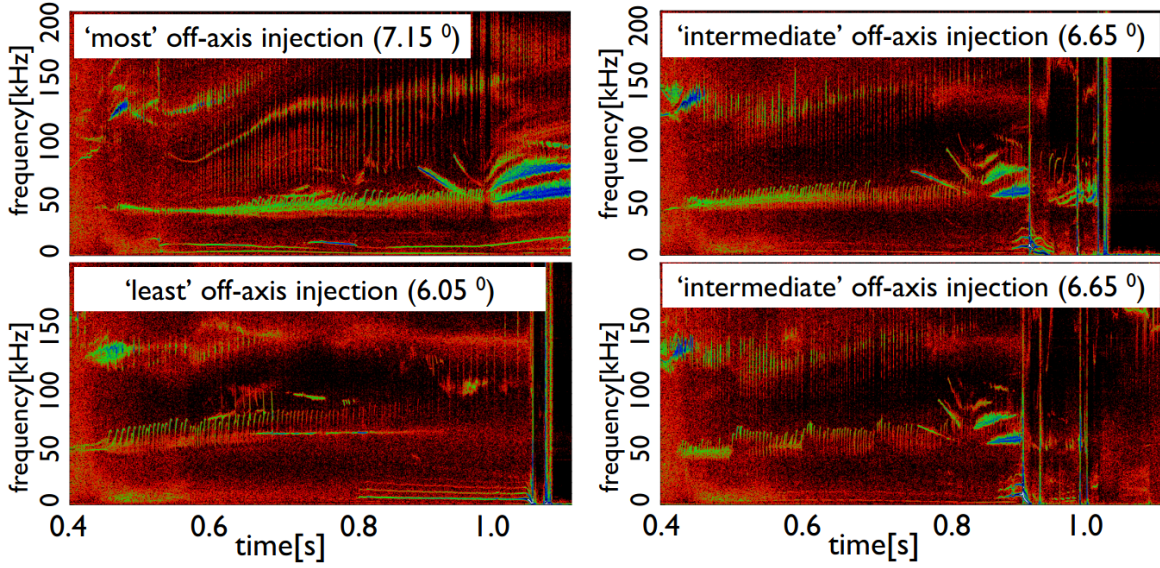
Figure 4.22: Experimental data from NLED-AUG case from magnetic Mirnov (pick-up) coils (in order top-left, top-right, bottom-left, bottom-right: 31213,5,4,6)

4.5 Discussion and chapter summary

This chapter investigated the influence of anisotropic EP distribution functions on the linear stability of Geodesic Acoustic Modes in tokamak plasmas, using the NLED-AUG case as the plasma configuration. As a first step for this study, a new analytical anisotropic and asymmetric distribution function, parametrized by ξ_0 and σ_ξ, was implemented (section 3.3.1). Theoretical analyses were performed to derive the stability conditions for extreme cases of ξ_0 and σ_ξ by examining the dispersion relation of EGAMs (section 4.1). These theoretical studies found that EGAM are excited for low values of σ_ξ and values of $\xi_0 \sim -0.5$. This method could not evaluate threshold values for the parameters. Therefore, numerical simulations were necessary to determine threshold values, and scans were conducted using the gyrokinetic code ORB5 to explore the stability of EGAMs over the parameter space of ξ_0, σ_ξ, and the EP density fraction $\langle n_{EP}/n_e \rangle$ (section 4.3). The results revealed that the modes become unstable for low values of σ_ξ and within the range of ξ_0 between -0.9 and -0.3. This stability region widens with decreasing σ_ξ and increasing EP fraction. The threshold value for $\langle n_{EP}/n_e \rangle$ varied depending on the specific ξ_0 and σ_ξ configuration, resulting in different values for different cases (section 4.3.5).

The power exchange structures (MPR) for different simulations were also investigated, in order to establish which populations of EPs were contributing to the excitation

and damping of the modes. It was found that, accordingly to theory (sec. 2.2), the particles of the distribution function with $\partial F_0 / \partial v_\parallel > 0$ were ceding energy to the mode exciting it and viceversa (section 4.3.4). The effects of ion temperature was also studied showing that the growth rate decreases with increasing thermal ion temperature (sec. 4.3.6). Additionally, it was found that the main resonance velocity, at which most of the power is exchanged between the mode and the particles, agrees with the theoretical expectations from section 4.1.

Furthermore, experimental-like numerical distribution functions were obtained from RABBIT and were fed as input in ORB5 to simulate the different NLED-AUG cases #31213-6, incorporating the experimental temperature and density profiles from the four different shots (sec. 4.4). The simulation results indicated that all modes were damped when using the RABBIT distribution functions, and the MPR analysis was carried out specifically for case #31213 to find out why this was the case. A more complex power exchange structure emerged from this simulations if compared to the analytical distribution function cases, in particular, the steep negative gradients at the different injection velocities seemed to be the cause for such negative growth rates for the RABBIT cases (sec. 4.4.1). This analysis also suggested that interactions between EPs and the mode occur even at higher mode resonant velocities. Scans varying the EP concentration were performed for the three shots #31213, #31214, and #31216, corresponding to three different injection angles of the NBI systems. As expected, different EP concentration threshold values were found for the different injection angles (section 4.4.2), following the trend expected from theory and the results of the simulations with analytical anisotropic F_0.

Finally, a qualitative comparison was made between the analytical F_0 results and the RABBIT F_0 results (section 3.3.3) and between the RABBIT simulation results and experimental measurements obtained from magnetic pick-up coils (section 4.4.4). In the experimental cases with the nominal EP concentration (around 9%), EGAMs were found to be excited in all the AUG cases, even though with different growth rates. However, when simulating the numerical experimental-like distribution functions and profiles at the same EP fraction, no unstable mode was found. This discrepancy hinted the need to consider nonlinear, electromagnetic physics in order to achieve fully predictive simulations of EGAM dynamics. A crucial nonlinear effect, neglected in these simulations, is the interaction between n=1 Alfvén waves and EGAMs [57], which have been observed in the NLED-AUG case and investigated in previous studies [58]. We found that the numerical realistic anisotropic distribution function alone is unable to linearly drive EGAMs unstable at such low EP fractions.

Overall, the good agreement between simulations, analytical expectations, and theoretical predictions in this chapter demonstrates that the gyrokinetic code ORB5 is capable of handling experimental-like anisotropic EP distribution functions, both

analytical and numerical. In the next chapter non-linear studies, addressing these, so far neglected, effects will be presented.

5 Non-linear electromagnetic simulations of EGAMs and AWs

The study and comprehension of energetic particle (EP) dynamics and their confinement is crucial for future fusion reactors [68]. As previously declared, this thesis is a validation exercise on this path. Its ultimate goal is to predict the non-linear dynamics of EPs using experimental-like distribution functions. In the previous chapter 4 we studied the linear stability of GAMs using anisotropic distribution functions. In this Chapter we will introduce in our ORB5 simulations the non-linearities and $n = 1$ electromagnetic modes (AWs), keeping the same plasma parameters (NLED-AUG case, see section 3.2) and the newly implemented anisotropic distribution functions for the EPs (see section 3.3). This will allow us to advance in the reconstruction of the non-linear dynamics of the NLED-AUG case.

Alfvén Waves (AWs), along with EGAMs, can be excited by EPs and affect plasma confinement (see section 2.4). Unlike EGAMs, AWs can be linearly driven unstable by isotropic distribution functions with real-space gradients, the studies with these characteristics are abundant [47, 73, 119]. Nonlinear interactions between AWs and EGAMs have been observed in ASDEX-Upgrade [70], motivating the interest for the non-linear driving effect of pump AWs on EGAMs using experimental-like EP distribution functions in the NLED-AUG scenario. The ORB5 gyrokinetic code was therefore set to run such nonlinear, electromagnetic, multi-mode simulations.

To the path of predictive simulations of experimental scenarios previous, the efforts made so far are the following. In chapter 4 [50] an analytical ASD distribution function was developed, and its parameters ξ_0 and σ_ξ were varied. The growth rate of EGAMs was found to depend on the phase space shape of the distribution function. Numerical simulations using experimental-like distribution functions obtained from RABBIT showed no positive growth rates for tested cases, contradicting experimental measurements. Non-linear interactions with $n = 1$ Alfvén waves were suggested as a possible cause. The non-linear interactions between AWs and EGAMs in NLED-AUG case were already studied in reference [58]. In these simulations a double bump-on-tail distribution function was used for the EPs. As aforementioned, this case is too far from the experimental truth. In fact, this distribution function was peculiarly designed for the linear excitation of EGAMs. In order to bridge the gap between theory and

experiments, we are going to analyze the dynamics of the NLED-AUG case using the analytical and numerical experimental like distribution functions introduced in section 3.3, this time adopting a much more complete numerical physical description than those offered in Chapter 4 (see sec. 5.1 for details).

This Chapter is structured in the following way. In section 5.1 we present the numerical set up used for the ORB5 simulations. Starting from section 5.2 we present the non-linear electromagnetic simulation results for the analytical ASD EP F_0 and in section 5.3 the results with the RABBIT numerical distribution function. The non-linear coupling between higher mode number instabilities (AWs) and EGAMs is proved to be fundamental for the excitation of the latter in the experimental scenario. Finally, in section 5.4 we compare the numerical results using the realistic RABBIT distribution function with the experimental observations. In section 5.5 we draw our conclusions and outline the path for future work.

5.1 Numerical setup

Before moving to the numerical results obtained from ORB5 non-linear simulations we will briefly describe the input sheet used to run them. Once again, attempting to achieve the most experimental relevant case, we use the magnetic equilibrium (fig. 3.1), the temperature and density profiles (fig. 3.2) from NLED-AUG case (see section 3.2 for details), or shot #31213 in AUG (for the simulations using the RABBIT distribution functions from shots #31214-6, we used the profiles from those shots). The main plasma characteristics are listed in Table 3.1. The simulations included three species, ions (deuterium), electrons and EPs (fast deuterium). This time the simulation was run non-linearly. In order to retain the non-linearities for the EP dynamics it's enough to consider in the characteristic of the particles the first order non-linear corrections (as show in equations 3.7 to 3.9) only for the EP species, as specified in section 2.1 and 3.1. The non-linearities will allow the particles to redistribute in phase space. Therefore, at different time steps we will yield a distribution function different from the initial one ($F_{EP}(t) \neq F_{EP,0}$). Not considering non-linear effects for electrons and ions will have a slightly stronger damping effect on the modes, nevertheless, as said previously, this effect is not dominant with respect to the phase space effects of EP distribution. Furthermore, not considering non-linearities for bulk species allows us to run much fast simulations. This time the electrons were run kinetically, thus dropping the adiabaticity hypotesis which was possible in the linear electrostatic case (see section 4.2). The electron to ion mass ratio was set to $m_e/m_i = 0.002$, an approximation that allows for faster simulations. The fields equations were solved using both Ampere and Poisson equations 3.12 and 3.13, allowing both electrostatic $\delta\varphi$ and electromagnetic $\delta\mathbf{B}$

fluctuation to develop. The Fourier mode filter was set to consider only $n = 0$ and $n = 1$ modes, filtering out all the modes with $n > 1$. The Δm filter was set to 5. Numerical resolution parameters as the time step, the spatial grid (in s, χ, ϕ coordinates), and the number of markers used for the three species (e, i, EP) are listed in Table 5.1.

$\Delta t[\omega_{ci}^{-1}]$	N_s	N_χ	N_ϕ	$N_{p,i}$	$N_{p,e}$	$N_{p,EP}$
1	256	128	32	10^7	$4 \cdot 10^7$	$5 \cdot 10^7$

Table 5.1: Numerical simulation parameters: Δt is the time step, $N_{(s,\chi,\phi)}$ are the grid resolution, N_p the total number of markers for each species.

Provided the numerical settings that were used in the non-linear simulations, we can move forward and focus our attention on the results obtained in these simulations. We will present first the results using the analytical ASD distribution function for the EPs (section 3.3.1), and then the results using the realistic numerical RABBIT one (sec. 3.3.2).

5.2 Non-linear simulation results using ASD distribution function

In this section we will show the results from ORB5 running sets of simulations similar to those presented in section 4.3. We are interested in analyzing the effects of anisotropy of realistic distribution functions on the non-linear excitation of n=0 modes via wave-wave coupling with AWs. To this purpose we ran non-linear simulations using the analytical pitch-dependent anisotropic slowing down (ASD) F_0 for the EPs, defined as in equation 3.17 [50]. The numerical simulations were run using the equilibrium and the profiles of NLED-AUG case, shot #31213 in ASDEX Upgrade, as mentioned in the previous paragraph. We ran scans varying the preferred pitch ξ_0 and the scattering of the particles σ_ξ around that pitch.

The purpose of adopting a richer and more accurate physics, as described in the previous section 5.1, is to be able to reproduce the experiment more faithfully than it was previously done in the linear case using experimental like F_0 [50], as presented in Chapter 4, or in the non-linear case using non experimental like anisotropic distribution functions as in reference [58]. Hence, according to the analytical theory presented in section 2.5 [57, 58] we expect to yield positive $n = \{0\}$ ZS growth rate also for anisotropic EP F_0 that yield damped GAMs in the linear simulations. This is the case, for example, of the ASD F_0 with $\xi_0 = -0.9$ and $\sigma_\xi = 0.2$ (sec. 4.3.3) or of the RABBIT distribution functions (sec. 4.4). In fact, we expect the $n = \{1\}$ EPM to be excited by

the radial gradient of the off-axis peaked EP density profile, and through the non-linear wave wave coupling mechanism this should be able to drive a ZS with $\gamma_{ZS} = 2 \cdot \gamma_{AW}$ [57].

If our expectations are correct, we will be able to reproduce the experimental scenario in an unprecedented way. Enabling us to reach a very important fidelity degree for our PIC code ORB5.

In particular, in this section we will focus on the results from a particular case of the ASD F_0 ($\xi_0 = -0.9$, $\sigma_\xi = 0.2$). We will analyze the differences with the linear simulation and draw some considerations. After that, as in section 4.3.3, we will give the results from a full scan varying the parameters ξ_0 and σ_ξ. We will try to described the trends observed and give an explanation for it and the issues arising from performing and interpreting such a simulation scan. Finally, we will focus on the pitch dependency of growth rates and saturation levels. In this way, we will be ready to study the RABBIT cases which offer (only) slightly different injection angles.

5.2.1 Results using ASD F_0 with $\xi_0 = -0.9$ and $\sigma_\xi = 0.2$

For this reference case, we performed simulations either retaining only $n = \{0\}$ or $n = \{1\}$ modes, as well as both $n = \{0, 1\}$ modes coupled together in the same simulation, for a total of three simulations. This allows us to compare the growth rates of the decoupled different modes (ZS, GAM, AWs) and examine the impact of non-linear interactions on their behavior as they are coupled together. Specifically, we focus on the case where the EPs' ASD F_0 was defined with $\xi_0 = -0.9$ and $\sigma_\xi = 0.2$. This choice is not a coincidence. In fact, it's worth to remind that this case closely resembles the experimental like distribution function reconstructed by RABBIT, giving some experimental relevance to the results shown below. Furthermore, as outlined in section 4.3, this distribution function in the linear case yields a marginally stable GAM. Therefore, it will be clear if the non-linear pumping mechanism of AWs will have an effect on the non-linear drive of $n = \{0\}$ modes.

The results obtained are shown in fig. 5.1, here the different modes from three different simulations have been plotted. The plot shows the radial peak of the scalar potential signal in time of the dominant m mode from either the $n = 0$ or the $n = 1$ modes. The red line represents the AW from the only $n = 1$ simulation, the green the GAM from the only $n = 0$ one, and the blue and orange lines are respectively the ZS and the AW from the simulations were modes $n = \{0, 1\}$ were let interact with each other. These result demonstrate a significant impact of non-linear interactions with AWs on the growth rate of the zonal structure (ZS), confirming previous predictions and findings in [57, 58]. When considering only the $n = 0$ mode without retaining the AWs (green line in fig. 5.1), the GAM exhibits a marginally stable behavior, consistently with

the linear case [50] (see section 4.3). However, when both modes interact non-linearly, the ZS (blue line) is pumped by the EP non-linear response to the AW (orange line) during the linear phase, resulting in a growth rate of $\gamma_{ZS} \sim 2\gamma_{AM}$ as indicated by equation 2.95. In particular, in this case, we yield:

$$\gamma_{ZS} = 5.8 \cdot 10^{-2} \omega_A = 1.75\gamma_{AM} \simeq 2\gamma_{AM} \ , \tag{5.1}$$

with $\gamma_{AM} = 3.31 \cdot 10^{-2}\omega_A$, considering the time interval $t = [7300, 9300]\omega_{ci}^{-1}$. The growth rates are computed as described in section 4.3. The growth rate of the AW does not appear to be significantly influenced by the non-linear interaction with the ZS:

$$\gamma_{AM,n=1} \simeq \gamma_{AM,n=0,1} \ . \tag{5.2}$$

The frequency of the damped GAM in the only $n = 0$ simulation is $\omega_{GAM} = 0.03\omega_A$. On the other hand, the AW alone has a frequency of $\omega_{AW} = 0.078\omega_A$. The frequencies of the modes in the simulation including both EGAM and AM are similar: $\omega_{ZS,n=0,1} = 0.082, \omega_A \simeq \omega_{AW} = 0.076, \omega_A$. This frequency corresponds to approximately 65 kHz, which is in reasonable agreement with the measured GAM frequencies in the NLED-AUG case (green lines near 50 kHz in fig. 5.13). This finite frequency of the ZS makes it a EGAM rather than a zero frequency zonal flow (ZFZF), which, as self evident from the name, is a zero frequency (non fluctuating) $n = 0$ mode due to the radial redistribution of EPs.

In non-linear simulations it is of interest analyzing the saturation levels too. These are the amplitude levels at which the modes turn from an exponential to a purely oscillatory steady state behaviour. The saturation levels are very similar for the $n = \{1\}$ and the $n = \{0,1\}$ Alfvèn waves: in ORB5 normalized units $SAT_{AW,n=\{1\}} \simeq 6.3$ and $SAT_{AW,n=\{0,1\}} \simeq 1.15$. The saturation level for the ZS in the $n = \{0,1\}$ case is slightly lower than the Alfvèn wave one in the same simulation: $SAT_{ZS,n=\{0,1\}} \simeq 1.5$. Furthermore, we notice that there is a second linear phase for the growing modes in fig. 5.1. This seems to be rather a numerical instability which, anyhow, does not affect the parts we are interested in: the first growing phase and the first saturation phase.
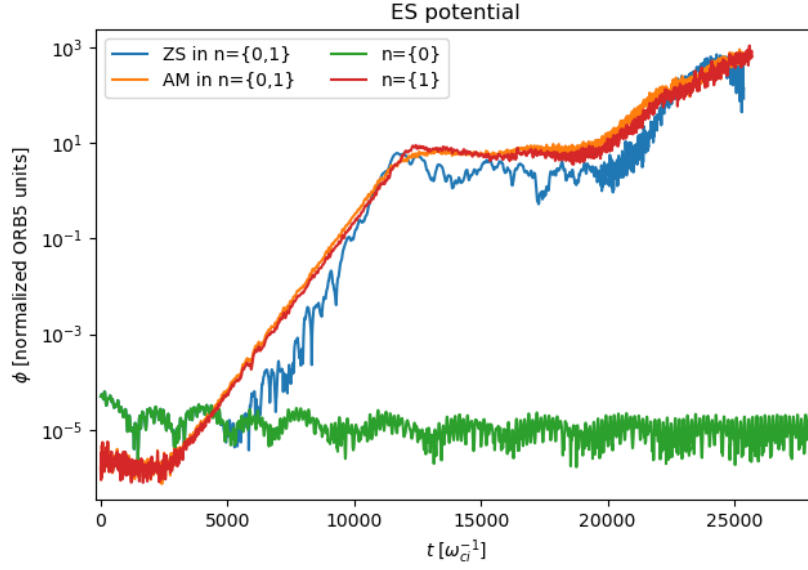
Figure 5.1: Modification of ZS growth rate in presence of AMs, the plot shows the radial peak of the amplitude of the dominant m mode for each of the $n = \{0\}, \{1\}, \{0, 1\}$ modes in time. These simulations used the ASD F_0 with $\xi_0 = -0.9$ and $\sigma_\xi = 0.2$

It is interesting noting the radial structures of the two interacting modes. Similarly to references [58, 62], the dominant AW mode exhibits a $(m, n) = (2, 1)$ structure located in the core region around $s \simeq 0.25$ (fig. 5.2, left panel), where the EP density profile exhibits the highest positive gradient (fig. 3.2). Similarly, the $(m, n) = (0, 0)$ GAM shows the highest electric field $(\partial \varphi / \partial r)$ in a region outside the core region around $s \simeq 0.2$ (fig. 5.2, right panel). This highlights the interplay between the AW and the EGAM.
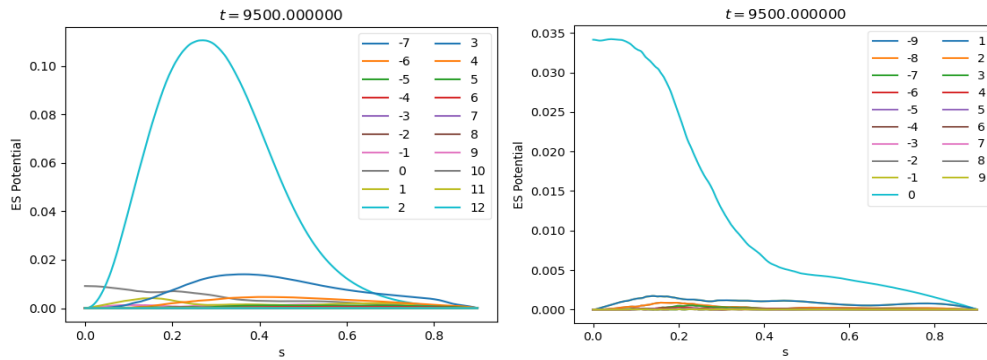
Figure 5.2: Radial profiles for $n = \{1\}$ AM (left) and $n = \{0\}$ ZS mode (right) m-modes in the linear phase of the multi-mode $n = \{0, 1\}$ simulation with $\xi_0 = -0.9$ and $\sigma_\xi = 0.2$ at $t = 9500 \, \omega_{ci}^{-1}$

Morover, the nature of the AW can be analyzed by overlaying the LIGKA Alfvén continuum [121] on top of the simulation spectrogram (fig. 5.3). We can see that the mode is located at its radial peak ($s \sim 0.25$) at a frequency very close to the Alfvén continuum (red lines in fig. 5.3). This hints that the AM, during the linear phase, is actually an energetic particle mode (EPM) in the BAE (beta-induced) gap. Note that the mode does not peak at or close the BAE continuum minimum at s=0.47, but further inside at s=0.25. Thus the mode properties are mainly determined by the radial EP gradient, justifying the identification as an EPM.

After the saturation, the frequency of the Alfvén mode increases to $\omega_{AW,NL} = 0.12\omega_A$. This suggests that even experimental distribution functions can capture frequency chirping phenomena observed in the NLED-AUG case [73]. However, this phenomenon will not be extensively analyzed in this thesis, it will be investigated in future studies.
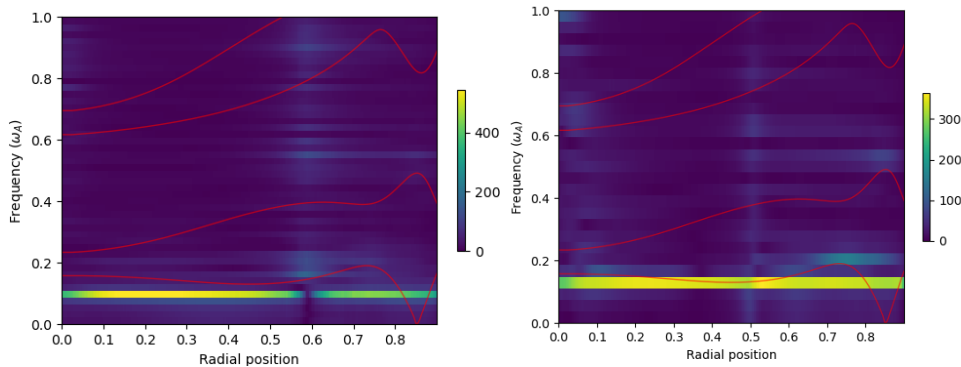
Figure 5.3: Frequency spectrogram of the AW in the linear (left) and non-linear (right) phases of the simulation with $n = \{0, 1\}$ modes, LIGKA Alfvén continuum [121] for $n = \{1\}$ mode in AUG shot #31213 is superimposed with red lines to the spectrogram

When comparing the single simulations either the $n = 0$ or the $n = 1$ mode ran independently from one another, it is evident that the non-linear coupling between the ZS and the AW has a minimal impact on the structure of the AW. In fact, the electrostatic potential level of the AW remains nearly unchanged in both the $n = \{0, 1\}$ simulation (fig. 5.2 left) and the $n = \{1\}$ simulation (fig. 5.4 left). However, in the $n = \{0\}$ simulation (fig. 5.4 right), the mode transforms from a damped GAM to a non-linearly excited ZS or EGAM (given the finite frequency) in the $n = \{0, 1\}$ simulation (fig. 5.2 right). We notice that the damped $(m, n) = (0, 0)$ GAM survives closer to the edge. In fact, as mentioned in sec. 2.3, the damping is proportional to $exp(-q(r)^2)$ so it will be mostly damped in the core as we see from the figure. Furthermore, we notice that a strong $m = 1$ mode is of a magnitude comparable to the $m = 0$ GAM. A thorough analysis of this mode goes beyond the aim of this work, however it may be a global Alfvén Eigenmode (GAE) which is marginally stable. We

do not exclude the possibility that it is also a marginally stable numerical instability. In both cases, this mode does not affect the physical results highlighted above.
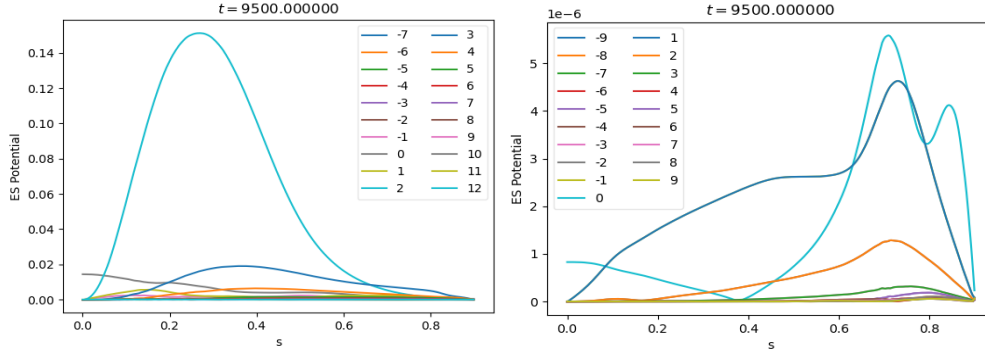

Figure 5.4: Radial profiles for $n = \{1\}$ AM (left) and $n = \{0\}$ GAM mode (right) m-modes in the linear phase of the decoupled $n = \{0\}$ and $n = \{1\}$ simulations with $\xi_0 = -0.9$ and $\sigma_\xi = 0.2$ at $t = 9500 \, \omega_{ci}^{-1}$

These results are extremely relevant for our research. In fact, we proved that through non-linear interactions we can excite also EGAMs where the linear drive of EP was not enough to destabilize them linearly (sec. 4.3). The hypothesis drawn at the end of Chapter 4 is correct, as we now see, the mismatch previously observed with experimental measurements is due to an incomplete physical description in our model (sec 4.5). Furthermore these results from the ASD F_0, suggest that also using experimental-like numerical F_0 we will be able to better reproduce the experimental finding, see section 5.3 for details.

In the next section we will perform a scan varying the two ASD F_0 parameters (ξ_0 and σ_ξ), similarly to what done in section 4.3.3. Our purpose for the next two sections is to study how the phase space, and the pitch of the ASD distribution function, influences the growth rates and the non-linear dynamics of AWs and ZS.

5.2.2 Simulation scan of ASD with varying ξ_0 and σ_ξ

In this section we want to study the effects of the two ASD parameters on the characteristic of AW and ZS modes in non-linear ORB5 simulations. In figure 5.5, the growth rates of $n = 0$ modes in the linear phase of non-linear simulations, where both $n = 0$ and $n = 1$ were retained, are shown as a function of ξ_0 and σ_ξ. Similarly the growth rates of GAMs with linear single mode simulations were shown in section 4.3.3. A notable difference from the linear results, where only the $n = 0$ modes were retained (figure 4.5), is that all modes in the non-linear simulations exhibit $\gamma_{ZS} > 0$, whereas in the linear case there were many cases of modes with $\gamma_{ZS} < 0$ (Chapter 4). This

positive growth rate is a result of the non-linear wave-wave coupling with the Alfv'en waves, as explained in section 2.5. In fact, in all these cases also AWs are excited.

In the region with $\xi_0 \sim 1$ (left part of the plane in figure 5.5), the growth rates of the ZS modes are primarily influenced by the growth rates of the AW modes. This happens because the Alfvén modes are particularly excited by deeply passing EPs. This condition is met for low pitch angles relative to the magnetic field (values of the parallel velocity close to $\xi_0 \sim -1$). As in the case of the simulations shown in fig. 5.1, for all the simulation with high values of ξ_0 the AW is more unstable than the $n = 0$ mode. As a result, the non-linear wave-wave coupling leads to the excitation of ZS modes through the interaction with pump TAEs, with $\gamma_{ZS} \sim 2\gamma_{AM}$ [57].

For low ξ_0 values, even though the AWs are weakly excited, the ZS modes can still become unstable through wave-wave coupling. Instead, for low values of both σ_ξ and ξ_0, we observe cases where the EGAMs are more unstable than the AW modes, as depicted in fig. 5.5. These cases correspond to the conditions where the linear drive of EGAMs is most unstable [50] (as shown in the previous chapter in fig. 4.5). In these scenarios, the EGAM modes retain their growth rates, while it is the AM mode that becomes more unstable due to the influence of the EGAM mode.

It should be noted by the reader that caution is required when interpreting the simulation results for values of ξ_0 close to 0. Numerical errors may arise due to a singularity in the computation of gradients near $v_{\parallel} \sim 0$ for the anisotropic asymmetric EP distribution functions. Consequently, the results in these cases may not be entirely reliable. Specifically, in the bottom right area of the plot where ξ_0 and σ_ξ are close to 0, the effective growth rate (γ_{ZS}) could potentially be lower than what is displayed in figure 5.5. Furthermore, it is important to note that such low values of pitch physically correspond to a configuration where an NBI is directed radially with respect to the plasma ($\xi_0 \sim 0 \implies v_{EP} \simeq v_{\perp}$). This experimental configuration is unfeasible for structural, ionization and plasma-deposit problems. The consequences are two folded: firstly, we are actually simulating an unusual plasma configuration, whose effects could involve instabilities not considered in this thesis, which would deserve their own dedicated studies. Secondly, since there is no physical experimental configuration corresponding to such low pitches, we cannot directly compare these results with experimental cases, unlike the comparison possible for high pitches (as explained in section 3.3.1).
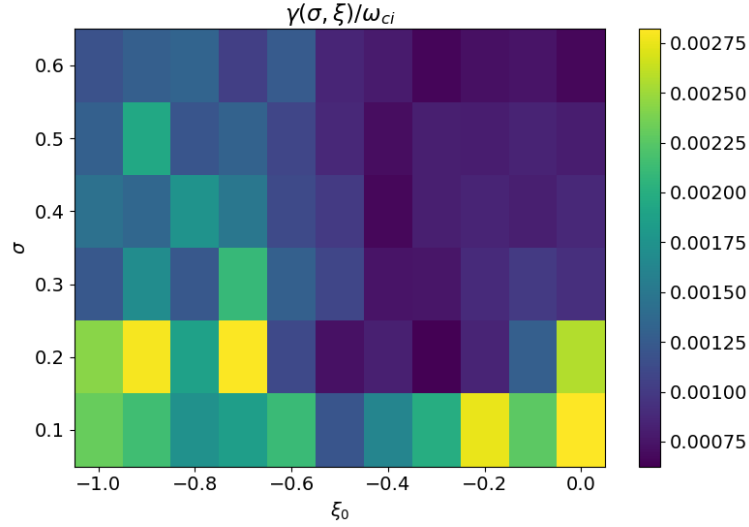
Figure 5.5: Growth rate (γ/ω_{ci}) scan in ξ_0 and σ_ξ of $n = \{0\}$ modes in growing phases of $n = \{0, 1\}$ simulations

Summarizing, the dependency of the non-linearly driven ZS on the phase space is of much more difficult interpretation than the linear excitation mechanisms explained in Chapter 4 (section 4.3.3). In fact, in this section we saw that the growth rate is mostly dominated by the AW dynamics due to the non-linear interactions between the modes, but there are cases where this is not true: for example for those EGAMs that present a linear growth rate equal or higher than the linear growth rate of the AWs. Unlike the linear electrostatic case, we don't have a tool to evaluate the exchange of power that happens non-linearly between the modes, therefore it is even harder to determine which are the driving mechanism that generate the trends we observed in figure 5.5.

5.2.3 Dependency of ZS growth rate and saturation level on the pitch angle

In this section, we explore the growth rates and saturation level trends of AWs and ZS through non-linear simulations, and we compare among them the different results. We investigate three cases of scans: simulations that include only $n = \{0\}$ modes, simulations that include only $n = \{1\}$ modes, and simulations that include both $n = \{0, 1\}$ modes. These simulations make use of an anisotropic slowing-down (ASD) EP distribution function, with a fixed parameter of $\sigma_\xi = 0.2$ while varying ξ_0 from its minimum value of -1 to its maximum value of 0, see section 3.3.1 for details. The results hereby obtained provide an important insights into the observed phenomena and outlined in the previous section 5.2.2.

If we observe the growth rate trend in the $n = \{0\}$ simulations (represented by blue crosses in figure 5.6), we observe a similarity to the linear results obtained in section 4.3.2 [50], in particular in figures 4.3, 4.4 and 4.5. Notably, the highest growth rates are yielded around $\xi_0 \sim -0.4$, while for $\xi_0 \sim 0; -1$, the growth rates are negative. In these latter cases, the EPs are unable to resonate with the characteristic velocity of the GAM, which is approximately $v_{th,i}$ (for details refer to section 2.3). This lack of resonance is due to the particles being either trapped ($\xi_0 = 0$) or deeply passing ($\xi_0 = -1$) (sections 2.3, 4.3.2). This highlights once again that the decoupled physics of the $n = \{0\}$ modes is unable to reproduce the experimental findings, which, as we will state in section 5.4, can be matched only by non-linear multi-mode simulations. On the other hand, the growth rates of AWs in the only $n = \{1\}$ simulations (represented by red crosses in figure 5.6) are consistently positive for all the pitches. In fact, as we know from theory (section 2.4), AWs can be driven both by gradients in phase-space as well as in real space.

When we examine the radial structure, we observe that values of $\xi_0 \geq -0.4$ lead to the excitation of an $n = 1$ mode, which corresponds to a TAE. Conversely, values of $\xi_0 \leq -0.4$ result in the excitation of an Energetic Particle Mode (EPM). Notably, the growth rates of EPMs tend to be higher, the closer proximity of ξ_0 to -1 results in higher growth rates (as shown in figure 5.6). This is due to the fact that deeply passing particles resonate more effectively with the Alfvén velocity : for $\xi_0 = -1$, we yield:

$$v_{EP,th,\parallel} \sim 3 \cdot 10^6 \frac{m}{s} \lesssim v_A \sim 8.3 \cdot 10^6 \frac{m}{s} \ . \tag{5.3}$$

Furthermore, analyzing the simulations with both modes $n = \{0, 1\}$, we observe that the growth rates of AWs (represented by red dots in fig. 5.6) exhibit minimal differences compared to the $n = \{1\}$ simulations (red crosses). In fact, red crosses and red dots are barely distinguishable in figure 5.6. Nevertheless, ZS growth rates are significantly affected, particularly in cases where the growth rate of $n = \{0\}$ mode was considerably lower than that of the AWs. We note that for $\xi_0 \geq -0.6$, the growth rates of the non-linearly excited ZS approach the growth rate of the AWs. We remind again that such low values of ξ_0 can generate the numerical and physical problems addressed in section 5.2.2. Conversely, for $\xi_0 \leq -0.6$, starting from a certain threshold value of the AW growth rate, the γ_{ZS} begins to align with the trend predicted by Qiu et al. in [57]. In particular, in fig. 5.6, we observe that the blue dots ($\gamma_{ZS,n=0,1}$) start to approach the dashed black line representing Qiu's prediction for non-linearly driven ZS by EPM-dominated pump AWs [57]: $\gamma_{ZS,n=0,1} \sim 2 \cdot \gamma_{AW,n=0,1}$.
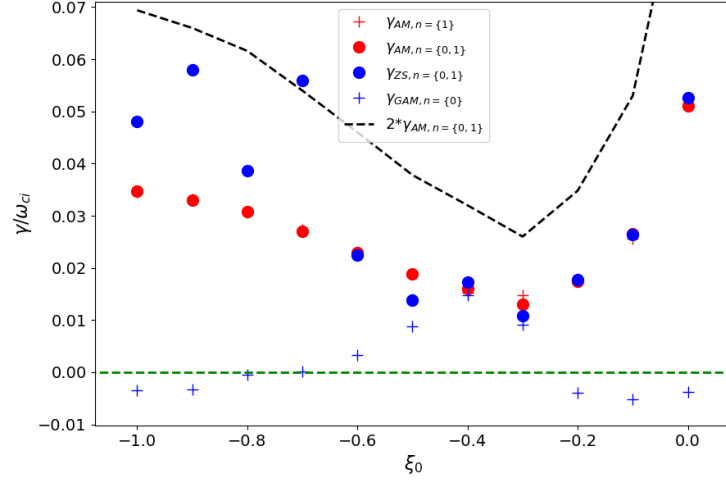
Figure 5.6: Growth rate trends of ZS and AW modes in $n = \{0\}, \{1\}, \{0, 1\}$ simulations, with ASD F_0 with $\sigma_\xi = 0.2$ and varying ξ_0

The interpretation of these results as said in the previous section can be challenging. For this case, we can split the ξ_0 domain in 3 areas with different dynamics. For values $-1 \geq \xi_0 \geq -0.6$, we observe that the ZS dynamics is dominated by the non-linear interactions with AWs (EPMs), with growth rates for the ZS well aligned with the theoretical predictions from Qiu et al. according to formula 2.95 (dashed black line in fig. 5.6). For $-0.6 \geq \xi_0 \geq -0.3$, the growth rates of linearly driven EGAMs are comparable with those of AWs, therefore the non-linear interactions are not dominated by AWs anymore. For $-0.2 \geq \xi_0 \geq 0.0$, we incur in too many physical and numerical problems to accurately determine the nature of the EP driven modes in such conditions. Dedicated studies are needed to understand the feasibility of such simulations. We can now move to the study of the saturation level dependency on ξ_0

The saturation levels, their modification through non-linear mode coupling and their dependency on ξ_0 are shown in figure 5.7. The saturation level has been determined localizing the point in the simulation where the mode deviates from its exponential behavior. Overall, we observe that the difference in saturation levels between the $n = \{0\}$ AW (red crosses in figure 5.7) or $n = \{1\}$ ZS modes (blue crosses) and their $n = \{0, 1\}$ (respectively blue and red dots) counterparts is consistently less than a factor of 10. This suggests that non-linear interactions have a small impact on the saturation level change. Of course, it is worth noting that the non-linearly excited ZS modes exhibit saturation levels different from the zero value of the damped modes.

We can observe a dependency of these levels on ξ_0, which seems to affect primarily the AW saturation levels and, consequently, the non-linearly excited ZS levels. Specifically,

for $\xi_0 \geq -0.4$, the saturation levels are generally more than one order of magnitude higher compared to $\xi_0 < -0.4$ cases. This can be caused by the dominance of TAEs in the former case, allowing the AWs to reach higher saturation levels. Nevertheless, we remind once again that these cases may be overly excited for unforeseen numerical and physical instabilities (see section 5.2.2). On the other hand, simulations with $\xi_0 < -0.4$, which are predominantly governed by EPMs in the linear phase, achieve saturation at lower levels.
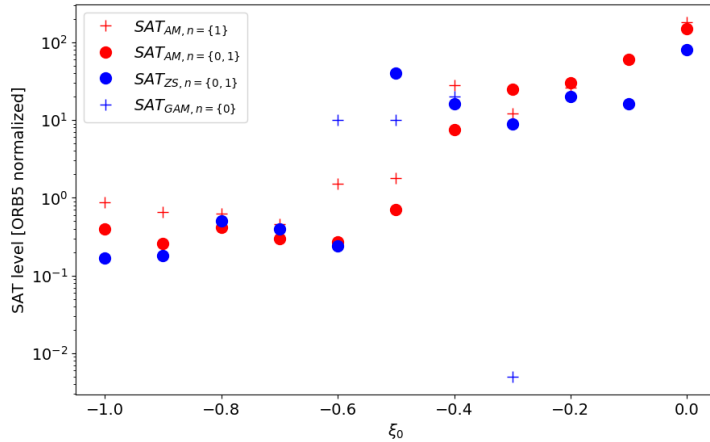

Figure 5.7: Saturation level trends of ZS and AW modes in $n = \{0\}, \{1\}, \{0, 1\}$ simulations, with ASD F_0 with $\sigma_\xi = 0.2$ and varying ξ_0

In this section we studied the effects of non-linear interactions with AWs on the dynamics of ZS and EGAMs in $n = \{0, 1\}$ mode simulations on NLED-AUG case, varying the analytical ASD distribution function over the parameter space determined by ξ_0 and σ_ξ. We have seen a completely different behavior of the ZS growth rate with respect to ξ_0 and σ_ξ if compared to the behavior yielded in the linear simulations. Furthermore, the interpretation of it is very complex. Nevertheless, according to the pitch we identified three areas, one dominated by the AW dynamics at high ξ_0, one where EGAMs and AWs interact with each other but where none prevails on the other one, and one for $\xi_0 \sim 0$ which may hide numerical instabilities and phenomena which go beyond the aim of this thesis. Finally, we performed a similar analysis for the saturation levels of the different modes.

Enriched by the observations obtained from simulations employing the analytical ASD distribution function for EPs, we are now ready to test this advanced physical model with the most experimental-relevant EP distribution function, that obtained from RABBIT.

5.3 Non-linear simulation results using RABBIT distribution functions

We previously showed the results from non-linear electromagnetic NLED-AUG case simulations using the ASD F_0. The growth rate was found to be dependent on ξ_0 according to the superimposition of different physical effects (see section 5.2 for details). In this section we will use the more realistic RABBIT distribution functions [50, 140, 141]. Feeding them as input in ORB5 NLED-AUG case non-linear simulations, we will obtain the most experimental relevant scenario simulated in the whole thesis. Our hopes are to be able to reproduce the non-linear EP dynamics observed in the experimental measurements (fig. 5.13).

As before, we can rely only on the little changes in pitch of the NLED-AUG case RABBIT distribution functions to appreciate the differences in growth rate that this experimental change in phase space produces. The NBI injection angle, in fact, varied from 6.05° in shot #31214 to 7.15° in shot #31213 (in shots #31215-6 it was 6.65°), see figure 4.13.
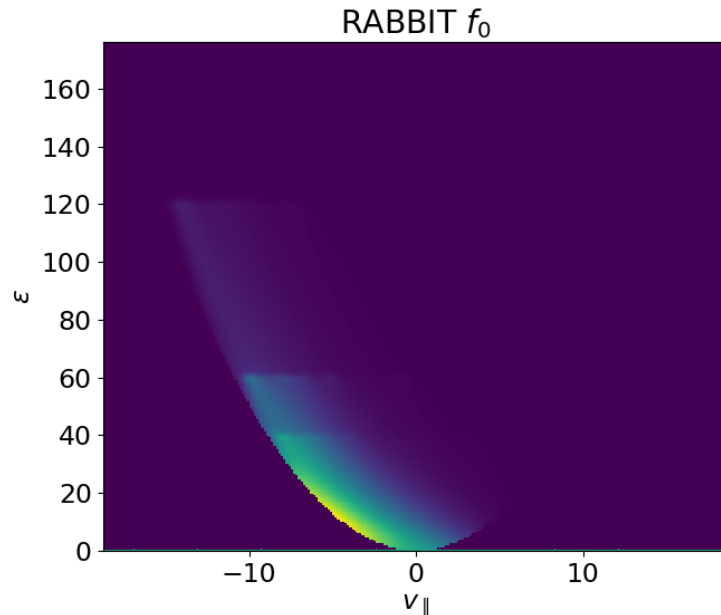

Figure 5.8: EP F_0 for AUG shot #31213 obtained from the Fokker-Planck solver code RABBIT [140]

5.3.1 Non-linear simulations of shot #31213 in AUG

We ran additional non-linear simulations, using the equilibrium, profiles, and plasma parameters of NLED-AUG case shot #31213 (described in sections 3.2 and 3.3.2). This time, we used the RABBIT F_0 as the input EP distribution function and performed the simulations with the retention of either only $n = \{0\}$, $n = \{1\}$, or both modes. The obtained results are presented in figure 5.9.

We yielded results very close to the case shown before for the analytical ASD with $\xi_0 = -0.9$ and $\sigma_\xi = 0.2$, as we can observe from a comparison of plots show in figure 5.9 and figure 5.1. The case where only the $n = \{0\}$ mode was retained yields a marginally stable GAM (green line in fig. 5.9) with a growth rate:

$$\gamma_{GAM,n=\{0\}} = -3.8 \cdot 10^{-3} \omega_A \ , \tag{5.4}$$

consistent with the results yielded in the linear case for the same distribution function (section 4.4). From the simulation where only the $n = \{1\}$ modes were retained, the AW has instead a positive growth rate (red line in fig. 5.9):

$$\gamma_{AM,n=\{1\}} = 1.9 \cdot 10^{-2} \omega_A \ . \tag{5.5}$$

Such growth rate is maintained almost identically in the case where both modes $n = \{0, 1\}$ were considered (orange line in fig. 5.9):

$$\gamma_{AM,n=\{1\}} \simeq \gamma_{AM,n=\{0,1\}} \cdot \tag{5.6}$$

In the simulation with non-linear interactions with $n = \{0, 1\}$ modes, the ZS mode (blue line) is driven unstable via non-linear wave-wave coupling by the growing AM. The growth rate of such mode is measured to be:

$$\gamma_{ZS}^{NL} = 2.9 \cdot 10^{-2} \omega_A = 1.52 \gamma_{AM} \simeq 2 \gamma_{AM} \ , \tag{5.7}$$

as foreseen by theory [57, 58]. This result has been obtained in particular for the time interval $t \simeq [17 \cdot 10^3, 19 \cdot 10^3] \omega_{ci}^{-1}$.

If we analyze the saturation levels we will find that it is almost the same for the AW in both $n = \{0\}$ and $n = \{0, 1\}$ simulations:

$$SAT_{AW,n=\{1\}} = SAT_{AW,n=\{0,1\}} = 0.36 \ , \tag{5.8}$$

in ORB5 normalized units. Whereas, the saturation level for the non-linearly driven ZS in the $n = \{0, 1\}$ simulation is almost the same as the AW one: $SAT_{ZS,n=\{0,1\}} = 0.27$.
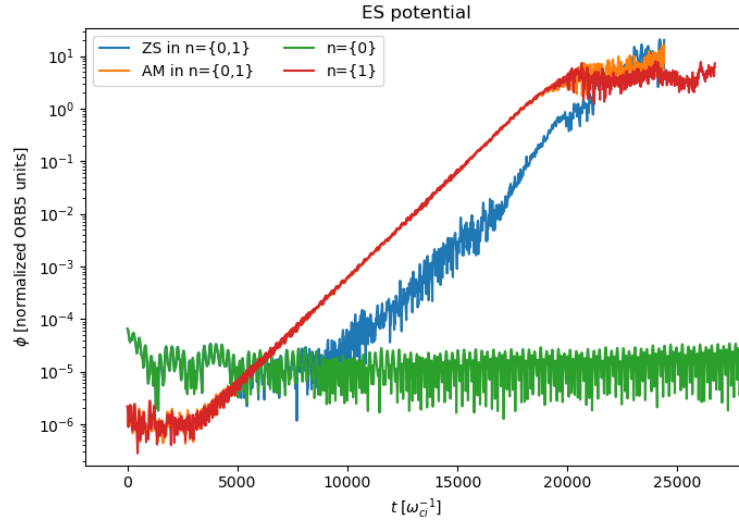
Figure 5.9: Modification of ZS growth rate in presence of AMs, the plot shows the radial peak of the amplitude of the dominant m mode for each of the $n = \{0\}, \{1\}, \{0,1\}$ modes in time. These simulations used the RABBIT F_0 from AUG shot #31213

The results shown in fig. 5.9 provide strong evidence that non-linear electromagnetic ORB5 simulations with experimental-like distribution functions can successfully reconstruct the EP non-linear dynamics in an experimental scenario as NLED-AUG case. This is proved by the good qualitative agreement between the simulation results and the experimental measurements. As in this example, for NLED-AUG case #31213, as shown in figure 5.13, an excited $n = \{0\}$ mode was observed using magnetic probe coils. As described in section 4.4, linear numerical simulations using experimental-like EP F_0 were unable to reproduce this result [50]. The successful numerical reproduction of the non-linear EP dynamics through these simulations highlights the capability of ORB5 to simulate complex non-linear behavior of EPs in experimental configurations, paving the way to the possibility of simulation global burning plasmas scenarios.

In the next section we will run the same simulation setup shown in this section but this time we will use the other RABBIT distribution functions, namely those from NLED-AUG shots #31214-6. We will analyze the dependency of the growth rates and the saturation levels of the modes on the NBI injection angle (section 5.3.2) and then compare them to the experimental observations (section 5.4).

5.3.2 NLED-AUG case simulations of shots #31213-6

Non-linear, electromagnetic simulations were run, retaining either $n = \{0\}$, $n = \{1\}$, or both $n = \{0,1\}$ modes. These simulations used the experimental density and temperature profiles, as presented in sections 3.2 and 3.3.2, and incorporated the

experimental-like EP distribution functions obtained from RABBIT for the aforementioned shots. The simulations were conducted for all four NLED-AUG cases, specifically shots #31213-6 [70], which correspond to experimental measurements shown in figure 5.13.

The simulation results for the four NLED-AUG shots #31213-6 are displayed in the following figures. Figure 5.10 shows the time evolution of the $n = \{0\}$ ZS modes from the $n = \{0, 1\}$ simulations. The growth rate trends for both ZS and AWs are plotted in figure 5.11, while figure 5.12 shows the saturation level trends for these modes. The simulations were run retaining either $n = \{0\}$, $n = \{1\}$, or both $n = \{0, 1\}$ modes, in order to be able to compare the non-linear effects on the modes.
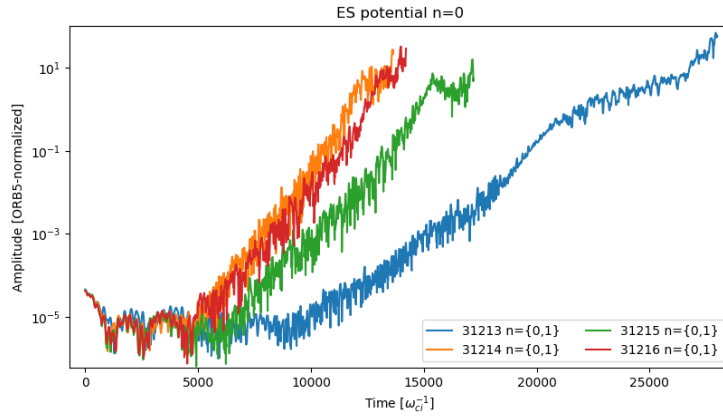

Figure 5.10: Signals of the radial peak of the $(m, n) = (0, 0)$ ZS modes in time from simulations retaining both $n = \{0, 1\}$ modes for the four different NLED-AUG cases (shots #31213-6 in AUG)

Figure 5.10 shows that the ZS modes are excited for all the four NLED-AUG shots. It is worthy to note that the electrostatic linear simulations in section 4.4 were unable to reproduce this result. This fact points out the importance of non-linear interactions with the pump TAE in driving the ZS modes unstable.

As a matter of fact, figure 5.11 shows that the growth rates of non-linear simulations with only $n = \{0\}$ modes are negative (blue crosses in fig. 5.11), the same result we yielded for the linear RABBIT simulations basically (see section 4.4 for details). Nevertheless, in simulations where both modes were retained, we observe that GAMs are initially damped and it is only in a second phase, when the AWs overtake the $n = \{0\}$ modes in magnitude, that they begin to grow, triggered by non-linear wave-wave coupling as described by Qiu in [57].

From figure 5.10 we observe that the non-linear coupling reaches full effect after some time in the coupled-physics phase (for example between $t = 18500\omega_{ci}^{-1}$ and

$t = 21000\omega_{ci}^{-1}$ for simulation of shot #31213), here the ZS has a growth rate double with respect to the growth rates of the pump-TAE, as it is clarly shown in figure 5.11. This results aligns very well with theoretical prediction explained in section 2.5 and summarized in equation 2.95 [57].

Moreover, from both plots 5.10 and 5.11, we can note that the ZS growth rate is maximum for the most on-axis case, shot #31214, where the NBI had an angle of 6.05° relative to the magnetic axis. As the NBI angle increases towards the most off-axis case, namely shot #31213, the growth rate of ZS decreases. This behavior is attributed to the physics of Alfvén Waves, which are driven by deeply passing energetic particles. In fact, we observed the same phenomenon in the simulations with the analytical ASD EP distribution function. In that case (section 5.2), we could explicitly test this dependency of AW and ZS growth rate on the pitch and it was found an increasing behavior as the pitch increases. Therefore, when the NBI angle is closer to the magnetic axis, the Alfvén waves are more strongly driven. This trend is clearly depicted by the behavior of $\gamma_{AM,n=\{1\}}$ (red dots) in figure 5.11. Finally, as initially observed, this stability feature of AWs has an important impact on the growth rates trends of non-linearly driven ZS. As depicted in figure 5.11, the non-linearly driven EGAMs align with the theoretical expectations by Qiu et al. [57] (dashed black line), which are determined by the AW trends, thus explaining the trend of the growth rated of $n = \{0\}$ modes as depicted in figures 5.10 and 5.11.

As we already found out in section 5.2.3, in such multi-mode configurations the non-linear coupled dynamics is dominated by the AWs' one. Therefore the growth rate trend of the ZS (blue dots in figure 5.11) follows the same pattern of the AWs (the dashed black line in the figure represents the estimated growth rate of non-linearly coupled ZS according to Qiu's formula: $\gamma_{ZS}^{NL} = 2 \cdot \gamma_{AW}$ [57]).
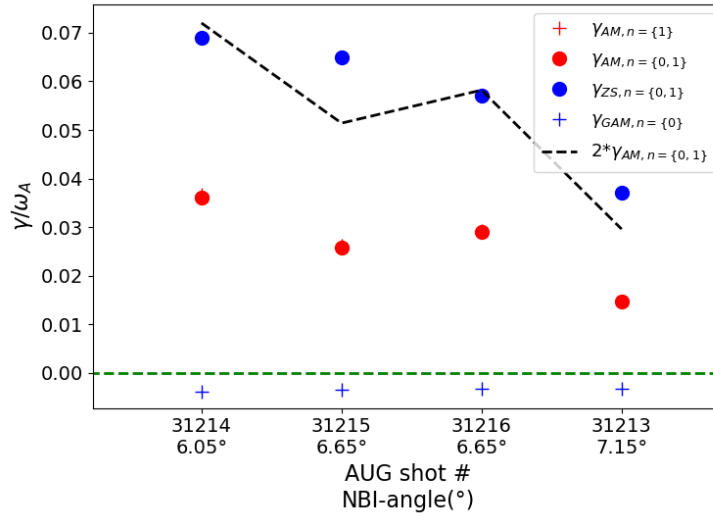
Figure 5.11: Growth rate trends of ZS and AW modes in $n = \{0\}, \{1\}, \{0, 1\}$ simulations, with RABBIT F_0 from NLED-AUG cases #31213-6

Figure 5.12 presents the saturation levels of all the modes in different cases. We notice a similar trend as the one described earlier, where the higher saturation levels are achieved in the most on-axis cases. Self evidently, the damped $n = \{0\}$ GAM modes, which have null saturation levels, become unstable in multi-mode $n = \{0, 1\}$ simulations, reaching saturation levels close to those of the AWs. To explain this trend of the saturation levels with respect to the NBI injection angle we may refer to the same explanations offered above and valid also for the analytical ASD distribution function case in section 5.2.3.
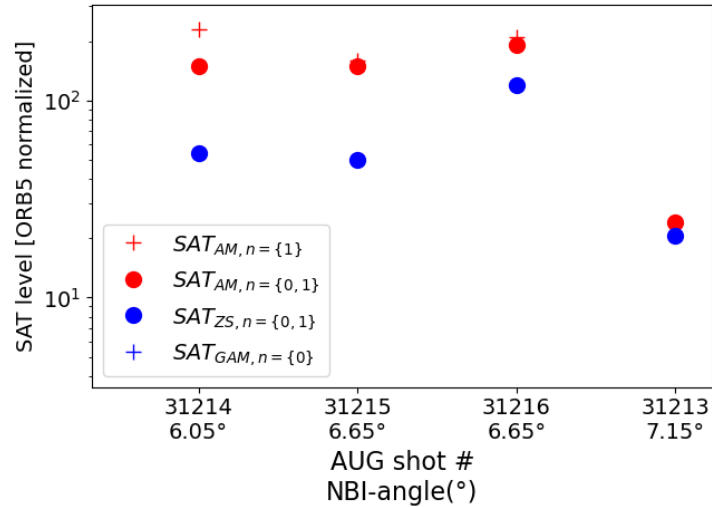
Figure 5.12: Saturation level (in ORB5 normalized units) trends of ZS and AW modes in $n = \{0\}, \{1\}, \{0, 1\}$ simulations, with RABBIT F_0 from NLED-AUG cases #31213-6

5.4 Comparison with experimental measurements

The aim of this study is to demonstrate that the gyrokinetic code ORB5 is capable of reproducing the non-linear dynamics of EPs in realistic experimental configurations, such as those observed in ASDEX-Upgrade. This is an important validation test for ORB5 to simulate realistic anisotropic distribution functions, a crucial step on the path to global predictive simulation of burning plasmas [68]. As discussed at the beginning of this chapter, previous linear electrostatic simulations [50] (see Chapter 4) could not yield the observed growth rates in the NLED-AUG case. However, it was shown that there is a correlation between the growth rate and the phase-space shape in realistic geometries [50] (Chapter 4).

In section 5.2 we demonstrated that the non-linear coupling between $n = \{0\}$ and $n = \{1\}$ modes can induce the excitation of ZS, which would otherwise remain stable (see section 4.3), by utilizing experimental-like analytical EP F_0. After that, in section 5.3, we employed experimental-like numerical EP F_0 distributions obtained from the code RABBIT to reconstruct the most experimental numerical cases, comparable to the measurements of NLED-AUG case shown below. The measurements obtained from Mirnov (pick-up) coils for the four shots of the NLED-AUG case (shots #31213-6 in ASDEX-Upgrade [70]) are shown in figure 5.13.

The Mirnov coil measurements provide an important insights into the growth rates behavior of $n = \{0\}$ modes in all the NLED-AUG shots. The green lines in the plots of

figure 5.13 at approximately 50 kHz represent the unstable $n = \{0\}$ ZS (EGAMs) which exhibit positive growth rates in all the modes. Even though, they display different values of ω and saturation levels (characteristic of the drive intensity), according to the different injection angles, the general instability of these modes is evident. Moreover, a clear dependence of the drive, hence of the growth rate and the saturation level, on the injection angle of the NBI can be observed. In the NLED-AUG case, as discussed in section 3.3.2 and above, the four shots varied in terms of the NBI angle relative to the magnetic axis. Shot 31213 had the most off-axis angle of 7.15° (top-left plot in fig. 5.13), while shot 31214 had the most on-axis angle of 6.05° (bottom-left plot). Shots 31215-6 had a mid-range angle of 6.65° (top-right and bottom-right plots). The plots of figure 5.13 clearly illustrate that the ZS mode becomes stronger as the NBI angle increases, in this behavior we noticed an alignment with the theoretical expectations of linear GAM drive obtained in chapter 4, even though linear physics wasn't able to reproduce the qualitative behavior we yield from non-linear simulations.

However, despite using experimental temperature and density profiles along with experimental-like numerical EP F_0, we did not achieve this quantitative agreement with the experimental results in our multi-mode, non-linear, electromagnetic simulations. As shown in section 5.3, the trend with respect to the injection angle observed in the simulations was contrary to the experimental findings. The dominant driving mechanism for ZS in the multi-mode simulations was the non-linear coupling with AW (see section 5.3), which is stronger for mainly on-axis beams, as discussed earlier. This mismatch between the simulations and experimental measurements arises because the linear driving mechanism, which was found to be stronger for more off-axis beams [50] (see Chapter 4), is not dominant in the non-linear simulations. Hence, a synthesis of these two driving mechanisms that aligns with the experimental observations was not achieved.

As for the linear case (section 4.4.4), a number of aspects may account for this quantitative difference with the experimental measurements.

Firstly, the reconstruction of the experimental-like EP F_0 for the NLED-AUG case using RABBIT posed certain difficulties and limitations. The representation of F_0 on the phase-space grid provided by RABBIT was not perfectly smooth, particularly in the $v_{\parallel}$ direction. This could have introduced inaccuracies in the representation of the distribution function.

Furthermore, there may be inherent uncertainties in the measurements of temperature, density, and safety factor profiles. For instance, the temperature profile was measured only in the last shot of NLED-AUG case, #31216, using an NBI blip. The profiles for the other shots were inferred from this measurement and other plasma parameters.

Additionally, the steepness of the q profile in the outer radial domain ($s > 0.9$) introduces challenges when representing its gradients in that area. This can potentially

result in numerical errors and instabilities for the modes hereby studied, particularly in areas of the magnetic equilibrium with such steep q profiles.

Finally, non-linear simulations are very sensitive to gradients in parallel velocity: $\partial F_0/\partial v_\parallel$. The combination of this sensitivity with the inaccuracies in RABBIT's representations of the experimental-like F_0 in the $v_\parallel$ direction can account for the quantitative discrepancies between the simulations and the experimental measurements.

We are confident that by improving the accuracy of the numerical description of the experiment, including more precise parameters, profiles and better representations of the experimental F_0, we can enhance the quantitative agreement with the experimental observations. Hopefully, such accuracy will be achieved in future studies using the numerical tools developed so far in the present work and in the context of the gyrokinetic code ORB5 [147].
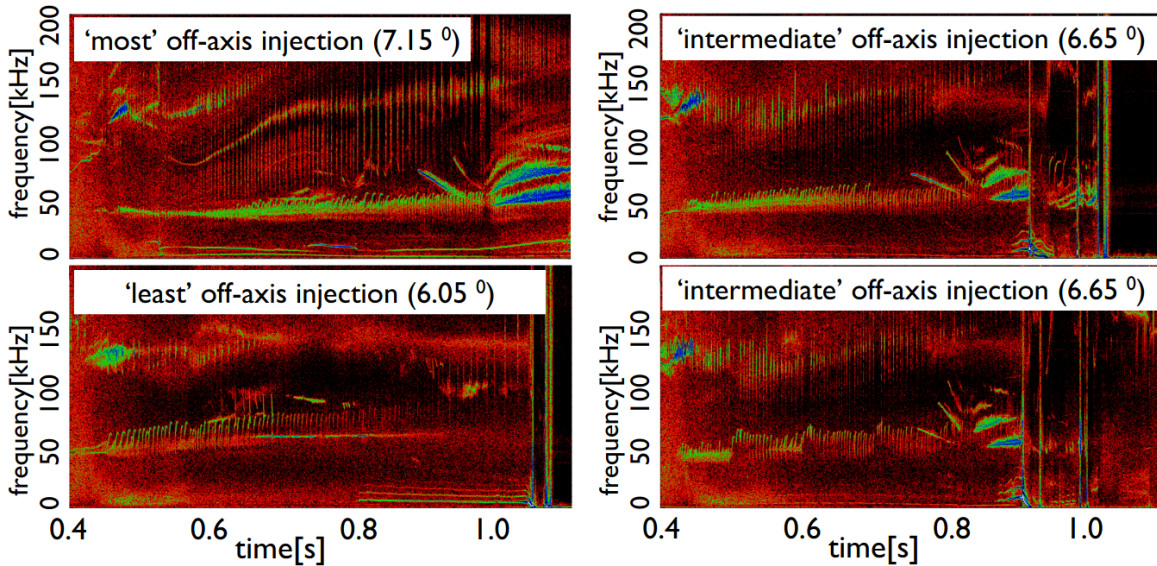
Figure 5.13: Experimental data from NLED-AUG case from magnetic pick-up coils (in order top-left, top-right, bottom-left, bottom-right: #31213,5,4,6)

5.5 Discussion and chapter summary

In this chapter we showed how we made significant progress toward the capability of simulating a realistic scenario for a burning plasma fusion scenario. Specifically, non-linear electromagnetic multi-mode simulations have been proved to have the ability to reproduce the dynamics of anisotropic EP distribution functions in a manner that is coherent with experimental findings. These simulations employed new experimental-

like EP distribution functions to attempt to accurately simulate the experimental configuration of the NLED-AUG case [70].

In the present chapter, such realistic simulations were run with the gyrokinetic code ORB5, aiming to reconstruct the experimental, coupled dynamics of GAMs and AWs [70], which linear studies [50] (see chapter 4) failed to reproduce from a qualitative point of view.

For the analytical ASD EP distribution function (section 5.2), the non-linear simulations that retained both $n = \{0, 1\}$ modes, demonstrated the possibility of exciting ZS through non-linear wave-wave coupling between AWs and ZS. This was found to be true even for those cases where the linear drive of the EPs on the GAM alone was insufficient to drive them unstable (sections 4.3.3 and 5.2). These simulations presented good agreement with theory and previous simulations [57, 58], despite the realistic geometry, scenario, and safety factor profile which set us away from ideal configurations used in literature. More specifically, throughout the scan of the analytical ASD F_0 for various ξ_0 and σ_ξ values, it was consistently observed that the growth rates of non-linearly driven $n = \{0\}$ modes were positive, thanks to the wave-wave coupling with Alfvén Waves. As described in Subsection 5.2, beyond a certain threshold of $\gamma_{AW,n=0,1}$ (e.g., for $\xi_0 < -0.5$ at $\sigma_\xi = 0.2$), the $\gamma_{ZS,n=0,1}$ followed the theoretical expectations proposed by Qiu et al. [57] (see section 5.2.3):

$$\gamma_{ZS,n=\{0,1\}} = 2 \cdot \gamma_{AW,n=\{0,1\}} \cdot \tag{5.9}$$

Hence, considering that the growth rates of AW were found to be higher for pitch angles closer to the magnetic axis ($\xi_0 \longrightarrow -1$), a similar γ_{ZS} trend was observed for non-linearly driven ZS. Depending on the preferred pitch angle of the particles, the AW could manifest as a TAE ($\xi_0 \geq -0.4$ at $\sigma_\xi = 0.2$) or an EPM ($\xi_0 < -0.4$). As discussed in section 5.2.3, EPMs exhibited lower saturation levels compared to TAEs.

Furthermore, significant results were also obtained when employing the experimental-like numerical distribution functions obtained from the heating solver code RABBIT as input in ORB5. In section 5.3, it was observed that the non-linear drive of AWs could destabilize ZS in cases where they were previously considered stable considering solely the linear EP drive.

In the NLED-AUG case, namely shots #31213-6 in ASDEX-Upgrade, ORB5 simulations successfully reproduced the unstable dynamics of $n = \{0\}$ EGAMs observed in the experimental findings. The growth rate measurements of the different modes (AWs, EGAMs) from the simulations also demonstrated a strong agreement with Qiu's theory (fig. 5.11). However, the simulations did not fully reproduce the quantitative trend of the growth rates depending on the injection angle observed in the Mirnov coil measurements (fig. 5.13). The simulation results showed higher growth rates for lower

NBI angles, indicating that the dominant driving effect on the ZS is originated from the non-linear coupling with AWs (see section 5.2 and 5.3 for details). Conversely, the magnetic measurements displayed present an opposite trend, with the most unstable cases corresponding to the most off-axis NBI angles (figure 5.13). This suggests that the linear drive of EGAMs [50], whose effects were analyzed in chapter 4, may also have a quantitative impact on the growth rate of non-linearly driven modes. Section 5.4 provides further insights and explanations for this quantitative discrepancy. In this section, an ideal combination of these two driving effects (the linear and the non-linear ones) is hoped in the future for the accurate interpretation of experimental measurements from NLED-AUG case.

In conclusion, the implementation of new numerical tools in ORB5 has yielded very promising results in terms of qualitative agreement between the simulated experimental NLED-AUG scenarios and the actual experimental measurements. Despite having found to some extent quantitative discrepancies arising from numerical limitations in profile and distribution function representations, we are anyhow confident that in this work and in the recent advancements made in the ORB5 framework we achieved a high degree of development towards predictive tokamak simulations. These developments represent a crucial milestone in the prediction of non-linear energetic particle dynamics within experimentally relevant scenarios, also applicable to burning plasmas configurations. Moving forward, future studies employing these improved numerical tools will hopefully be able to achieve a quantitative alignment with experimental measurements and observations, thereby enabling us to accurately predict the dynamics and transport [65] of energetic particles in realistic and, eventually, burning plasma scenarios.

6 Conclusions and outlook

In this thesis we addressed the problem of EP driven instabilities in experimental relevant plasma scenarios. In future reactors, EP confinement will be crucial for power plant operations. Such confinement, as demonstrated in literature and in this work, sensibly depends on the dynamics of EPs through the excitation of EP driven instabilities such as the Alfvén Waves and the EP driven Geodesic Acoustic Mode (EGAM). The capability to predictively simulate EP dynamics in experimental relevant scenarios is fundamental for such operations [68].

As it has been more thoroughly explained in section 1.5, this work is one of the first attempt to combine different features and numerical tools, together with theory from literature and experimental observations, in order to investigate how the global, multi-mode, non-linear physics of EPs, and the subsequent transport, work in experimental relevant scenarios (section 1.5).

To this purpose we tested experimental like EP distribution functions, attempting to reconstruct the experimental case of NLED-AUG scenario. We used the non-linear, global, electromagnetic, gyrokinetic PIC code ORB5 [69] for our multi-mode simulations. Experimental equilibrium and profiles from the NLED-AUG case [70] were used in order to reconstruct a realistic scenario for the simulation of EP dynamics.

The novelty of this thesis lies in the analysis of the dynamics of EP instabilities depending on newly implemented anisotropic EP distribution functions. Furthermore, this has been done while analyzing the interplay of two different EP-driven modes (AWs and EGAMs) in an experimental scenario in order to determine which saturation mechanism was dominant in the experimental observations from NLED-AUG case, whether the linear wave-particle channel or the non-linear wave-wave coupling channel. In fact, we introduced two new experimental-like distribution functions as input in ORB5 [50] (details in chapter 3). We developed an analytical distribution function which parametrizes phase-space anisotropy as a function of two parameters (section 3.3.1). We also employed a numerical distribution function generated from the Fokker-Planck solver RABBIT which represent the closest distribution function to the experimental one (section 3.3.2). The two distribution functions were compared highlighting their similarities and differences (section 3.3.3).

We ran many parameter scans of ORB5 simulations using NLED-AUG case scenario and the aforementioned EP distribution functions. At first we ran these scans linearly

and electrostatically, retaining only the $n = \{0\}$ modes. Later, we performed similar scans analyzing the effects of different distribution functions and parameters on the nonlinear dynamics of both Zonal Structures (ZS) and AWs. The results are summarized below.

At first, through this thesis we provide a comprehensive analysis of the linear stability of EGAMs under the influence of anisotropic EP distribution functions. As said, the study begins by introducing a novel analytical distribution function that incorporates anisotropic and asymmetric properties, parametrized by ξ_0 and σ_ξ. Analytical studies are conducted to determine stability conditions by examining the dispersion relation of EGAMs (section 4.1). The findings indicate that EGAMs are primarily excited when σ_ξ is low, and ξ_0 is approximately -0.5. However, precise threshold values for these parameters necessitate further exploration through numerical simulations.

To determine the threshold values, extensive scans are performed using the ORB5 code, which enables an exploration of EGAM stability across the parameter space (ξ_0, σ_ξ), and the EP density fraction $\langle n_{EP} \rangle / \langle n_e \rangle$ (section 4.3). The simulation results reveal that modes become unstable for low σ_ξ values within the ξ_0 range of -0.8 to -0.3. Furthermore, we also used the power exchange diagnostic (MPR) to study the EP contributions to the excitation and damping of EGAMs (section 4.3.4).

After that, we employed the numerical experimental like distribution functions from the RABBIT code. These distribution functions, combined with temperature and density profiles from the four different shots of NLED-AUG case, are utilized as input for ORB5 simulations (section 4.4). The simulation results showed that EGAMs should be linearly stable in these scenarios, contrary to the experimental observation. We used the MPR diagnostic to shed light on this result, revealing a more complex power exchange structure compared to the analytical distribution function cases. Notably, the presence of steep negative gradients in energy at different injection velocities seem to cause the observed damping rates in the RABBIT cases (section 4.4.1).

Qualitative comparisons are performed between the analytical F_0 and the RABBIT F_0 results (section 4.4.3), as well as between the RABBIT simulation results and experimental measurements of EP instabilities (section 4.4.4). In experiments with a nominal EP fraction of about 9%, EGAMs are found to be excited in all AUG cases, even though with varying growth rates. However, in linear simulations using the experimental setup no unstable modes are observed. In the thesis we showed that the neglected interaction between $n = 1$ Alfvén waves and EGAMs represents a crucial nonlinear effect for the NLED-AUG case . As a result, it is concluded that the numerical realistic anisotropic distribution function alone is insufficient to linearly drive EGAMs unstable at such low energetic particle density fractions.

Overall, in this first part of the thesis, good agreement between simulations, analytical expectations, and theoretical predictions was found. This demonstrates that

the gyrokinetic code ORB5 is capable of handling experimental-like anisotropic EP distribution functions, both analytical and numerical. This work is based on the results published in reference [50].

The second part of this thesis focuses on non-linear electromagnetic multi-mode simulations. In this way we reproduced the dynamics of anisotropic EP distribution functions more consistently with the experimental findings (details in chapter 5). We ran scans similar to those discussed above this time retaining non-linearities and $n = \{1\}$ modes. When employing the analytical ASD distribution function, all non-linear simulations show the excitation of ZS through wave-wave coupling between AWs and ZS (section 5.2). This occurs even for those cases where the linear drive of the energetic particle population alone is insufficient to drive the instability. The simulations demonstrate good agreement with theory and previous simulations, despite realistic geometry and non-ideal configurations. The growth rates of non-linearly driven modes are positive for certain pitch angles closer to the magnetic axis, which particularly destabilize EPMs, which strongly drive non-linearly ZS unstable.

When using experimental-like numerical distribution functions from the RABBIT, it is also observed that the non-linear drive of AWs can destabilize ZS. These non-linear ORB5 simulations of the NLED-AUG case successfully reproduce the unstable dynamics of EGAMs observed in experiments. The growth rates ratio of different modes from the simulations align well with theory. However, there are quantitative discrepancies in the growth rate trends depending on the NBI injection angle when compared to experiments, possibly due to inaccuracies in experimental measurements of profiles. Ideally, we hope that with more accurate profiles and numerical F_0 representation it will be possible to reconstruct modes whose growth rate will show a combination of linear and non-linear drive mechanisms. These results are based on the work presented/published in [59].

As a remark, this work has been developed in ORB5 using local coordinates for the distribution functions $(\psi, v_\parallel, \epsilon)$. This was done for several reasons, including consistency with previous works done on distribution functions in ORB5, compatibility with RABBIT, and also for straightforward integration with the Vlasov equation of ORB5. In recent years, a lot of effort has been made towards representing equilibrium EP distribution functions in terms of their constants of motion (CoMs), $(P_\phi, \mu, \epsilon, \sigma_{v_\parallel})$ [65, 67]. International efforts towards calculating, handling, and converting distribution functions in CoMs are ongoing at the time of writing. An extension of the current work to treat EPs in CoM representation in ORB5 is left for future work, where the first steps have recently been made [148]. As an aside, in order to do this consistently, particular effort will need to be made in order to ensure quasi-neutrality of the background profiles. Although the distributions in this work were not in CoMs, and therefore might not be expected to be stationary, effort has been made to isolate the effect of the relaxation of the distribution function, using the method described in [49].

To summarize, this thesis project focused on studying the physics of ZS and AMs in experimental ASDEX Upgrade scenarios. Despite the complexity of the simulations, we successfully gained insights into the linear and non-linear dynamics of these modes. The implementation of new numerical tools in ORB5 shows promising qualitative agreement with experimental measurements for the NLED-AUG scenario. It opened the way to more realistic simulations of experimental cases, eventually leading to the possibility of global burning plasmas simulations. Despite some quantitative discrepancies due to numerical limitations, these developments represent significant progress towards predictive tokamak simulations, encouraging and providing a foundation for predicting the dynamics of energetic particles in future fusion devices like ITER.

Future studies using these improved tools aim to achieve quantitative alignment with experimental measurements, enabling accurate predictions of energetic particle dynamics and transport in realistic and burning plasma scenarios. Furthermore, these new numerical tools will hopefully be able to match experimental observations, enabling us to predict EP dynamics and transport [65] also in realistic, and eventually burning plasma, scenarios. This work could be achieved, for example, integrating the tools developed and tested in this and other on-going work with the study of Phase Space Zonal Structures (PSZS) transport theory [65] for these new distribution functions in realistic scenarios. In fact, in this thesis we proved that ORB5 is capable to analyze the non-linear, multi-mode, δf physics of EP on short time-scales consistently with experimental observations. This could be used to derive saturation rules to be used into PSZS transport theory for effective modelling also over long time-scales.

Appendix A
Gyrokinetic Equation

In this appendix we derive the gyrokinetic equation 2.50 presented in section 2.3. We start from the particles characteristics, equations 2.22 to 2.27:

$$\dot{\mathbf{R}} = \dot{\mathbf{R}}^{(0)} + \epsilon_\delta \dot{\mathbf{R}}^{(1)} \ , \tag{1}$$

$$\dot{p_z} = \dot{p_z}^{(0)} + \epsilon_\delta \dot{p_z}^{(1)} \ . \tag{2}$$

$$\dot{\varepsilon} = \dot{\varepsilon}^{(0)} + \epsilon_\delta \dot{\varepsilon}^{(1)} \ . \tag{3}$$

We also make use of Vlasov equation (eq. 3.2):

$$\frac{d\delta f}{dt} = -\frac{dF_0}{dt} \ , \tag{4}$$

where the distribution functions has been split into a background F_0 and a perturbation δf components: $F = F_0 + \delta f$. We hypothesize that the background distribution function is a Maxwellian (as in eq. 2.49), depending only on the energy $\varepsilon = v_\parallel^2/2 + \mu B$:

$$F_0(\varepsilon) = \frac{1}{(2\pi)^{\frac{3}{2}} v_{th}^3} \exp\left(-\frac{\varepsilon}{T}\right) \ . \tag{5}$$

Plugging equation 5 into 4, and applying a linearization getting rid of all the terms higher than the first, we yield:

$$\frac{\partial \delta f}{\partial t} + \dot{\mathbf{R}}^{(0)} \cdot \nabla \delta f + \dot{\varepsilon}^{(0)} \frac{\partial \delta f}{\partial \varepsilon} = -\dot{\varepsilon}\frac{\partial F_0}{\partial \varepsilon} \ . \tag{6}$$

Considering that the full time derivative of the kinetic energy is:

$$\dot{\varepsilon} = v_\parallel \dot{v}_\parallel + \mu \dot{\mathbf{R}} \cdot \nabla B \ , \tag{7}$$

and keeping in mind that the kinetic energy must be preserved along the unperturbed trajectories, we notice that the 0th order time derivative of the kinetic energy is zero:

$\dot{\varepsilon}^{(0)} = 0$ (eq. 3.6). As a consequence Vlasov equation 6 can be simplified in the following way:

$$\frac{\partial \delta f}{\partial t} + \dot{\mathbf{R}}^{(0)} \cdot \nabla \delta f = -\frac{\partial F_0}{\partial \varepsilon}(v_\parallel \dot{v}_\parallel^{(1)} + \mu \dot{\mathbf{R}}^{(1)} \cdot \nabla B) \ . \tag{8}$$

We split the perturbation of the distribution function into an adiabatic part and a non-adiabatic parts:

$$\delta f = -\underbrace{Q\frac{\partial F_0}{\partial \varepsilon}\langle \varphi \rangle_\theta}_{\text{adiabatic component}} + \underbrace{K}_{\text{non-adiabatic component}} \ , \tag{9}$$

where $\langle ... \rangle_\theta$ is the gyroaveraging operator. The adiabatic component of a species distribution function represents those particles that immediately respond to the electric field (as we can see it is directly proportional to the electrostatic potential). This adiabatic component self evidently does not have any phase shift with respect to the potential, thus will not lead to any instability excitation. For example, electron adiabaticity for their low inertia is a reasonable approximation and is very used in GK codes for electrostatic simulations as those shown in Chapter 4. Using equation 9 we can recast Vlasov equation 8 in the following form:

$$\frac{\partial K}{\partial t} + \dot{\mathbf{R}}^{(0)} \cdot \nabla K + Q\frac{\partial F_0}{\partial \varepsilon}\frac{\partial \langle \varphi \rangle_\theta}{\partial t} = -\frac{\partial F_0}{\partial \varepsilon}[Q\dot{\mathbf{R}}^{(0)} \cdot \nabla \langle \varphi \rangle_\theta + v_\parallel \dot{v}_\parallel^{(1)} + \mu \dot{\mathbf{R}}^{(1)} \cdot \nabla B] \ . \tag{10}$$

Considering the characteristic of the particles and the expressions of $\dot{\mathbf{R}}^{(0)}$, $\dot{\mathbf{R}}^{(1)}$ and $v_\parallel^{(1)}$ from section 2.1 and assuming $B_\parallel^* \simeq B_0$, we find that the part of the above equation between the square brackets is zero. We can rewrite the scalar potential and the non adiabatic response of the EP in Laplace and Fourier components:

$$\varphi \longrightarrow \varphi \exp(ik_r r + ik_\phi \phi - i\hat{\omega}t) \ , \tag{11}$$

$$K \longrightarrow K \exp(ik_r r + ik_\phi \phi - i\hat{\omega}t) \ , \tag{12}$$

where r and ϕ are respectively the radial and toroidal coordinate, k_r and k_ϕ the radial and toroidal wave number and $\hat{\omega}$ is the complex GAM frequency (as in section 2.3). Plugging these transformations in equation 10 we yield a new expression for the GK Vlasov equation:

$$[\omega_{tr}\partial_\chi - i(\hat{\omega} + \omega_d)]K = -i\frac{Q\hat{\omega}}{T}F_0 J_0(k_\perp \rho)\varphi \ , \tag{13}$$

with ω_{tr} and ω_d as described in section 2.3 (eq. 2.52), and the gyroaveraging operator $\langle...\rangle_\theta$ has been replaced by the Bessel function of the first kind: $J_0(k_\perp \rho)$. Here, $k_\perp \rho$ is the normalized perpendicular wave number. Finally, we can split the electrostatic potential in a zonal (poloidally symmetric or small k_χ) component $\overline{\varphi}$ and a non-zonal (poloidally varying or high k_χ) one $\widetilde{\delta\varphi}$:

$$\varphi = \overline{\varphi} + \widetilde{\delta\varphi} \,. \tag{14}$$

The same can be done for the non-adiabatic part of the distribution function:

$$K = \overline{K} + \delta K \,. \tag{15}$$

Noticing that the zonal components have zero poloidal derivative: $\partial_\chi \overline{...} = 0$, and assuming that $\omega_{tr} \gg \omega_d$ we see that for the zonal component of equation 13 we get:

$$\overline{K} = \frac{Q}{T} F_0 J_0(k_\perp \rho) \overline{\varphi} \,. \tag{16}$$

Plugging the previous expressions into equation 13 we get the GK equation as presented in section 2.3 (equation 2.50):

$$[\omega_{tr}\partial_\chi - i(\hat{\omega} + \omega_d)]\delta K = -i\frac{Q}{T}F_0\left(\hat{\omega} J_0(k_\perp \rho)\widetilde{\delta\varphi} + \omega_d J_0(k_\perp \rho)\overline{\varphi}\right) \,. \tag{17}$$

In order to get to the expression show in Eq. 2.50 we need to use the ordering used for the GAM dispersion relation. We hypothesize that the radial wave number is small $k_r\rho \ll 1$. This allows us to consider the Bessel function $J_0 \sim 1$ at the smallest order. We introduce the smallness parameter (section 2.3): $\omega_d/\hat{\omega} \sim k_r/\rho_L \sim \epsilon$. We assume the non-zonal component of the electric field $\widetilde{\delta\varphi}$ to be much smaller than the zonal component: $\widetilde{\delta\varphi}/\overline{\varphi} \sim \epsilon$. From equation 16 we derive that $\overline{K}/F_0 \sim \mathcal{O}(1)$, while $\delta K/F_0 \sim \mathcal{O}(\epsilon)$. For the electrons, because of their low mass, the transit frequency is dominant over all the other frequencies obtaining $\omega_{tr,e}/\hat{\omega} \sim \mathcal{O}(\epsilon^{-1})$, while for ions $\omega_{tr,i}/\hat{\omega} \sim \mathcal{O}(1)$. From the above considerations, for electrons we can rewrite equation 17 at the lowest order:

$$\omega_{tr,e}\partial_\chi \delta K_e = 0 \,. \tag{18}$$

The meaning of eq. 18 is that electrons don't have a non-adiabatic response. Therefore, electrons can be considered fully adiabatic. This approximation, in fact, has been considered throughout Chapter 4. Considering the $\mathcal{O}(\epsilon)$ order components of equation 17 for ions and keeping in mind the hypothesis above we get equation 2.50 as presented in section 2.3:

$$(\omega_{tr}\partial_\chi - i\hat{\omega})\delta K_i = -i\hat{\omega}\frac{F_{0,i}q}{T_i}\left(\widetilde{\delta\varphi} - \frac{\omega_d}{\hat{\omega}}\overline{\delta\varphi}\right).$$
(19)

Bibliography

[1]   A. M. Bradshaw et al. "Is nuclear fusion a sustainable energy form?", *Fusion Engineering and Design* 86, 9-11 (2011), pp. 2770–2773.

[2]   A. Gore. "An inconvenient truth", (2007).

[3]   A. Lépine-Szily et al. "Nuclear astrophysics: nucleosynthesis in the Universe", *International journal of astrobiology* 11, 4 (2012), pp. 243–250.

[4]   J. D. Lawson. "Some criteria for a power producing thermonuclear reactor", *Proceedings of the physical society. Section B* 70, 1 (1957), p. 6.

[5]   J. Wesson et al. *Tokamaks*. Vol. 149. Oxford university press, 2011.

[6]   B. Dstrozzi. https://commons.wikimedia.org/w/index.php?curid=12153588. This file is licensed under the Creative Commons Attribution-Share Alike 3.0 Unported license.

[7]   A. A. Vlasov. "The vibrational properties of an electron gas", *Soviet Physics Uspekhi* 10, 6 (1968), p. 721.

[8]   H. Zohm. *Magnetohydrodynamic stability of tokamaks*. John Wiley & Sons, 2015.

[9]   J. H. Goedbloed et al. *Principles of magnetohydrodynamics: with applications to laboratory and astrophysical plasmas*. Cambridge university press, 2004.

[10] J. P. Goedbloed et al. *Advanced magnetohydrodynamics: with applications to laboratory and astrophysical plasmas*. Cambridge University Press, 2010.

[11] H. Alfvén. "Existence of electromagnetic-hydrodynamic waves", *Nature* 150, 3805 (1942), pp. 405–406.

[12] H. Alfvén. *Cosmical electrodynamics.*, 1963.

[13] O. Maj. "A mathematical introduction to magnetohydrodynamics," *Vorlesung (SS 2017)*. 2017, pp. 1–222.

[14] R. M. Kulsrud. "MHD description of plasma", *Handbook of plasma physics* 1, (1983), p. 115.

[15] U. S. Inan et al. *Principles of plasma physics for engineers and scientists*. Cambridge University Press, 2010.

[16] H. Grad et al. "Hydromagnetic equilibria and force-free fields", *Journal of Nuclear Energy (1954)* 7, 3-4 (1958), pp. 284–285.

[17] V. Shafranov. "Plasma equilibrium in a magnetic field", *Reviews of plasma physics* 2, (1966), p. 103.

[18] B. V. Somov. *Cosmic plasma physics.* Vol. 251. Springer Science & Business Media, 2013.

[19] M. Andrenucci. "Magnetoplasmadynamic thrusters", *Encyclopedia of Aerospace Engineering* (2010).

[20] R. J. Pearson et al. "Review of approaches to fusion energy," *Commercialising Fusion Energy: How small businesses are transforming big science.* IOP Publishing, 2020.

[21] M. Haines. "A review of the dense Z-pinch", *Plasma Physics and Controlled Fusion* 53, 9 (2011), p. 093001.

[22] D. Ryutov et al. "The physics of fast Z pinches", *Reviews of Modern Physics* 72, 1 (2000), p. 167.

[23] J. Taylor et al. "Special topics in plasma confinement", *Journal of Plasma Physics* 81, 5 (2015), p. 205810501.

[24] V. Igochine et al. *Active control of magneto-hydrodynamic instabilities in hot plasmas.* Springer, 2015.

[25] R. Wolf et al. "Performance of Wendelstein 7-X stellarator plasmas during the first divertor operation phase", *Physics of Plasmas* 26, 8 (2019), p. 082504.

[26] U. Stroth et al. "Stellarator-tokamak energy confinement comparison based on ASDEX Upgrade and Wendelstein 7-X hydrogen plasmas", *Nuclear Fusion* 61, 1 (2020), p. 016003.

[27] E. Kikuchi et al. *Fusion Physics (IAEA, 2012).*

[28] V. Smirnov. "Tokamak foundation in USSR/Russia 1950–1990", *Nuclear fusion* 50, 1 (2009), p. 014003.

[29] N. Peacock et al. "Measurement of the electron temperature by Thomson scattering in tokamak T3", *Nature* 224, 5218 (1969), pp. 488–490.

[30] L. Artsimovich. "Tokamak devices", *Nuclear Fusion* 12, 2 (1972), p. 215.

[31] B. Green et al. "ITER: burning plasma physics experiment", *Plasma physics and controlled fusion* 45, 5 (2003), p. 687.

[32] A. Creely et al. "Overview of the SPARC tokamak", *Journal of Plasma Physics* 86, 5 (2020), p. 865860502.

[33] A. Herrmann et al. "Chapter 1: Asdex upgrade-introduction and overview", *Fusion Science and Technology* 44, 3 (2003), pp. 569–577.

[34] U. Stroth et al. "Progress from ASDEX Upgrade experiments in preparing the physics basis of ITER operation and DEMO scenario development", *Nuclear Fusion* 62, 4 (2022), p. 042006.

[35] B. Kurzan et al. "Edge and core Thomson scattering systems and their calibration on the ASDEX Upgrade tokamak", *Review of scientific instruments* 82, 10 (2011), p. 103501.

[36] E. Viezzer et al. "High-resolution charge exchange measurements at ASDEX Upgrade", *Review of scientific Instruments* 83, 10 (2012), p. 103501.

[37] G. De Tommasi. "Plasma magnetic control in tokamak devices", *Journal of Fusion Energy* 38, 3-4 (2019), pp. 406–436.

[38] J. A. Rome et al. "The topology of tokamak orbits", *Nuclear fusion* 19, 9 (1979), p. 1193.

[39] J. Faustin et al. "Fast particle loss channels in Wendelstein 7-X", *Nuclear Fusion* 56, 9 (2016), p. 092006.

[40] L. Chen et al. "Theory of Alfvén waves and energetic particle physics in burning plasmas", *Nuclear Fusion* 47, 10 (2007), S727.

[41] W. Core. "A note on the calculation of NBI fast ion distribution functions", *Nuclear fusion* 33, 5 (1993), p. 829.

[42] M. Weiland et al. "RABBIT: Real-time simulation of the NBI fast-ion distribution", *Nuclear Fusion* 58, 8 (2018), p. 082032.

[43] G. Vlad et al. "Dynamics of Alfvén waves in tokamaks", *La Rivista del Nuovo Cimento (1978-1999)* 22, 7 (1999), p. 1.

[44] G. D. Conway et al. "Geodesic Acoustic Modes in magnetic confinement devices", *Nuclear Fusion* (2021).

[45] L. Chen et al. "Physics of Alfvén waves and energetic particles in burning plasmas", *Reviews of Modern Physics* 88, 1 (2016), p. 015008.

[46] A. Biancalani et al. "Nonlinear velocity redistribution caused by energetic-particle-driven geodesic acoustic modes, mapped with the beam-plasma system", *Journal of Plasma Physics* 84, 6 (2018).

[47] R. Betti et al. "Stability of Alfvén gap modes in burning plasmas", *Physics of Fluids B: Plasma Physics* 4, 6 (1992), pp. 1465–1474.

[48] I. Novikau et al. "Implementation of energy transfer technique in ORB5 to study collisionless wave-particle interactions in phase-space", *Computer Physics Communications* (2019), p. 107032.

[49] D. Zarzoso et al. "Analytic dispersion relation of energetic particle driven geodesic acoustic modes and simulations with NEMORB", *Nuclear Fusion* 54, 10 (2014), p. 103006.

[50] B. Rettino et al. "Gyrokinetic modeling of anisotropic energetic particle driven instabilities in tokamak plasmas", *Nuclear Fusion* 62, 7 (2022), p. 076027.

[51] M. Osakabe et al. *Indication of bulk-ion heating by energetic particle driven Geodesic Acoustic Modes on LHD.* Tech. rep. National Inst. for Fusion Science, 2014.

[52] M. Sasaki et al. "Energy channeling from energetic particles to bulk ions via beam-driven geodesic acoustic modes—GAM channeling", *Plasma Physics and Controlled Fusion* 53, 8 (2011), p. 085017.

[53] D. Zarzoso et al. "Nonlinear interaction between energetic particles and turbulence in gyro-kinetic simulations and impact on turbulence properties", *Nuclear Fusion* 57, 7 (2017), p. 072011.

[54] K. Shinohara et al. "Energetic particle physics in JT-60U and JFT-2M", *Plasma physics and controlled fusion* 46, 7 (2004), S31.

[55] A. Bierwage et al. "Simulations tackle abrupt massive migrations of energetic beam ions in a tokamak plasma", *Nature Communications* 9, 1 (2018), p. 3282.

[56] Y. Kusama et al. "Characteristics of Alfvén eigenmodes, burst modes and chirping modes in the Alfvén frequency range driven by negative ion based neutral beam injection in JT-60U", *Nuclear Fusion* 39, 11Y (1999), p. 1837.

[57] Z. Qiu et al. "Effects of energetic particles on zonal flow generation by toroidal Alfvén eigenmode", *Physics of Plasmas* 23, 9 (2016), p. 090702.

[58] F. Vannini et al. "Gyrokinetic investigation of the nonlinear interaction of Alfvén instabilities and energetic particle-driven geodesic acoustic modes", *Physics of Plasmas* 28, 7 (2021), p. 072504.

[59] B. Rettino et al. "Gyrokinetic modelling of non-linear interaction of Alfvén Waves and EGAMs in ASDEX-Upgrade", *Nuclear Fusion* (submitted), (2023).

[60] F. Zonca et al. "Energetic particles and multi-scale dynamics in fusion plasmas", *Plasma Physics and Controlled Fusion* 57, 1 (2014), p. 014024.

[61] F. Zonca et al. "Nonlinear dynamics of phase space zonal structures and energetic particle physics in fusion plasmas", *New Journal of Physics* 17, 1 (2015), p. 013052.

[62] F. Vannini et al. "Gyrokinetic investigation of the damping channels of Alfvén modes in ASDEX Upgrade", *Physics of Plasmas* 27, 4 (2020), p. 042501.

[63] T. Hayward-Schneider. "Global nonlinear fully gyrokinetic and hybrid treatments of Alfvénic instabilities in ITER", (2020).

[64] M. V. Falessi. "Gyrokinetic theory for particle transport in fusion plasmas", *arXiv preprint arXiv:1701.02202* (2017).

[65] M. V. Falessi et al. "Transport theory of phase space zonal structures", *Physics of Plasmas* 26, 2 (2019), p. 022305.

[66] F. Zonca et al. "Nonlinear radial envelope evolution equations and energetic particle transport in tokamak plasmas," *Journal of Physics: Conference Series*. Vol. 1785. 1. IOP Publishing. 2021, p. 012005.

[67] M. V. Falessi et al. "Nonlinear equilibria and transport processes in burning plasmas", *arXiv preprint arXiv:2306.08642* (2023).

[68] A. Mishchenko et al. "Numerical tools for burning plasmas", *Plasma Physics and Controlled Fusion* (2023).

[69] E. Lanti et al. "ORB5: a global electromagnetic gyrokinetic code using the PIC approach in toroidal geometry", *Computer Physics Communications* 251, (2020), p. 107072.

[70] P. Lauber. "Off-axis NBI heated discharges at ASDEX Upgrade: EGAMs, RSAEs, TAE bursts," *13th Energetic Particle Physics TG Meeting*. 2014.

[71] P. Lauber. `https://pwl.home.ipp.mpg.de/NLED_AUG//data.html`.

[72] S. Sharapov et al. "MHD spectroscopy through detecting toroidal Alfvén eigenmodes and Alfvén wave cascades", *Physics Letters A* 289, 3 (2001), pp. 127–134.

[73] F. Vannini et al. "Gyrokinetic modelling of the Alfvén mode activity in ASDEX Upgrade with an isotropic slowing-down fast-particle distribution", *Nuclear Fusion* 62, 12 (2022), p. 126042.

[74] R. G. Littlejohn. "Hamiltonian formulation of guiding center motion", *The Physics of Fluids* 24, (1981), p. 1730.

[75] A. J. Brizard et al. "Foundations of nonlinear gyrokinetic theory", *Reviews of modern physics* 79, 2 (2007), p. 421.

[76] A. J. Brizard. "Variational principle for nonlinear gyrokinetic Vlasov–Maxwell equations", *Physics of Plasmas* 7, 12 (2000), pp. 4816–4822.

[77] R. G. Littlejohn. "Variational principles of guiding centre motion", *Journal of Plasma Physics* 29, 1 (1983), pp. 111–125.

[78] A. Brizard. "Gyrokinetic energy conservation and Poisson-bracket formulation", *Physics of Fluids B: Plasma Physics* 1, 7 (1989), pp. 1381–1384.

[79] N. Tronko et al. "Second order gyrokinetic theory for particle-in-cell codes", *Physics of Plasmas* 23, 8 (2016), p. 082505.

[80] H. Sugama. "Gyrokinetic field theory", *Physics of Plasmas* 7, 2 (2000), pp. 466–480.

[81] A. Bottino et al. "Monte Carlo particle-in-cell methods for the simulation of the Vlasov–Maxwell gyrokinetic equations", *Journal of Plasma Physics* 81, 5 (2015), p. 435810501.

[82] R. Hager et al. "Electromagnetic total-f algorithm for gyrokinetic particle-in-cell simulations of boundary plasma in XGC", *Physics of Plasmas* 29, 11 (2022), p. 112308.

[83] F. Jenko et al. "Electron temperature gradient driven turbulence", *Physics of plasmas* 7, 5 (2000), pp. 1904–1910.

[84] M. Garcia-Munoz et al. "Fast-ion transport induced by Alfvén eigenmodes in the ASDEX Upgrade tokamak", *Nuclear Fusion* 51, 10 (2011), p. 103013.

[85] J. Hiratsuka et al. "Achievement of high power and long pulse negative ion beam acceleration for JT-60SA NBI", *Review of Scientific Instruments* 91, 2 (2020), p. 023506.

[86] U. Fantz et al. "Achievement of the ITER NBI ion source parameters for hydrogen at the test facility ELISE and present Status for deuterium", *Fusion Engineering and Design* 156, (2020), p. 111609.

[87] L. Landau et al. "61–On the vibrations of the electronic plasma", *The Collected Papers of LD Landau* (1965), pp. 445–460.

[88] T. M. O'Neil et al. "Transition of the Dispersion Roots from Beam-Type to Landau-Type Solutions", *Physics of Fluids* 11, (1968), pp. 1754–1760.

[89] P. Manz et al. "Physical mechanism behind zonal-flow generation in drift-wave turbulence", *Physical review letters* 103, 16 (2009), p. 165004.

[90] R. Z. Sagdeev et al. "Nonlinear plasma theory", *Nonlinear Plasma Theory* (1969).

[91] A. Di Siena et al. "Effect of elongation on energetic particle-induced geodesic acoustic mode", *Nuclear Fusion* 58, 10 (2018), p. 106014.

[92] F. Romanelli. "Ion temperature-gradient-driven modes and anomalous ion transport in tokamaks", *Physics of Fluids B: Plasma Physics* 1, 5 (1989), pp. 1018–1025.

[93] A. Di Siena et al. "Electromagnetic turbulence suppression by energetic particle driven modes", *Nuclear Fusion* 59, 12 (2019), p. 124001.

[94] N. Winsor et al. "Geodesic acoustic waves in hydromagnetic systems", *The Physics of Fluids* 11, 11 (1968), pp. 2448–2450.

[95] L. Chen. *Waves and instabilities in plasmas.* Vol. 12. World scientific, 1987.

[96] A. Smolyakov et al. "On the dispersion of geodesic acoustic modes", *Plasma Physics Reports* 42, 5 (2016), pp. 407–417.

[97] F. Zonca et al. "Kinetic theory of low-frequency Alfvén modes in tokamaks", *Plasma physics and controlled fusion* 38, 11 (1996), p. 2011.

[98] H. Sugama et al. "Collisionless damping of geodesic acoustic modes", *Journal of plasma physics* 72, 6 (2006), pp. 825–828.

[99] Z. Qiu et al. "Collisionless damping of short wavelength geodesic acoustic modes", *Plasma Physics and Controlled Fusion* 51, 1 (2008), p. 012001.

[100] Z. Qiu et al. "Nonlocal theory of energetic-particle-induced geodesic acoustic mode", *Plasma Physics and Controlled Fusion* 52, 9 (2010), p. 095003.

[101] G. Y. Fu. "Energetic-particle-induced geodesic acoustic mode", *Physical review letters* 101, 18 (2008), p. 185002.

[102] I. Chavdarovski et al. "Linear dispersion relation of geodesic acoustic modes driven by trapped and circulating energetic particles", *Journal of Plasma Physics* 87, 4 (2021).

[103] R. Nazikian et al. "Intense geodesic acousticlike modes driven by suprathermal ions in a tokamak plasma", *Physical review letters* 101, 18 (2008), p. 185001.

[104] Q. Zhiyong et al. "Kinetic theories of geodesic acoustic modes: Radial structure, linear excitation by energetic particles and nonlinear saturation", *Plasma Science and Technology* 13, 3 (2011), p. 257.

[105] I. Novikau et al. "Nonlinear dynamics of energetic-particle driven geodesic acoustic modes in ASDEX Upgrade", *Physics of Plasmas* 27, 4 (2020), p. 042512. eprint: `https://doi.org/10.1063/1.5142802`.

[106]   A. Biancalani et al. "Saturation of energetic-particle-driven geodesic acoustic modes due to wave–particle nonlinearity", *Journal of Plasma Physics* 83, 6 (2017).

[107]   I. Chavdarovski et al. "Effects of trapped particle dynamics on the structures of a low-frequency shear Alfvén continuous spectrum", *Plasma Physics and Controlled Fusion* 51, 11 (2009), p. 115001.

[108]   I. Chavdarovski et al. "Analytic studies of dispersive properties of shear Alfvén and acoustic wave spectra in tokamaks", *Physics of Plasmas* 21, 5 (2014), p. 052506.

[109]   J.-B. Girardo et al. "Relation between energetic and standard geodesic acoustic modes", *Physics of Plasmas* 21, 9 (2014), p. 092507.

[110]   D. Zarzoso et al. "Fully kinetic description of the linear excitation and nonlinear saturation of fast-ion-driven geodesic acoustic mode instability", *Physics of Plasmas* 19, 2 (2012), p. 022102.

[111]   A. Biancalani et al. "Cross-code gyrokinetic verification and benchmark on the linear collisionless dynamics of the geodesic acoustic mode", *Physics of Plasmas* 24, 6 (2017), p. 062512.

[112]   Z. Gao. "Plasma shaping effects on the geodesic acoustic mode in the large orbit drift width limit", *Physics of Plasmas* 17, 9 (2010), p. 092503.

[113]   A. Biancalani et al. "Interaction of geodesic acoustic modes and energetic particles in tokamaks," *6th International Workshop on the Theory and Applications of the Vlasov Equation (VLASOVIA 2019)*. 2019.

[114]   Z. Gao et al. "Plasma elongation effects on temperature gradient driven instabilities and geodesic acoustic modes", *Nuclear fusion* 49, 4 (2009), p. 045014.

[115]   F. Zonca et al. "Radial structures and nonlinear excitation of geodesic acoustic modes", *EPL (Europhysics Letters)* 83, 3 (2008), p. 35001.

[116]   Q. Zhiyong et al. "Kinetic theory of geodesic acoustic modes in toroidal plasmas: a brief review", *Plasma Science and Technology* 20, 9 (2018), p. 094004.

[117]   E. Frieman et al. "Nonlinear gyrokinetic equations for low-frequency electromagnetic waves in general plasma equilibria", *The Physics of Fluids* 25, 3 (1982), pp. 502–508.

[118]   R. Cairns et al. "Application to fusion and space research", *Plasma Physics* (1985), p. 104.

[119]   C. Cheng et al. "High-n ideal and resistive shear Alfvén waves in tokamaks", *Annals of Physics* 161, 1 (1985), pp. 21–47.

[120] L. Chen. "Theory of magnetohydrodynamic instabilities excited by energetic particles in tokamaks", *Physics of Plasmas* 1, 5 (1994), pp. 1519–1522.

[121] P. Lauber et al. "LIGKA: A linear gyrokinetic code for the description of background kinetic and fast particle effects on the MHD stability in tokamaks", *Journal of Computational Physics* 226, 1 (2007), pp. 447–465.

[122] K. Hain et al. "Zur Stabilität zylindersymmetrischer plasmakonfigurationen mit volumenströmen", *Zeitschrift für Naturforschung A* 13, 11 (1958), pp. 936–940.

[123] A. Hasegawa et al. "Plasma heating by Alfvén-wave phase mixing", *Physical Review Letters* 32, 9 (1974), p. 454.

[124] P. Lauber et al. "Kinetic Alfvén eigenmodes at ASDEX upgrade", *Plasma Physics and Controlled Fusion* 51, 12 (2009), p. 124009.

[125] G. Fu et al. "Excitation of the toroidicity-induced shear Alfvén eigenmode by fusion alpha particles in an ignited tokamak", *Physics of Fluids B: Plasma Physics* 1, 10 (1989), pp. 1949–1952.

[126] C. Cheng et al. "Low-n shear Alfvén spectra in axisymmetric toroidal plasmas", *The Physics of fluids* 29, 11 (1986), pp. 3695–3701.

[127] D. J. Sigmar et al. "Alpha-particle losses from toroidicity-induced Alfvén eigenmodes. Part II: Monte Carlo simulations and anomalous alpha-loss processes", *Physics of Fluids B* 4, 6 (1992), pp. 1506–1516.

[128] R. Betti et al. "Ellipticity induced Alfvén eigenmodes", *Physics of Fluids B: Plasma Physics* 3, 8 (1991), pp. 1865–1870.

[129] L. Villard et al. "Geometrical and profile effects on toroidicity and ellipticity induced Alfvén eigenmodes", *Nuclear fusion* 32, 10 (1992), p. 1695.

[130] L. Chen et al. "Nonlinear excitations of zonal structures by toroidal Alfvén eigenmodes", *Physical Review Letters* 109, 14 (2012), p. 145002.

[131] Y. Todo et al. "Nonlinear magnetohydrodynamic effects on Alfvén eigenmode evolution and zonal flow generation", *Nuclear Fusion* 50, 8 (2010), p. 084016.

[132] Z. Qiu et al. "Fine structure zonal flow excitation by beta-induced Alfvén eigenmode", *Nuclear Fusion* 56, 10 (2016), p. 106013.

[133] S. Jolliet et al. "A global collisionless PIC code in magnetic coordinates", *Computer Physics Communications* 177, 5 (2007), pp. 409–425.

[134] A. Bottino et al. "Global simulations of tokamak microturbulence: finite-β effects and collisions", *Plasma Physics and Controlled Fusion* 53, 12 (2011), p. 124027.

[135] N. Tronko et al. "Hierarchy of second order gyrokinetic Hamiltonian models for particle-in-cell codes", *Plasma Physics and Controlled Fusion* 59, 6 (2017), p. 064008.

[136] M. Sadr et al. "Linear and nonlinear excitation of TAE modes by external electromagnetic perturbations using ORB5", *Plasma Physics and Controlled Fusion* 64, 8 (2022), p. 085010.

[137] A. Mishchenko et al. "Mitigation of the cancellation problem in the gyrokinetic particle-in-cell simulations of global electromagnetic modes", *Physics of Plasmas* 24, 8 (2017), p. 081206.

[138] A. Mishchenko et al. "Pullback transformation in gyrokinetic electromagnetic simulations", *Physics of Plasmas* 21, 9 (2014), p. 092110.

[139] F. Vannini. "Gyrokinetic investigation of the nonlinear dynamics of Alfvénic instabilities and comparison with observations in ASDEX Upgrade." PhD thesis. Universität Ulm, 2023.

[140] M. Weiland et al. "RABBIT: Real-time simulation of the NBI fast-ion distribution", *Nuclear Fusion* 58, 8 (2018), p. 082032.

[141] M. Weiland et al. "Simulation of neutron emission in neutral beam injection heated plasmas with the real-time code RABBIT", *Nuclear Fusion* 59, 8 (2019), p. 086002.

[142] R. J. Goldston et al. "New techniques for calculating heat and particle source rates due to neutral beam injection in axisymmetric tokamaks", *Journal of computational physics* 43, 1 (1981), pp. 61–78.

[143] A. Pankin et al. "The tokamak Monte Carlo fast ion module NUBEAM in the National Transport Code Collaboration library", *Computer Physics Communications* 159, 3 (2004), pp. 157–184.

[144] E. Hirvijoki et al. "ASCOT: Solving the kinetic equation of minority particle species in tokamak plasmas", *Computer Physics Communications* 185, 4 (2014), pp. 1310–1321.

[145] I. Novikau et al. "Nonlinear dynamics of energetic-particle driven geodesic acoustic modes in ASDEX Upgrade", *Physics of Plasmas* 27, 4 (2020), p. 042512.

[146] A. Bottino et al. "Monte Carlo particle-in-cell methods for the simulation of the Vlasov-Maxwell gyrokinetic equations", *Journal of Plasma Physics* 81, 5 (2015), p. 435810501.

[147] A. Popa et al. "EP-Stability-WF: an IMAS-integrated workflow for energetic particle stability", *Nuclear Fusion* submitted, (2023).

[148] A. Bottino et al. "Time evolution and finite element representation of Phase Space Zonal Structures in ORB5," *Journal of Physics: Conference Series.* Vol. 2397. 1. IOP Publishing. 2022, p. 012019.

Acknowledgments

This work cannot be declared complete without thanking the people who made it possible, and supported my PhD research, as well as my scientific and personal growth over these years. Firstly, I thank sincerely Prof. Dr. Frank Jenko for giving me the opportunity to spend these years at the Max Planck Institute for plasma physics. IPP lived up to any of my expectations, being an intellectually fertile environment, enriched by the people who animate it. I thank Frank and the IPP for all the opportunities to learn from the world experts of my research field, not only inside the IPP, but also at important international conferences.

I thank heartily my scientific supervisor, Dr. Alberto Bottino, and Dr. Thomas Hayward-Schneider, they have closely supervised my work, responding always effectively and quickly to any of my uncountable questions and doubts. They patiently and daily led me through this long path. Their constant guidance has shaped my work and left a deep mark on all I have learned and accomplished in these years.

I thank profoundly Dr. Philipp Lauber for having been a point of reference, and for shedding light on difficult subjects to understand the nature of the physics we research on. A warm thank goes to Dr. Alessandro Biancalani for his expertise on theory and his patience to explain me the most complex derivations. I would like to thank Dr. Francesco Vannini with whom I shared the daily doubts and the office for most of my time here.

I was very inspired by all these people, by their thorough knowledge of both physics and computation. I thank them for their help, which enabled me to accomplish my goals, for the many friendly discussions and for their kind willingness to share their knowledge with me.

Furthermore, I am glad to have had the opportunity to work in the IPP environment. I met a lot of very competent people, some of whom I had the pleasure to become friend of. I would like to thank Emanuele Poli, Xin Wang, Zhixin Lu, Markus Weiland, Hartmut Zohm, Valentin Igochine, Alessandro di Siena, Michael Dunne for the interesting exchange on various topics.

I would like to thank all the friends that I met in this amazing environment with which I could share both professional and personal experiences. I had the privilege to have become friend of Oleg Samoylov, with whom I shared the cold long walks to Mensa in the dark pandemic winters, with whom I shared my deepest thoughts and ideas. I